POLITECNICO DI MILANO

Scuola di Ingegneria Industriale

Corso di Laurea Magistrale

in Ingegneria Energetica

Study of an advanced solar tower plant using sodium as heat transfer fluid and sCO$_2$ power cycle: technological limits and components design

Relatore:

    Prof. Marco BINOTTI

Co-relatore:

    Ing: Edoardo PADOVANI

Tesi di Laurea Magistrale di:

Anna MARABELLI   Matr. 899390

Anno accademico 2018/2019

Ringraziamenti

La scelta del mio percorso di studi è stata molto influenzata dal mio essere una persona pratica e a cui piace "vedere le cose che studia", per questa ragione ho iniziato ingegneria piuttosto che fisica o matematica. Sempre per questa mia propensione, ho preferito, nell'affrontare la tesi, provare un'esperienza sul campo, che mi facesse capire cosa vuol dire lavorare veramente, per questa opportunità non posso che ringraziare Michele Ferrazzini, non solo per avermi dato la possibilità di svolgere la tesi in ESE, ma anche per avermi aiutato, fin dai tempi del liceo, nelle scelte riguardanti i miei studi.

Lavorando alla tesi in ESE ho trovato un ambiente allo stesso tempo professionale e familiare, per questo vorrei ringraziare tutti i miei colleghi che hanno fatto in modo che, come una volta disse Angela, non ci sia nessun motivo per non voler venire a lavorare. Vorrei ringraziare in particolare Edoardo e Davide per avermi aiutato e indirizzato in questa tesi e Franco che, mostrando grande interesse per l'argomento scelto, mi ha dato ascolto e utilissimi consigli.

Questo lavoro di tesi non sarebbe stato possibile se oltre al contributo di ESE non avessi potuto contare sulla collaborazione di aziende come AC Boilers, Alpha Laval e Franco Tosi Meccanica, in particolare vorrei ringraziare Emanuel Pesatori, non solo perché il suo contributo è ciò che più rende valido questo lavoro, ma anche per aver sopportato le mie chiamate insistenti e la mia testa dura.

Ringrazio moltissimo anche il professor Binotti le cui lezioni mi hanno introdotto al fantastico mondo del CSP e i cui consigli durante lo svolgimento della tesi sono stati illuminanti specialmente in momenti in cui ero smarrita e non sapevo come continuare il lavoro.

Per avermi permesso di studiare, per avermi sopportato e supportato nei periodi preesame non posso non ringraziare la mia famiglia; ringrazio mia mamma che mi ha curato amorevolmente tutte le volte che avevo qualche malattia psicosomatica dovuta allo stress, mio papà perché grazie alle chiacchierate con lui riguardo a carrucole e cuscinetti sono anche riuscita a prendere qualche trenta, ringrazio mia sorella che mi è stata di esempio nello studio e che si è sempre preoccupata di chiedermi come era andato l'esame di turno.

Ringrazio i nonni Tiziana e Giuseppe che, devoti, sono andati a messa prima di ogni esame e che patiscono pazientemente i dispetti che tuttora gli faccio per amore, alla nonna Mara e il nonno Puccio che mi hanno sopportato in giovinezza quando il mio carattere non era ancora domato e che ora, chi dal cielo e chi da casa, mi vogliono bene con dolcezza.

Allo zio Paolo Z., sempre attento al mio percorso di studi, agli zii Paolo e Marina la cui casa è sempre stata come se fosse la mia, ai cugini: Ale Elena e Letizia, compagni di giochi, scout, scuola e confidenze, insomma tutto, da sempre.

Agli scout, alle serate accanto al fuoco e ai campi sotto la pioggia perché senza di loro non sarei la persona che sono ora e perché so che sono gli amici che rimarranno. Un grazie speciale va a Elena, Giuspri, Alice, Marianna, Lucia e Sara, grazie perché siete le persone con cui posso confidarmi su tutto, perché ogni tanto mi fate da mamma e ogni tanto sono io un po' mamma per voi e grazie perché alcuni dei momenti passati con voi me li ricordo come i più felici della mia vita.

Grazie alla famiglia di Nicolò, che in queste settimane di quarantena mi ha accolto come se ne fossi parte integrante.

Infine grazie a Nicolò che ho scoperto essere il compagno di avventure ideale e che mi fa sentire amata.

Table of contents

Abstract

One of the most important global challenges in this period of time, is the reduction of GHG emissions, CSP is of particular interest since it can provide dispatchable renewable energy thanks to the integration of a thermal storage, mitigating grid control issues which arised from the penetration of intermittent sources such as Solar PV and wind. CSP LCOE is still very high making it still not competitive with other renewable sources such as PV or wind, therefore new ways to increase plant efficiency and reduce investment cost are being studied.

This study considers two technological innovations aimed at increasing solar to electric efficiency increasing maximum temperature: the adoption of liquid sodium as HTF which allows a higher maximum HTF temperature compared to conventional solar salts and higher heat fluxes due to its outstanding heat transfer characteristics and the employment of an sCO_2 in the power block, which has smaller turbomachinery compared to the equivalent steam components and that, at this temperatures, is expected to have higher efficiency.

The purpose of this study is to verify the manufacturing feasibility of the components in an industrial context, assuming operating conditions previously studied in other works, and to give an indication on potential problems which must be addressed when designing this kind of plant. This analysis has been performed through a research in specific components literature and contacts with manufacturing companies such as Franco Tosi Meccanica, AC Boilers (formerly Ansaldo Caldaie) e Alpha Laval. Initially a preliminary design of the plant was performed and various parameters of the plant subsystems were optimized. Some results from these optimizations are that the receiver aspect ratio must be close to 1 in order to optimize solar to thermal efficiency and that overall solar to electric efficiency has a monotonically increasing trend as turbine inlet temperature is increased from 723.6°C to 785°C.

From the turbine feasibility study it emerged that the maximum turbine inlet temperature must be 725°C to avoid blade and rotor cooling, moreover a mechanical analysis was performed in order to assess maximum tube temperature on the receiver, which resulted in a temperature limit of 871°C. Finally, an optimized design of the plant, compliant with found limitations, was realized in order to evaluate design and annual performances of the plant. The resulting annual solar to electric efficiency is 20.21%, lower than the 22.79% solar to electric efficiency in design conditions since it is negatively affected from the off-design operation of the solar field and receiver.

Sommario

Una tra le più importanti sfide globali di questo periodo storico è la riduzione delle emissioni di gas serra. La tecnologia CSP è particolarmente interessante da questo punto di vista poiché l'energia prodotta non solo è tratta da fonte rinnovabile ma inoltre è programmabile, infatti l'energia termica derivante dal sole può essere stoccata sotto forma di calore e poi utilizzata per produrre energia elettrica a seconda della richiesta elettrica. Grazie a questa caratteristica l'energia elettrica prodotta da impianti CSP può essere controllata e utilizzata per mitigare i picchi di elettricità sulla rete dovuti alle fonti non programmabili e non prevedibili. Nonostante i suoi vantaggi, il LCOE di questa tecnologia è ancora molto alto rispetto a quello di altre tecnologie rinnovabili come il fotovoltaico o l'eolico, rendendo la tecnologia CSP poco competitiva. Per questo motivo, molti recenti studi focalizzano la loro attenzione su nuove metodologie per aumentare l'efficienza totale del sistema e per diminuirne il costo d'investimento.

Questo studio prende in considerazione due innovazioni tecnologiche che hanno lo scopo di aumentare l'efficienza totale dell'impianto tramite l'aumento della temperatura massima del sistema. Innanzitutto, l'utilizzo di sodio fuso come fluido termovettore nel ricevitore solare consente di aumentare la temperatura massima del fluido nel ricevitore solare, inoltre, grazie alle sue eccellenti caratteristiche di scambio termico, permette anche di realizzare ricevitori più piccoli a parità di potenza, aumentando il flusso di calore sulla superficie. Inoltre, l'impiego di cicli a CO_2 supercritica nel blocco di potenza implica l'utilizzo di turbomacchine di dimensioni ridotte rispetto alle corrispettive a vapore e una più alta efficienza di ciclo attesa alle temperature considerate.

Lo scopo di questo studio è quello di verificare la fattibilità tecnica della produzione di componenti che devono operare alle condizioni estreme ipotizzate in studi precedenti. L'autore, inoltre, vuole dare indicazioni di quali potrebbero essere i problemi che sorgono durante il design di un impianto di questo genere. Le informazioni sono state reperite tramite ricerche bibliografiche focalizzate sugli specifici componenti e la collaborazione con alcune aziende manifatturiere quali: Franco Tosi Meccanica, AC Boilers (prima Ansaldo Caldaie) e Alpha Laval.

Inizialmente un design preliminare è stato elaborato, tramite la ricostruzione di modelli dei sottosistemi dell'impianto solare, successivamente alcuni parametri di ricevitore solare, campo specchi e blocco di potenza sono stati ottimizzati per massimizzare l'efficienza totale dell'impianto. Alcuni risultati delle suddette ottimizzazioni sono: l'aspect ratio del ricevitore, che ne determina le proporzioni, deve essere vicino a uno per ottimizzare il prodotto tra efficienza ottica e termica, inoltre l'efficienza totale dell'impianto (da energia solare a elettrica) cresce all'aumentare della temperatura di ingresso in turbina nel range [723.6;785]°C.

Dallo studio di fattibilità eseguito per la turbina è emerso che la temperatura di ingresso in turbina non deve superare i 725°C se si vuole evitare il raffreddamento delle pale e del rotore. Inoltre, un'analisi meccanica è stata eseguita sui tubi di ricevitore per determinare la massima temperatura sostenibile dal materiale, la quale è risultata essere 871°C.

Infine, un design definitivo ottimizzato, tenente conto dei limiti tecnici sopra citati, è stato elaborato allo scopo di valutare le performance di design e annuali dell'impianto. L'efficienza annuale totale dell'impianto calcolata è 20.21%, minore dell'efficienza totale in condizioni di design poiché risente degli effetti di off-design sul campo solare e sul ricevitore.

Extended Abstract

Introduction

The problem of global warming is driving the energy industry towards renewable and low carbon intensity sources. Among these, solar photovoltaic and wind power installed capacity increased majorly in the last decade [1]. The increase of power production from unpredictable and intermittent renewable sources, such as wind and PV, has increased majorly in the last decade and has brought new grid control challenges and an increased need of new methods of energy storage.

CSP can be a very interesting technology due to its ability to produce dispatchable renewable power thanks to the low-cost integration of a thermal energy storage systems. The Solar Power Tower technology (SPT) is more promising than Parabolic Through Collectors (PTC) due to its higher concentration ratio and the ability to work with higher maximum temperature heat transfer fluids, such as molten salt or liquid metals, which have a solidification temperature higher than ambient temperature.

Even if CSP cost has decreased in the latest years [2] its LCOE is still too high to make this technology competitive with other renewable technologies such as PV and wind, therefore efficiency improvement and cost reduction are necessary.

Increasing cycle maximum temperature affects positively PB efficiency, although temperature is limited by the choice of the HTF. Conventional molten salts, employed in currently developing SPT projects, cannot exceed 565°C due to thermal degradation phenomena. A few candidates can reach 700°C, some advanced molten salts, such as KCl-MgCl$_2$, and liquid metals, such as sodium and lead-bismuth eutectic (LBE) [3][4]. Sodium was chosen for outstanding heat transfer characteristics of liquid metals with respect to molten salts and for the maturity level of the technology with respect to other liquid metals such as LBE, indeed liquid sodium has been studied, tested and commercialized as a primary and secondary HTF for fast breed nuclear reactors [5].

Another innovation which was considered for CSP plants is the adoption of an sCO$_2$ cycle instead of conventional steam cycles [6]–[8]. The superiority in CSP applications of sCO$_2$ cycles over steam cycles at temperatures above 600°C has been studied in literature ([4], [6], [9]–[11]). In general A-USC steam cycles, whose operation above 700°C is currently being studied in order to maximize efficiency of fossil fuels power plants, cannot be coupled with CSP because the small sizes, typical of this technology, do not justify the very high investment cost [4]. Supercritical CO$_2$ can reach higher temperatures and potentially higher efficiency, moreover they have much smaller turbomachinery, due to CO$_2$ high density. Lastly, they do not suffer as much as steam cycles of the scale-down effect. The sCO$_2$ RMCI cycle configuration was chosen according to Polimeni et al. [4] since it has the highest efficiency.

The purpose of this thesis is to verify that the assumptions made in previous studies are realizable in an industrial context, and to give an indication on potential problems which must be addressed when designing this kind of plant, through research in specific components literature and contacts with manufacturing companies. Finally, it aims to realize an optimized design which accounts for real limits of the materials and efficiency of the components assessing the plant performances during design conditions and through an annual simulation.

Models and Methodology

For this work models of the power block, receiver and solar field where built in order to optimize a few parameters and to assess the plant performances. Models interact with each other in order to optimize in each parametric analysis all the subsystems of the plant. The PB power output is fixed at 30 MW, thermal power entering the cycle is then determined by the PB efficiency and it is an input of the receiver model, same as for sodium temperatures which depend from sCO$_2$ temperatures on the PHX. Receiver and solar field models are reciprocally

dependent since the flux map on the receiver, which is determined by the solar field layout and aiming strategy, depends from the receiver dimensions and power, while dimensions depend from the flux map. In this analysis, indeed, receiver dimensions are not kept constant, but they are changed in order to maintain maximum tube temperature on the receiver constant. Each optimal design is therefore found through an iterative procedure described by the flow diagram in Figure 0.1.
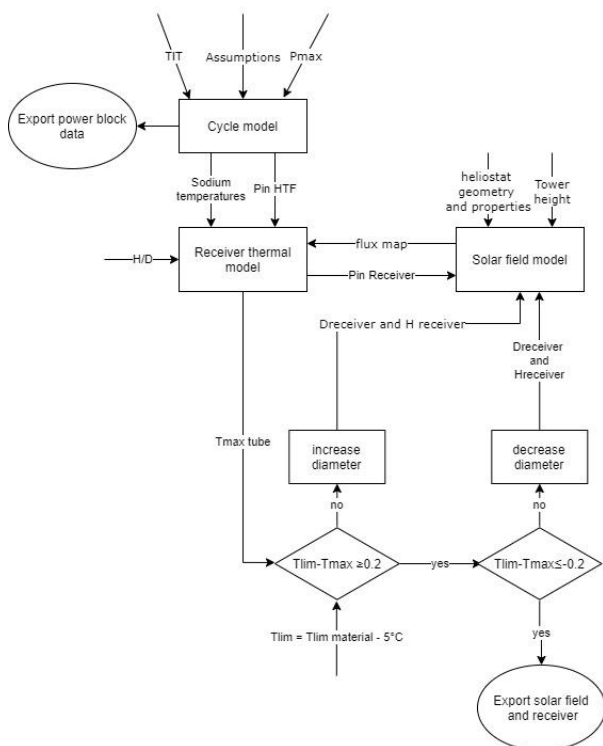

Figure 0.1 Flow diagrams of the different models interactions

Power block

A simplified power block model was developed on Excel using the Refprop add in for the calculation of CO_2 properties, the assumptions made for the development of this model are reported in Table 0.1.

Assumptions	
Turbine inlet pressure [bar]	250
CO_2 minimum temperature [°C]	52
ΔT_{min} LT/HT regenerator [°C]	12
Turbine isentropic efficiency	0.93
Compressor isentropic efficiency	0.85

Mechanical/Electrical efficiency	0.99/0.99
$\Delta p/p$ HP side of LTR (Cold side)	0.0006*
$\Delta p/p$ LP side of LTR and HTR (Hot side)	0.015
$\Delta p/p$ HP side of HTR (Cold side)	0.0016*
$\Delta p/p$ PHX (CO_2 side)	0.015
$\Delta p/p$ precooler	0.02

Table 0.1 Assumptions for the design of the PB (values calculated with a secondary pressure drop model)* [4]

The chosen configuration is a recompressed main compressor intercooling cycle (RMCI). Recompression is the splitting of the low pressure mass flow rate at the cold end side of the LTR, a part is directly compressed to the HTR inlet conditions, while the other is cooled to 52°C, then compressed in the main compressor, which is inter-refrigerated, and finally heated in the LTR. Recompression is performed to decrease heat transfer losses in the LTR, decreasing heat capacity on the HP side, which would be, otherwise, much higher than the LP side one. From previous analyses [12] the optimal split ratio (SR) resulted to be the one ensuring no entropy loss due to mixing at the HTR inlet.

Figure 0.2 RMCI cycle T-s diagram
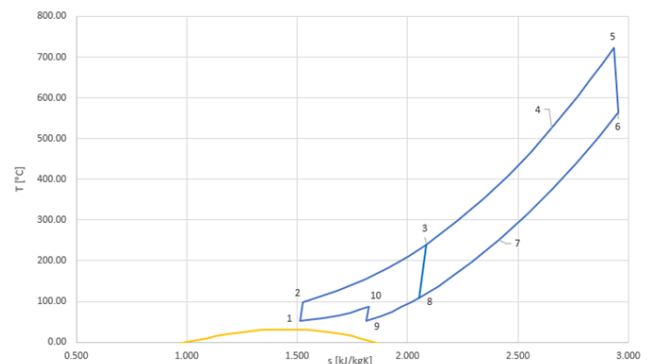
The power block design is adjusted in every analysis optimizing the turbine expansion ratio and the intermediate pressure.

Receiver

Receiver thermal and pressure losses model was designed on Excel in order to optimize its geometrical parameters and calculate its performances.

The thermal model takes in input geometry of the receiver, ambient conditions and the flux map, it

12

discretizes each panel in several vertical section calculating for each section the energy balance through the modelling of a thermal network (Figure 0.3).
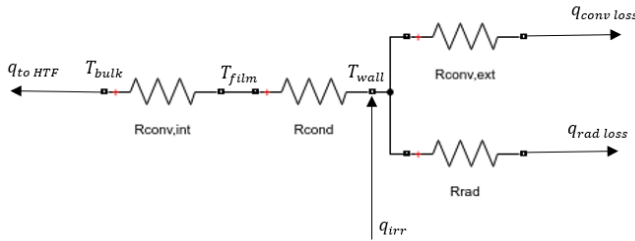

Figure 0.3 Receiver tube section thermal network

Radiative and convective losses are calculated through an iterative procedure considering the Sleicher, C.A. & Rouse, M.W. correlation, specific for sodium, suggested by Boerema et al. [3] and Benoit et al. [13] for the internal heat transfer coefficient calculation.

Conduction across the tube walls was modelled calculating the equivalent conductive resistance of the non-uniformly irradiated tube. Since irradiation is not uniform the equivalent resistance can be conceived as the sum of two equal resistances in parallel (called R1 in Figure 0.4). The resistance R1, which is used in the overall thermal network, is then calculated from the well known hollow cylinder conductive resistance.
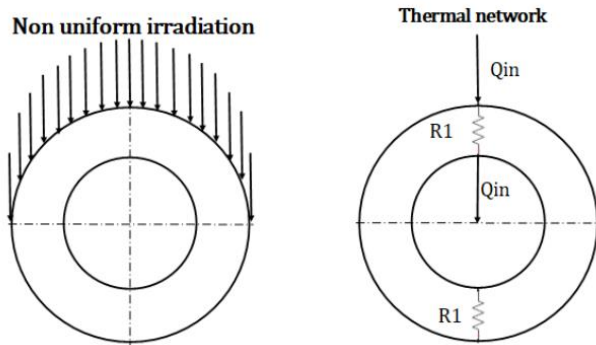

Figure 0.4 Conductive thermal resistance scheme

Eq. 0.1, recommended by Sieber and Kraabel [14], was used to account for both forced and natural convection.

$$h_{mix} = (h_{fc}^a + h_{nc}^a)^{1/a}$$ *Eq. 0.1*

An average forced convection heat transfer coefficient was calculated accounting the cylinder rugosity due to receiver tubes as in Achenbach [15], while the natural convection coefficient was calculated for each section since it depends from surface temperature.

The radiative heat losses were calculated considering the optical properties of the paint coating Pyromark° 2500 [16], accounting for the absorptivity degradation which occurs in a few hours if the paint is exposed at the temperature considered in this work.

The pressure loss model takes in input the pipe list, comprising outer diameter, thickness, length and number of curves and valves of each pipe and, assuming rugosity equal to 45μm, calculates distributed and concentrated pressure losses in each pipe. The calculation of the friction factor λ was performed using the Colebrook equation [3].

Solar field

The solar field layout was designed though the software SolarPILOT [17]. The model takes in input receiver dimensions and power and it gives as output the optimized solar field layout and receiver flux map. Some parameters, such as tower height, heliostat dimensions and their properties, were initially assumed and are kept constant in every analysis.

Preliminary design analyses

In the preliminary design a few technical limits were accounted for. In particular a maximum wall temperature was chosen on the basis of creep and low cycle fatigue phenomenon once the tubes material (Haynes 230® [18]) was determined, maximum flow velocity in tubes, which was set to 6 m/s to avoid erosion [5] and the maximum film temperature, which is the evaporation temperature of sodium (882°C [19]).

Geometry of the receiver was optimized evaluating the variation of tubes diameter, number of passes and panels per pass, receiver diameter and hight; these last two variables are related from the aspect ratio, which was analysed separately. From the analysis emerged that a tube diameter of 33.4 mm coupled with the distribution of the flow on three passes in series give good results in terms of heat transfer without increasing the fluid velocity over the critical value of 6 m/s.

From the parametric analysis on the aspect ratio, defined as H/D, emerged that aspect ratios closer to 1 result in higher optical efficiency and higher peak fluxes, in order to maintain maximum tube temperature fixed the receiver area must be increased, which result in slightly lower receiver thermal efficiency.

Although decreasing receiver diameter in favour of a larger receiver height, the number of tubes which fit in parallel in each panel decreases, rising fluid velocity inside the tube. For aspect ratios higher than about 1.3 it was necessary to increase the tubes diameter in order to have a higher flow area and lower flux velocity. This tube dimension variation resulted in an abrupt decrease of thermal efficiency. Finally, an aspect ratio of 1 was chosen due to its higher overall efficiency (Figure 0.5).
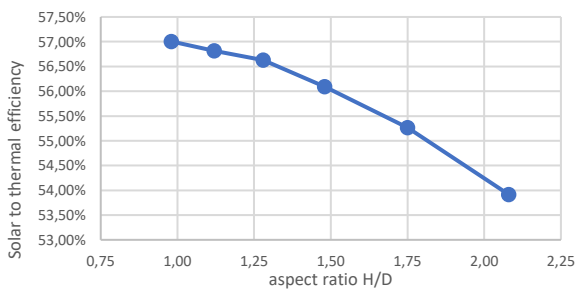

Figure 0.5 Solar to thermal efficiency varying aspect ratio, the analysis has been conducted maintaining maximum tube temperature equal to 865°C and varying the receiver surface area accordingly

When designing the solar field SolarPILOT automatically optimizes the heliostats number and positions, a further optimization was performed on the positioning cut off factor, which determines the aiming strategy of heliostats to the receiver. This parameter influences the shape of the flux map and the optical efficiency, particularly the image intercept efficiency. From this analysis emerged that increasing the positioning cut off factor enhances the optical efficiency, but it increases peak flux (see Figure 0.6) consequently influencing negatively thermal efficiency.

From the results it emerged that efficiency is highest when the cut off factor is 2.5, although, between a value of 2 and a value of 2.5 the efficiency increases of less than 0.3% while the area must be increased by 1/5 of the total surface to respect the maximum tube temperature limit. For this reason, the cut off factor was set to 2.
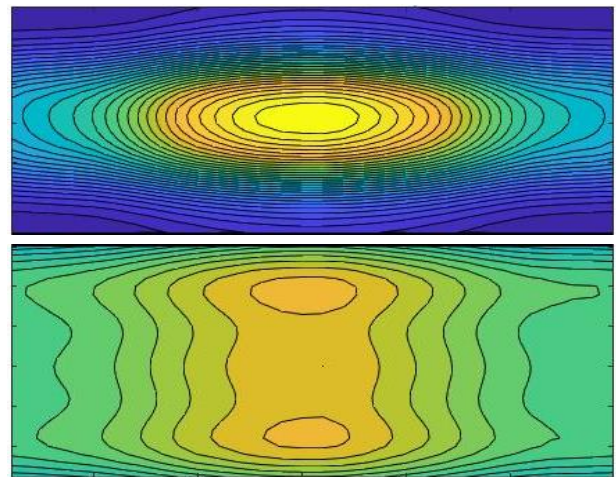
Figure 0.6 Flux maps resulting from a cut off value of 3 (on top) and of 0.5 (on the bottom) maintaining an aspect ratio of 1 and constant maximum tube temperature (thus varying receiver dimensions), the second flux map is clearly less peaked and has a more even distribution.

Lastly the analysis on maximum turbine inlet temperature highlighted that increasing temperature in the range investigated (723°C-785°C) is always beneficial for the overall plant efficiency (Figure 0.7), this result also depends from the choice to maintain fixed the maximum tube temperature increasing receiver area. Increasing TIT requires to increase receiver area, which results in a decrease of receiver thermal efficiency and in an increase of optical efficiency since there are less heliostats (due to the higher efficiency and fixed power output), which aim at a larger target.
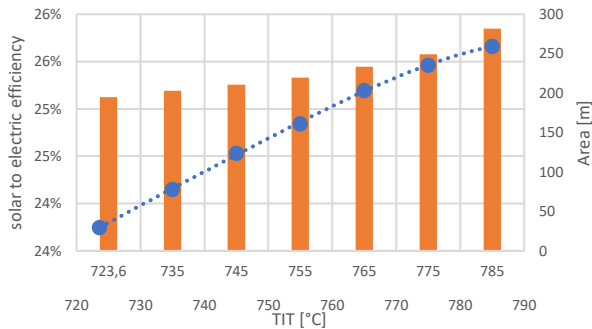
Figure 0.7 Solar to electric efficiency and receiver surface varying TIT

Ultimate design

This thesis work aimed at investigating real technical limits of the plant designed considering input provided by manufacturing companies (Franco Tosi Meccanica, AC Boilers and Alpha Laval). Where it wasn't possible to have direct contacts with the manufacturing companies, literature research favoured industrial articles.

1. Technical limits

During the investigation of technical limits, it emerged that the aspect which requires more technical advance is the very elevated temperature.

In particular, at such high temperatures the mechanical design of the receiver is very challenging since this component is exposed to high uneven irradiation. In this work a mechanical analysis was performed, accounting for the effect of pressure and thermal gradients. Creep and low cycle fatigue are the two most important degradation phenomena, creep and LCF data used for the comparison come from Haynes 230 datasheet.

The maximum stress experienced from the receiver tubes, calculated with the Mariotte equation (Eq. 4.2), is compared to the Yeald stress of Haynes 230 at 871°C, the maximum creep stress and the maximum allowable stress given by ASME norms.

The thermal stresses due to non-uniform temperature distribution along the tube surface can be estimated with the Eq. 0.2 from Babcock and Wilcox [20]. This stress must be below 2 times the yield stress and the thermal strains resulting must be below a certain limit in order to avoid the low cycle fatigue phenomenon.

$$\varepsilon = a \left[\frac{T_{max\,wall} + T_{film}}{2} - \left(T_{bulk} + \frac{\left[\frac{T_{max\,wall} + T_{film}}{2} - T_{bulk} \right]}{\pi} \right) + \left(\frac{T_{max\,wall} - T_{film}}{2(1 - \nu)} \right) \right]$$

Eq. 0.2

where a is the coefficient of thermal expansion and ν is the Poisson's ratio.

Moreover, the cumulated damage was verified using the method of the linear superposition of fatigue and creep damage, since the two damage mechanisms interact reducing furtherly the life of the component.

The mechanical analysis results are reported in Table 0.2, in bold maximum mechanical stresses and strains experienced by the receiver tube which must be lower than material stresses and strain limits (on the left). Results showed that a temperature limit of 871 °C can be sustained by the tubes material coupled with a tube diameter of 33.4 mm and 1.65 mm.

Maximum membrane stress due to pressure experienced by the receiver tubes (Mariotte eq.)	Yield stress of Haynes 230® at 871°C divided by 1.5 (Babcock and Wilcox company [21])	Maximum allowable creep stress taken from Haynes 230 datasheet at 871°C for a time of 91250 h	Maximum allowable creep stress for Haynes 230 at 875°C given in ASME section II, part D
9.58 MPa	157.33 MPa	19.19 MPa	13.8 MPa
Maximum thermal stress due to uneven irradiation on the tube surface (Babcock and Wilcox company [21])	Yield stress of Haynes 230 at 871°C multiplied by 2 (Babcock and Wilcox company [21])		
448.57 MPa	472 MPa		
Maximum thermal strain due to uneven irradiation on the tube surface (Babcock and Wilcox company [21])	Maximum allowable strain to have creep initiation due to low cycle fatigue at 871°C after 18250 cycles		
0.282%	0.357%		
Cumulated damage			
$\frac{18250}{131072} + \frac{91250}{1015884} = 0.229$			1

Table 0.2 Results of the mechanical analyses performed

Other critical components are the HXs. Initially, Printed Circuit Heat Exchangers (PCHE) design was considered for every heat exchanger (HX) of the system. Information on the limitations of these type of HX comes mostly from a discussion with Alpha Laval, company which manufactures shell and tube and PCHE, and from the article [22], written by Heatric engineers on the mechanical design of PCHE, Heatric is one of the most important manufacturers of diffusion bonded heat exchangers. PCHE design is limited in temperature and pressure, high pressure PCHE cannot sustain temperatures above 650°C. Moreover they are not suitable for sodium applications, Heatric suggests a hybrid design (H2X) which is, instead, compatible with sodium as HTF. Indeed, PCHE layout with its very small channels could have plugging issues with sodium which solidifies below 98°C. For these reasons, at this temperature and pressure the only viable option for the PHX is a shell and tube, whose feasibility has been verified with Alpha Laval. PCHE are, instead, feasible and particularly interesting for the regenerators, indeed this layout allows a more efficient gas-to-gas heat exchange with a smaller HX volume, thus reducing its cost.

A feasibility study of the turbine was performed in collaboration with Franco Tosi Meccanica. Initially a research on material which can be suitable for turbine parts manufacturing was developed, resulting in the choice of alloy N07263 for the rotor manufacturing. From a previous study made by FTM [23] emerged that blade cooling can be avoided, reducing notably turbine complexity and cost, if TIT is kept below 750°C. Rotor maximum temperature sustainable was, instead, calculated with the Larson miller extrapolation using the criteria of 100'000 h strength at 100 MPa, it resulted to be 725°C.

To keep TIT equal to 750°C rotor must be cooled through a refrigerating flux. The refrigeration flux intake point must be chosen wisely in other to avoid high thermal gradients and ensure a sufficient pressure, in this work it was decided to take it at the PHX inlet. Refrigeration is performed injecting the cooling fluid in a specifically realized cavity between a liner below the first stator and the rotor body (in Figure 0.8). The cooling process is effective only if

convection is high, therefore a study of the Nusselt number changing cooling mass flow rate was performed, geometric parameters used come from the FTM proprietary code "Fila per Fila". This analysis showed good convective heat transfer is possible on rotor surface.
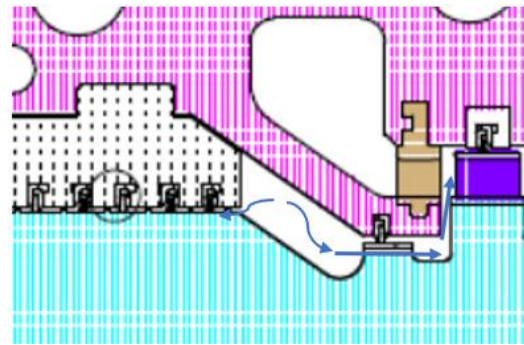
Figure 0.8 Cooling flow scheme of the turbine rotor (property of FTM)

Turbine rotor cooling leads to an efficiency loss which increases with higher refrigerant mass flow rates. This analysis showed that if the mass flow rate of cooling fluid needed to refrigerate the rotor is higher than 2.66% it is less detrimental for the cycle efficiency to decrease TIT to 725°C, temperature sustainable by the rotor without cooling.
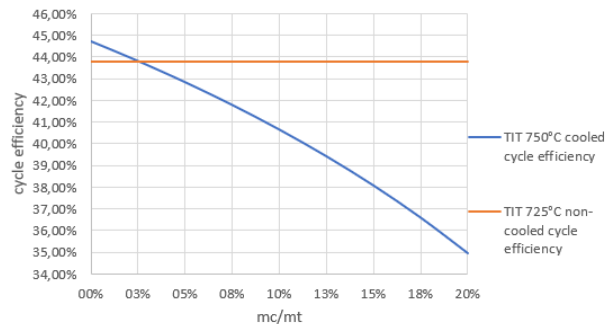
Figure 0.9 Comparison between efficiency loss of a 750°C turbine due to refrigeration (dependent on cooling mass flow rate) and efficiency decrease due to lower TIT (725°C)

Lastly two possible turbine designs were realized in collaboration with FTM. The first one is the maximum efficiency design, with a blading efficiency of 93.19%, in this design all stages are 0.5 degree of reaction. The second design, instead, was conceived in order to decrease as much as possible the number of stages and the temperature at the outlet of the first stages of the turbine, this temperature

reduction should reduce the need of high temperature resistance materials earlier in the stages. This effects are possible if the reaction degree in the first stages is reduced below 0.5, obtaining more loaded stages, although this design penalizes efficiency indeed this turbine can only achieve 92.26% of blading efficiency.

Together with FTM, a few considerations on the compressors were discussed. Compressors for this plant size are all radial, in this work they have been assumed directly coupled to the turbine through a gear box. A simple compressor sizing has been performed through the Balje diagram in order to keep efficiency at its maximum value of 85% and to avoid unstable operation enar the critical point.

Among limitations a research on sodium plant attentions was performed. In particular it emerged that sodium pumps can be critical components, some issues and possible resolutions found in literature are reported.

Lastly sCO2 corrosivity at very high temperatures has been considered, this topic needs further research, especially in the range of temperature and pressure of interest, although from considered studies nickel alloys seem to be the most resistant alloys when subject to sCO2 oxidation.

2. Design choices

The ultimate design takes account of the previously cited limitations and efficiency assumptions. In this design the turbine inlet temperature has been lowered, moreover pressure losses in the pipeline from the PHX to the turbine, as well as the pressure losses on the turbine inlet control valve where accounted. Turbine isentropic efficiency was adjusted with the values resulting from FTM calculations. Then cycle β and RPR were optimized, same as for the receiver geometry and solar field layout consequently. Receiver dimensions were calculated in order to maintain maximum tube temperature 865°C. The results reported in Table 0.3 consider ambient design conditions: 950 W/m^2, solar noon of the 21 of June, with an ambient temperature of 35 °C, wind at 5 m/s.

PB efficiency	45.63%
Receiver thermal efficiency	87.02%
SF optical efficiency	64.71%
SF aux consumption	3.51 MW
Net solar to electric efficiency	22.79 %

Table 0.3 Plant performances in design conditions

Annual simulation

The annual simulation required the evaluation of off design conditions of all the subsystems of the plant.

The optical efficiency variation though the year and day was evaluated with SolarPILOT changing solar azimuth and zenith (Figure 0.10).
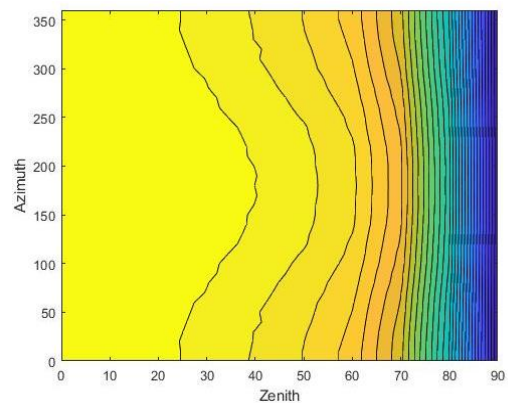
Figure 0.10 Optical efficiency varying sun position in the sky.

The receiver thermal efficiency depends on wind velocity, ambient temperature and incident irradiation, lower incident irradiation results in a decrease in surface temperature and a consequent reduction of thermal losses, although this reduction is less than proportional to the decrease of irradiation, therefore thermal efficiency decreases with partial load operation. From parametric analyses emerged that incident power is the variable with a larger impact and that increasing wind in the range of interest (wind speed range in the chosen location) is more detrimental than decreasing ambient temperature. For this reason and because a three parameter interpolation, necessary to account for the three variables, would have been too time consuming, only wind and incident power effects were considered to create a thermal efficiency matrix.
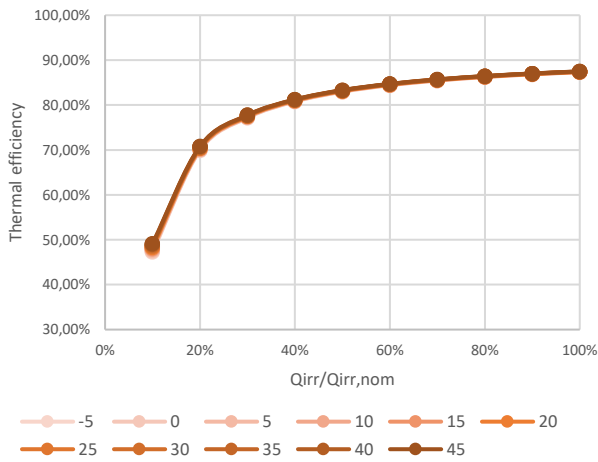
Figure 0.11 Effect of ambient temperature and irradiation on receiver thermal efficiency
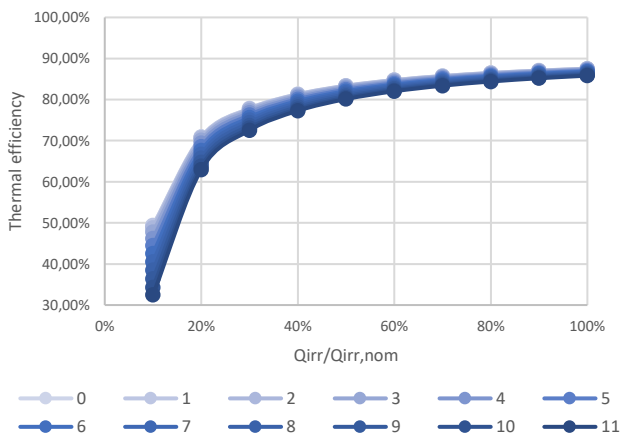
Figure 0.12 13 Effect of wind speed and irradiation on receiver thermal efficiency

Power block is always operated in design conditions for a few reasons, firstly, as it emerged from turbomachinery analysis, changing working conditions could be very detrimental for turbomachinery efficiency and thus for PB efficiency, moreover, in the energy scenario in which CSP operates now, SPT plants are more likely to be used as base load in the energy share and, therefore, to work and constant load until the storage tank is empty. Even if it is important to realize that in future scenarios, CSP with large storage tanks could be useful to cover intermittent renewable negative peaks, therefore an efficient off design should be studied in future works.

In this thesis, only the effect of ambient temperature was considered increasing or decreasing HRUs power, since power exchanged must be constant, the exchange area of the HRU is constant and the global heat transfer coefficient (U) was approximated constant the ΔTml must be unchanged. Ambient temperature range [5°C;45°C] was discretized and the HRUs area was designed to be able to reject nominal power even in the worst temperature conditions. Lastly, for each case the outlet air temperature was calculated in order to keep ΔTml constant and consequently air mass flow rate can be evaluated; HRUs power was assumed directly dependent from air mass flow rate.

The last off design considered is the HTF pump operating in the receiver loop which changes when receiver is operated at partial load, varying HTF mass flow rate, while power consumed by the PHX loop pump is two orders of magnitude lower [8], therefore it was neglected.

For the annual simulation a thermal storage filling strategy was developed (flowchart in Figure 0.14), according to it the program chooses when to fill and when to empty the hot storage tank, determining energy delivered to the PB and energy defocused when the hot tank is full. The tank size should be optimized in an economic analysis, in this work a storage size of 17 heq was chosen since it is the maximum size found in literature.
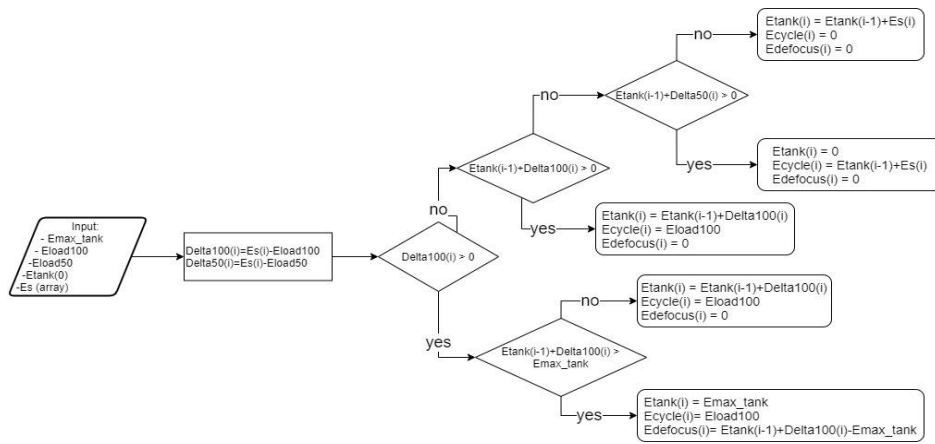
18

Input:
- Emax_tank
- Eload100
- Eload50
- Etank(0)
- Es (array)

Delta100(i)=Es(i)-Eload100
Delta50(i)=Es(i)-Eload50

Delta100(i) > 0

no →

Etank(i-1)+Delta100(i) > 0

no →

Etank(i-1)+Delta50(i) > 0

no →

Etank(i) = Etank(i-1)+Es(i)
Ecycle(i) = 0
Edefocus(i) = 0

yes →

Etank(i) = 0
Ecycle(i) = Etank(i-1)+Es(i)
Edefocus(i) = 0

yes →

Etank(i) = Etank(i-1)+Delta100(i)
Ecycle(i) = Eload100
Edefocus(i) = 0

yes →

Etank(i-1)+Delta100(i) > Emax_tank

no →

Etank(i) = Etank(i-1)+Delta100(i)
Ecycle(i) = Eload100
Edefocus(i) = 0

yes →

Etank(i) = Emax_tank
Ecycle(i)= Eload100
Edefocus(i)= Etank(i-1)+Delta100(i)-Emax_tank

Figure 0.14 Thermal storage control strategy flow-diagram

Results of the annual simulation reported in Table 0.4 show a high capacity factor due to the effect of very high solar multiple coupled with a large thermal storage.

$E_{SF_{incident}}$ [MWh]	1'082'447	$\eta_{opt_{annual}}$	55.46%
$E_{Receiver_{incident}}$ [MWhth]	600'290	$\eta_{thermal_{annual}}$	84.42%
$E_{HTF_{theoretical}}$ [MWhth]	506'753	$\eta_{defocus_{annual}}$	94.47%
E_{PB} [MWhth]	478'738	$\eta_{PB_{annual}}$	45.69%
$E_{el_{produced}}$ [MWhe]	218'752	$\eta_{SF\,aux_{annual}}$	99.99%
$E_{el_{delivered}}$ [MWhe]	218'736	$\eta_{sol\,to\,el}$	20.21%
h_{eq} of operation	7040 h	h_{eq} of defocus	412 h
CF	0,804	Percentage power defocused	5.53%

Table 0.4 Results of the annual simulation

Conclusions

In this work a SPT plant employing sodium as HTF and sCO$_2$ cycle in the power block was designed, various parameters where optimized and a parametric analysis on TIT was performed in order to asses its impact on solar to electric efficiency. From this analysis it emerged that, with this configuration, increasing the TIT in the range [723.6;785]°C the overall solar to electric efficiency monotonically increases.

The turbine feasibility study showed that a TIT higher than 725°C is not feasible without the refrigeration of the rotor of the turbine which, in this case, is not convenient considering the trade-off between the increase in efficiency and the higher turbine complexity. Therefore, in the ultimate design a TIT of 725°C was considered.

The analysis on heat exchangers showed how PCHE are not suitable for the PHX, due to high temperature and pressure and the incompatibility with liquid sodium. Therefore a shell and tube HX must be used as PHX, despite its larger volume and cost.

Lastly the receiver mechanical analysis showed that if tube maximum temperature is limited below 871°C the mechanical stresses experienced by the tubes can be sustained by the chosen material (Haynes 230).

The annual analysis resulted in an overall solar to electric efficiency equal to 20.21% with a capacity factor of 0.804.

From this thesis work it emerged that components limitations are often not technical but economical, indeed more performing materials and more complex solutions can often be employed in order to increase performances despite a very high increase of the cost. Although, some solutions which present very high

performances are not even considered by the industry sector due to their prohibitive costs.

Choices taken in this study favoured efficiency over reduced cost, for example high temperature and pressure in the sCO2 cycle make unfeasible the employment of hybrid heat exchangers for the PHX, which must be designed as a very expensive shell and tube HX. Other examples are the solar multiple and storage size which should be optimized through a techno-economic study, while in this study were pushed to very high values (SM of 3 and storage size of 17.5h), to increase the capacity factor.

For these reasons the author advices a future economic study, coupled to this one, in order to assess equipment cost and compare plant LCOE with the SOA of CSP plants. In the cited study, plant layout and parameters chosen should be optimized considering LCOE instead of efficiency.

Another essential development according to the author opinion is the increase of plant nominal power, indeed, SPT plants which are being built in the latest years are larger in size with respect to the one analysed in this study, their nominal power ranges around the hundred of Megawatts to exploit the scale effect decreasing LCOE. If sodium receiver coupled with sCO2 cycle needs to be commercially competitive with other CSP layouts, nominal power should increase up to at least 100 MW. Future studies should focus on technical challenges arising from an increased design power.

Lastly, once the competitivity of this kind of plant has been assessed, a study focused on the partial load performances of the sCO2 power block should be performed, in order to assess if this kind of plant configuration can be competitive also in a future scenario, when electricity produced by CSP plants will be used to cover negative production peaks of the intermittent renewable sources.

Acronyms

ASME American Society Of Mechanical Engineers

A-USC Advanced Ultra-Supercritical

CF Capacity Factor

CR Concentration Ratio

CSP Concentrated Solar Power

DNI Direct Normal Irradiation

DSG Direct Steam Generaing

EM Electro-Magnetic

ESE Egineering Services For Energy

FPHE Finned Plate Heat Exchanger

FTM Franco Tosi Mecchanica

GE General Electric

H2X Hybrid Heat Exchanger

HP High Pressure

HRU Heat Rejection Unit

HT High Temperature

HTF Heat Transfer Fluid

HTR High Temperature Regenerator

HX Heat Exchanger

IEA International Energy Agency

IP Intermediate Pressure

ISP Image Size Priority

LCOE Levelized Cost Of Energy

LFR Linear Fresnel Reflector

LP Low Pressure

LT Low Temperature

LTR Low Temperature Regenerator

NFP Number Of Flow Paths

NIST National Institute Of Standards And Technologies

NP Numpber Of Passes Per Path

NPP Number Of Parallel Panels

NREL National Renewable Energy Laboratory

OEM Original Equipment Manufacturer

OPEX Operating Expense

PB Power Block

PC Partial Cooling Cycle

PCHE Printed Circuit Heat Exchanger

PDS Parabolic Dish Systems

PERS Potential Energy Recovery System

PHX Primary Heat Exchanger

PTC Parabolic Trough Collector

RC Recompressed Cycle

RMCI Recompressed Main Compressor Intercooling Cycle

RPR Ratio Of Pressure Ratios

SC Simple Cycle

sCO2 Supercritical Carbon Dioxide

SM Solar Multiple

SOA State Of Art

SPT Solar Power Tower

SR Split Ratio

SSPS Small Solar Power Systems

TES Thermal Energy Storage

TESS Thermal Energy Storage System

TIT Turbine Inlet Temperature

US United States

USC Ultra-Supercritical

UTS Ultimate Tensile Strength

YS Yield Strength

List of figures

23

List of Tables

1 Introduction

2019 was a year of growing awareness on the subject of climate change, movements all around the world raised from youth asking for a higher attention on the subject. It is nowadays widely accepted the relation between human activities and the growth of GHG emissions, especially CO_2 whose concentration hasn't been as high as now (407.4 ppm) in 3 millions years [24], in 1950 the concentration of CO_2 in atmosphere surpassed 300 ppm, the highest concentration ever registered in the previous 800'000 years (Figure 1.1). The increasing concentration of GHG in the atmosphere leads to an increase in global average temperature which can have a strong impact on human and other species life on earth.

Global climate change has already had observable effects on the environment. Glaciers have shrunk, ice on rivers and lakes is breaking up earlier, plant and animal ranges have shifted and trees are flowering sooner. Effects that scientists had predicted in the past would result from global climate change are now occurring: loss of sea ice, accelerated sea level rise and longer, more intense heat wave [25]. To address climate change, countries adopted the Paris Agreement at the COP21 in Paris on 12 December 2015. The Agreement entered into force less than a year later. In the agreement, all countries agreed to work to limit global temperature rise to well below 2 degrees Celsius, and given the grave risks, to strive for 1.5 degrees Celsius. While it's important to note that a warming world will have year-to-year variations due to natural variability (so not every year will be warmer than the one before) 2019 was 1.22°C above the pre-industrial baseline temperature. To keep warming below 2°C will, hence, necessitate a global effort to drastically reduce emissions.
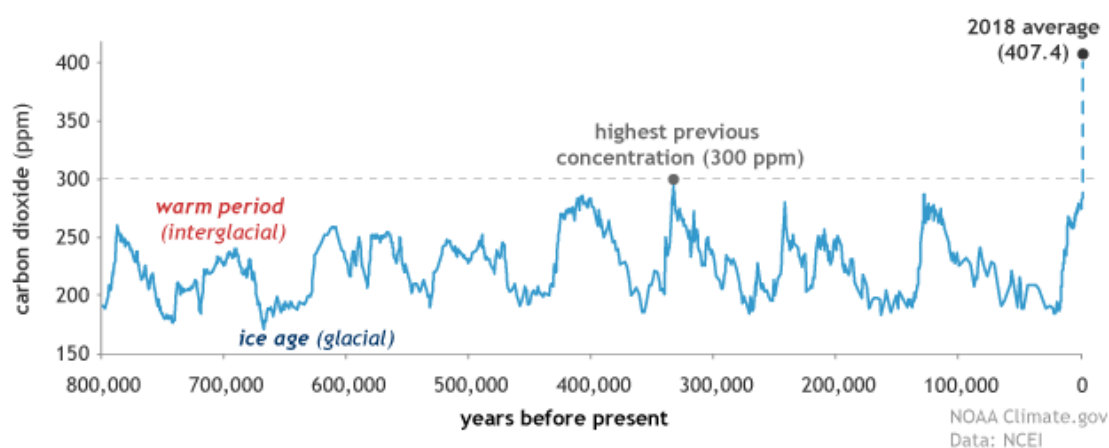
Figure 1.1 Global atmospheric carbon dioxide concentrations (CO_2) in parts per million (ppm) for the past 800,000 years. The peaks and valleys track ice ages (low CO_2) and warmer interglacials (higher CO_2). During these cycles, CO_2 was never higher than 300 ppm In 2018, it reached 407.4 ppm. On the geologic time scale, the increase (blue dashed line) looks virtually instantaneous [24].

About 40% of CO_2 emissions are ascribable to the heat and electricity production (IEA 2016). Other concerns about over-exploitation of fossil fuels for energy productions are that natural resources are limited and non-equitably distributed among countries. These reasons are pushing for a transition of the energy sector to renewable sources.

In the last two decades renewable energy production increased reaching 26% of world electricity production in 2018 (Enerdata [26]), this growth is mostly ascribable to solar PV and wind power production, especially in OECD countries where the hydroelectric sector was already fully developed in the 90s.

The higher penetration on the electricity grid of un-dispatchable and unpredictable renewable sources, such as PV and wind, introduces new challenges in the management of electricity demand and production. Concentrated solar power (CSP) is of particular interest because it can provide carbon-free, renewable and dispatchable electricity thanks to the easy coupling with a thermal energy storage system.

Despite these advantages this technology is not competitive on the market, due to its high LCOE (0.18 USD/kWh in 2018, IRENA [2]) with respect to other renewable technologies such as wind and PV (on-shore wind 0.127 USD/kWh, on-shore wind 0.056 USD/kWh, solar PV 0.085 USD/kWh [2]). For this reason in the latest years many studies aimed at reducing CSP cost of electricity were made, with the result that LCOE reduced of 26% between 2017 and 2018 [2].

Strategies to reduce the cost can be improving overall conversion efficiency or increasing the number of equivalent working hours by the usage of a larger thermal storage.

Among CSP technologies, SPT is the most interesting due to its higher concentration ratio and the possibility to use molten salts or other HTF with higher solidification temperatures than the ambient one. Solar salts currently employed in SPTs reach 565°C, in order to increase furthermore maximum HTF temperature affecting positively power block efficiency, other fluids must be considered such as liquid metals, which can reach temperatures as high as 800°C.

In parallel to the research of new HTFs, closed-loop sCO_2 cycles are currently being researched for application in fossil, nuclear and CSP applications. These cycles can reach higher temperature and potentially higher efficiencies than steam cycles, currently used in SPT plants; moreover they have much lower sizes and weights than their steam equivalent, due to higher CO_2 density. This reduction in size corresponds to a lower thermal mass, thus shorter thermal transients, and to a lower cost.

Many articles can be found in literature about thermodynamic studies of sCO_2 cycles [27]–[35], sCO_2 cycles coupled with CSP [6]–[12], [36] or even sCO_2 cycles coupled with CSP and

liquid sodium as HTF [3], [4], [12], [37]–[40], most of these analyses base their assumptions on previous studies, without verifying them with manufacturers.

The purpose of this thesis is to verify that the assumptions made in previous studies are realizable in an industrial context, and to give an indication on potential problems which must be addressed when designing this kind of plant, through research in specific components literature and contacts with manufacturing companies. Finally it aims to realize a design which accounts for real limits of the materials and efficiency of the components assessing the plant design and annual performances.

1.1 Work outline

This thesis starts, in chapter 2, from the investigation of various options of type of plant, heat transfer fluid and power block working fluid and configuration, from performance data found in literature, in order to choose the most performing layout and analyse its limits.

In chapter 4 the cycle chosen was modelized with the parameters and assumptions found in literature in order to verify that, accounting to physical laws, the results are approximately the same.

In addition, a detailed model of the receiver was made in order to develop an accurate optimization of its geometry and the evaluation of pressure losses, moreover the solar field was modelized with SolarPILOT to obtain optical efficiency data and realistic flux maps. In this preliminary design many parameters of the power block, receiver and solar field were optimized in order to check limits of the optimized plant. In this design some preliminary limits, such as maximum material and HTF temperature, were accounted already in order to start from a realistic layout.

In chapter 5, the study of specific components is reported, research focused on materials and their mechanical and temperature limits, in addition specific attentions needed with dealing with sodium as HTF and CO_2 as working fluid are explained. The help of some manufacturing companies was precious for this part of the work, indeed part of the components manufacturing limits come directly from the industry practice. In section 5.2, a new design accounting for limits found in section 5.1 is reported, design efficiency and power production can be found in this section.

Lastly the annual simulation is performed in chapter 6, the off design behaviour of receiver, solar field, HRUs of the power block and of the HTF pump is evaluated and a thermal storage filling strategy is modelized. The annual simulation takes ambient data from a location near Las Vegas (35.57°N 115.47°W) and calculates every half an hour the energy hitting the field, hitting the receiver, entering the HTF, produced by the PB and lastly the energy delivered to the grid, calculating the annual production and efficiencies.

2 Concentrated solar power plant

Concentrated solar thermal technologies are based on the concept of concentrating solar radiation to produce a stream of hot fluid which can then be used in order to produce electricity using conventional power cycles. Solar energy on the ground has relatively low density, about 1000 W/m^2, therefore it is fundamental to concentrate it in a smaller area in order to have higher temperature and to avoid the complete dispersion of the heat in the colder surrounding air.

CSP systems can use only direct radiation, and not the diffuse part of sunlight because this cannot be concentrated.[41] Indeed the light must to be coming from a specific direction in order to be able to reflect it on a target.

The CSP technology can be classified into parabolic trough collector (PTC), linear Fresnel reflector (LFR), solar power tower (SPT) and parabolic dish systems (PDS), according to the way in which they focus the sun's rays , the shape of the receiver and whether the receiver is fixed or mobile. In parabolic trough and linear Fresnel systems, the receiver has the geometric form of a line and the mirror tracks the sun along one axis (line focusing systems); in tower and dish systems, the receiver can be conceptually seen as a one dimensional system and the mirror tracks the sun along two axes (point focusing systems). The receiver is fixed in linear Fresnel and tower systems and it is mobile in parabolic trough and dish systems. [42]
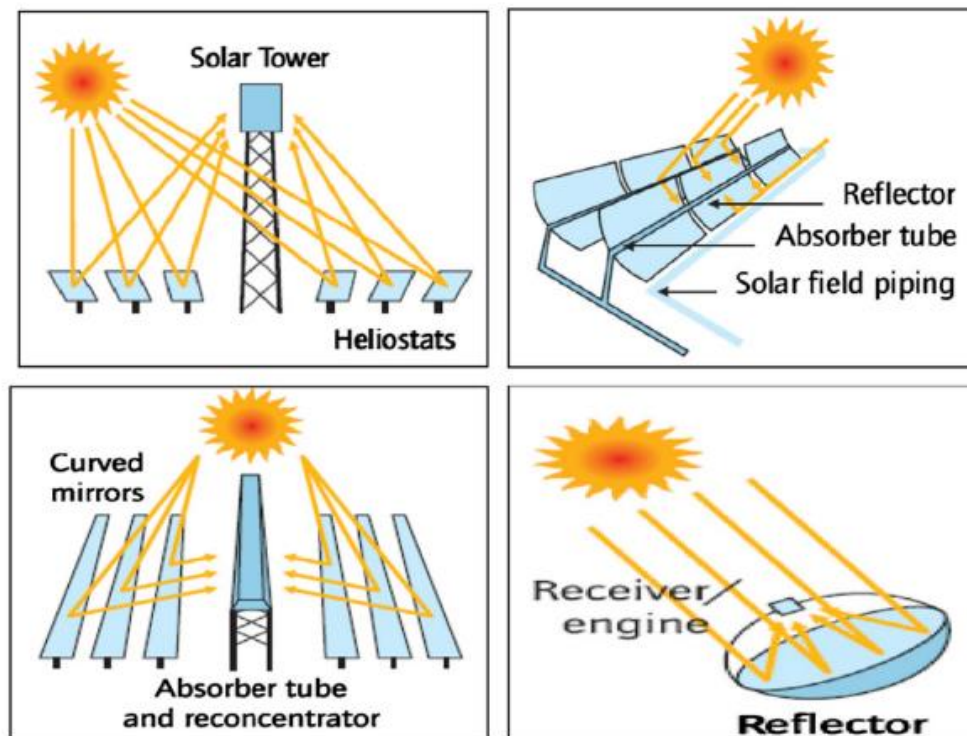
Figure 2.1 Currently available CSP Technologies:(a) STP; (b)PTC; (c) LFR; (d) PDC.[43]

31

Line focusing systems are easier to handle, in fact the PTC is the most used CSP technology in the world, although SPT technologies are gaining much interest because they can reach a higher concentration factor, hence achieve higher temperatures which ensures a higher efficiency of the bottoming cycle, moreover they have lower operating costs and good scale-up potential.

In this thesis only the Solar power tower technology has been considered because it is the only one which can reach the Temperatures and the concentration ratio investigated.

A solar tower system is composed of four main parts, as can be seen in Figure 2.2 where the simplified scheme of a molten salt CSP plant is reported:

- The collector system made of mirrors, called heliostats, which reflect the light on a target.
- The receiver system whose function is to absorb the light collected by the heliostat field and transfer it to a heat transfer fluid (HTF).
- The thermal storage system which is needed in order to keep the inlet thermal power in the power block constant and not dependent from the availability of solar light. Storage is also used in order to increase the hours of operation of the power block thus decreasing the LCOE.
- Lastly the power block system which comprises a region consisting in a heat exchanger used to exchange thermal power from the receiver heat transfer fluid to the cycle working fluid and a thermodynamic cycle which converts the thermal energy of the working fluid in electrical energy.
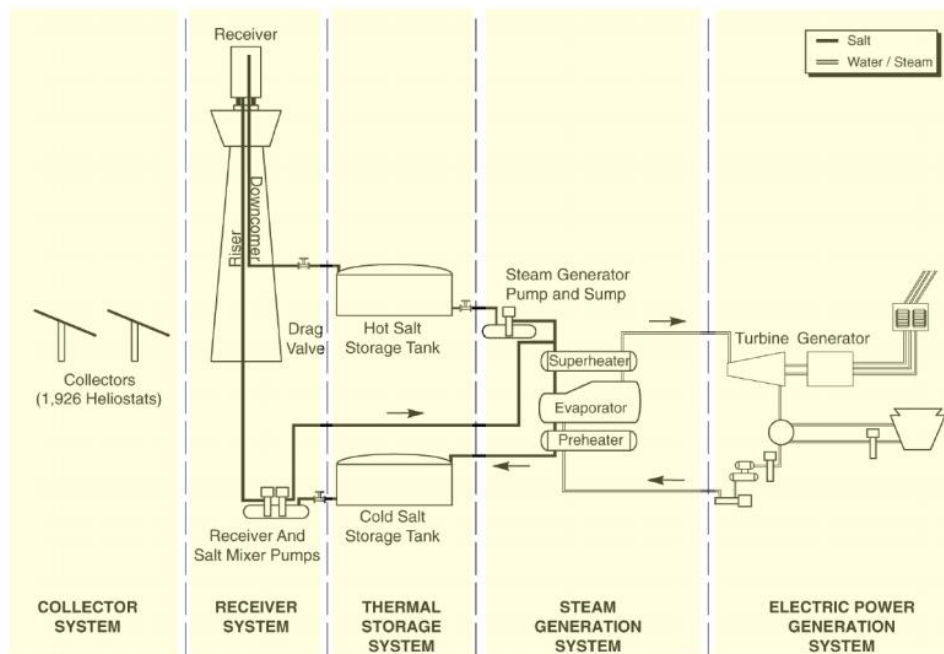
Figure 2.2 Simplified plant scheme of a molten salt solar tower CSP plant[44]

2.1 Collector system

Central receiver (or power tower) systems use a field of distributed mirrors, heliostats, that individually track the sun and focus the sunlight on the top of a tower. Two direction tracking allows the heliostats to follow the sun azimuth and elevation.

Each heliostat can be made of more than one flat panel or just one big concave mirror [45]. The effective area of the reflective surface of the heliostat is only the normal one to the incident ray and therefore it is smaller than the actual one, in order to obtain the effective area of each heliostat its geometrical area must be multiplied by the cosine of the incident angle. With an incident angle of 90° the reflective area is equal to the geometrical one, therefore to the design of the heliostat field must aim at keeping the average annual incident angle as close as possible to 90°. The annual cosine efficiency, which depends on the latitude at which the plant is located, must be maximized, resulting in two possible different layouts:

- Surrounded field, which is best for places close to the equator. The heliostats are put in concentric circles around the tower. At these latitudes the sun has a high altitude throughout the whole year, hence the south side of the field (for fields in the northern hemisphere) is not penalized too much by a high variation of the incident angle due to the revolution of earth around the sun.
- North field, more suitable for higher latitudes. The field is placed in the north direction with respect to the tower, in order to better exploit the incoming radiation, since the low sun position in the sky.

The definitions above are given for latitudes in the northern hemisphere, for the southern one the directions must be inverted. Other than the two reference configurations there is a broad spectrum of solar fields which are a compromise between these two depending on the location.

Not the whole solar radiation incident on the heliostat field reaches the absorber surface, a part of it is lost due to these reasons:

- First of all, the discrepancy from actual area of the heliostats and their normal surface (cosine efficiency).
- The actual reflectivity of mirrors is not 1.
- Part of the light reflected from one mirror could be blocked from a close by mirror on its path to the solar tower.
- In some parts of the day in which the solar altitude is low the shadow of a mirror can reach the surface of another mirror shading the solar light for it. The farther apart are the mirrors the smallest is the impact of this effect.
- The distance of the heliostats from the tower can't be too high due to increasing attenuation of the atmosphere. Indeed, part of the light reflected is absorbed by atmosphere between the heliostat and the tower.
- The last source of inefficiency is the spillage. When sunlight is reflected from the mirror it is not reflected in a straight beam, its light has a Gaussian distribution in all direction, therefore part of the reflected light doesn't reach the receiver[45].

The overall conversion of energy of the solar energy to electric energy is the result of two different processes: a solar to thermal process which happens in the solar field and tower and a thermal to electric process which happens in the power block.

The thermal to electric process consists in a thermodynamic cycle, whose theoretical maximum efficiency is achieved with Carnot cycle:

$$\eta_{th-el,max} = \eta_{carnot} = 1 - \frac{T_{amb}}{T_{max}}$$

Where T_{amb} is the ambient temperature and T_{max} is the maximum temperature of the working fluid in the power block.

The higher the maximum temperature, the higher the Carnot efficiency (Figure 2.3), therefore the better the performances of the power block.
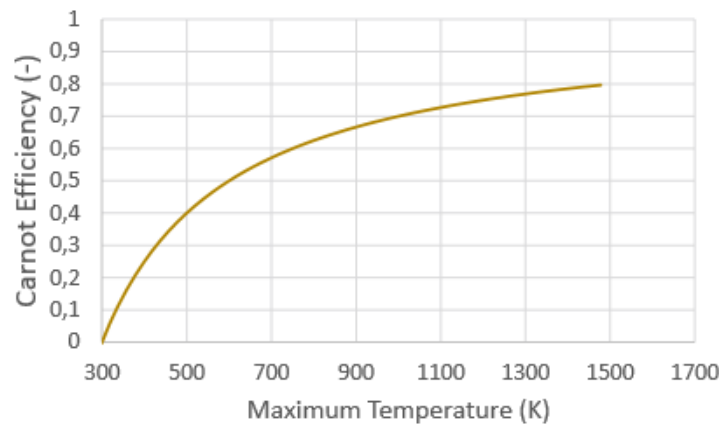
Figure 2.3 Carnot efficiency [44]

The solar to electric process has an efficiency which depends from the optical loss of the solar field and receiver and from the losses due to thermal dispersion:

$$\eta_{sol-th} = \eta_{opt} * \eta_{thermal}$$

Where, η_{opt} is the optical efficiency of the solar field, $\eta_{thermal}$ is the thermal efficiency of the receiver, expressing the ratio between the actual thermal power transmitted to the HTF and the thermal power hitting its surface, strongly dependent on the maximum temperature of the HTF. Indeed the thermal losses can be evaluated as:

$$\dot{Q}_{loss} = \dot{Q}_{rad} + \dot{Q}_{conv} = \sigma \varepsilon A_{rec}(T_{rec}^4 - T_{amb}^4) + h A_{rec}(T_{rec} - T_{amb})$$

Where $\dot{Q}_{rad}$ is the radiative loss and $\dot{Q}_{conv}$ is the convective loss, they both depend from the surface area of the receiver and the temperature of the receiver walls. σ is the Stefan-Boltzmann constant, ε the emissivity of the receiver walls and h is the convective heat transfer coefficient.

The thermal efficiency can be consequently evaluated:

$$\eta_{th,rec} = \frac{\dot{Q}_{rec} - \dot{Q}_{loss}}{\dot{Q}_{rec}} = 1 - \frac{\sigma \varepsilon A_{rec}(T_{rec}^4 - T_{amb}^4) + h A_{rec}(T_{rec} - T_{amb})}{\eta_{opt} A_{SF} DNI} \qquad Eq. \ 2.4$$

As the mean logarithmic temperature of the heat transfer fluid in the receiver increases the thermal efficiency will decrease.
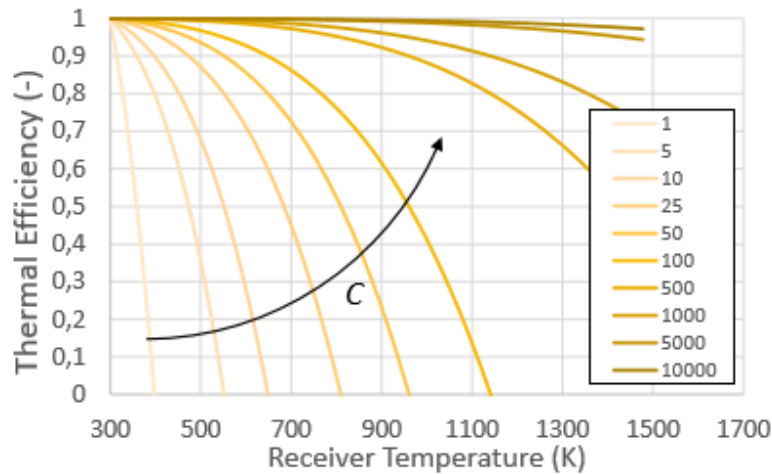
Figure 2.4 Thermal efficiency of the receiver [44]

The maximum temperature of the cycle, therefore, must be chosen in order to maximize the total solar to electric efficiency.

In order to decrease as much as possible the thermal losses with a constant optimized temperature the heat exchanging area (receiver area) must be reduced without decreasing the Power absorbed by the receiver. This results in an increase in the concentration ratio, defined as:

$$CR = \frac{A_{SF}}{A_{rec}} \qquad Eq. \ 2.5$$

As shown in Figure 2.5 the higher the concentration ratio the higher the optimal temperature and the product of thermal efficiency times cycle efficiency.
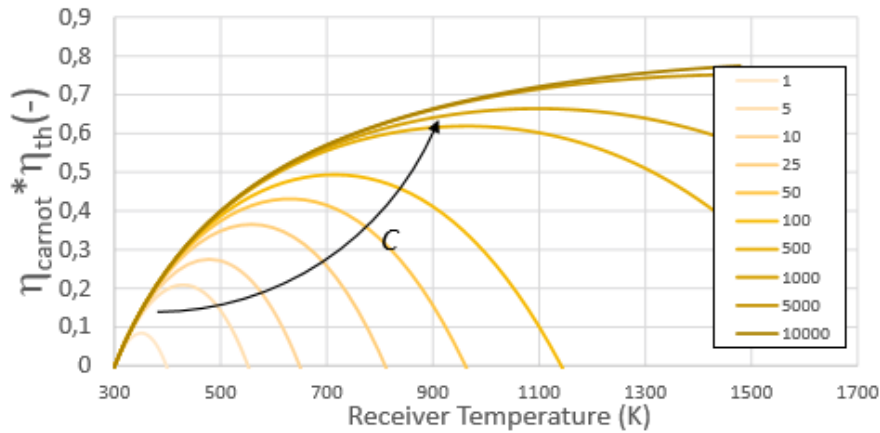
Figure 2.5 Overall efficiency [44]

SPTs show the main advantage of a higher concentration ratio with respect to linear focus technologies. Ideally all concentrators would be able to achieve extremely high concentration ratios, however in practice the concentration ratio is limited due to the finite solid angle of the sun in the sky on Earth, leading to a non-zero divergence angle of sunlight at the Earth's surface (θ_{sun}).

The maximum achievable concentration ratio $Cmax$ is determined by the geometrical conservation of energy for a solar concentrator:

$$C_{max,1ax} = \frac{\sin \psi_{rim}}{\sin \theta_{sun}}$$

<div align="right">*Eq. 2.6*</div>

$$C_{max,2ax} = \left(\frac{\sin \psi_{rim}}{\sin \theta_{sun}}\right)^2$$

<div align="right">*Eq. 2.7*</div>

Where $C_{max,1ax}$ and $C_{max,2ax}$ are the maximum concentration ratios for one-axis and two-axis tracking systems respectively, and θsun is the divergence half angle of sunlight on earth, $\theta_{sun} = 16' = 4.653 * 10^{-3}$ rad.

The rim angle (ψ_{rim}) refers to the largest angle at which reflected sunlight from the concentrator strikes the receiver (see Figure 2.6).
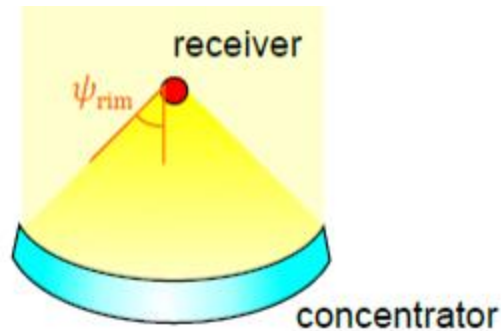
Figure 2.6 Concentrator rim angle ψ_{rim} [46]

For a flat receiver, the largest possible rim angle is $\pi/2$, therefore maximum concentration ratio is:

Real

$$C_{max,1ax} = \frac{1}{\sin\theta_{sun}} \cong 210$$

$$C_{max,2ax} = \left(\frac{1}{\sin\theta_{sun}}\right)^2 \cong 43000$$

concentrators cannot achieve such high concentration ratios due to imperfect tracking and imperfections in reflector surfaces [46].

2.2 Receiver system

Central receivers are the technology associated with point-focus heliostat field CSP systems.

These systems are often referred to as "power towers," since the receiver typically sits atop a large tower which the heliostats reflect sunlight to. Heliostat fields have large concentration ratios around 1000 in order to decrease as much as possible thermal losses.

There are two primary designs for central receivers: external receivers and cavity receivers, both of them are shown in Figure 2.7.
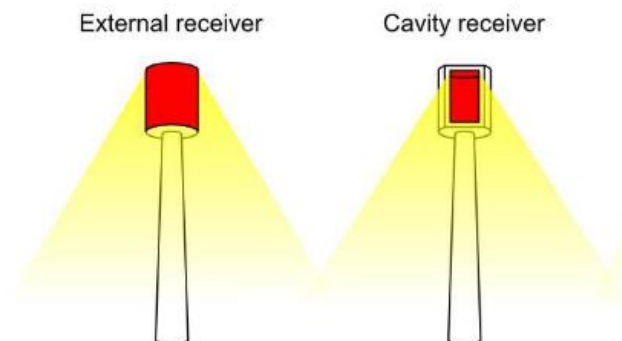
Figure 2.7 Diagrams of different central receiver configurations, with red denoting the absorbing surface. [46]

- Cavity receiver

  In a cavity receiver, sunlight is focused on an aperture leading to an internal cavity where the sunlight is absorbed. In cavity receivers welded tubes are kept inside a cavity in order to reduce convection losses. [47]

  With this kind of receivers the heliostat field is only on the side of the receiver which the aperture faces, e.g., in the northern hemisphere the aperture would face north and the heliostat field would only be on the north side of the receiver [4].

  For cavity receivers, the absorptance is naturally high due to the cavity geometry, indeed light which enters through the aperture is trapped inside the cavity being absorbed at some point from the large interior surface, it is unlikely for it to be reflected back out of the aperture. In order to increase furtherly the absorbance, the internal cavity is coated with an absorber paint, the most common one which is used is Pyromark 2500, which has an absorbance of around 95% [48].

- External receiver

  In an external receiver the absorbing surface is on the outer surface of the receiver, which typically has a cylindrical shape, and the heliostat field can completely surround the central receiver. [4]

  The external central receiver is configured as a 360° cylindrical tubular receiver. The vertical thin-walled tubes are arranged in panels. Depending on the flow path configuration there can be one or more HTF paths in parallel, each path is a series of up-flow and down-flow panels. In each panel several thin tubes in parallel are linked by a header.

  Due to the large exposed area it is very important for the coating material not just to have a high absorbance but also to have a low emittance. Unfortunately, these two characteristics are strictly linked to each other and even the most common absorber coating, Pyromark 2500 has a fairly high emittance (>85%) at elevated operating temperatures.

  Although even if the high emittance is a clear disadvantage of this coating, it is the most used one because it has high thermal stability and due to the high temperatures, large heat fluxes, and large number of thermal cycles experienced by central receivers, the importance of reliability makes it a competitive option.

2.3 Heat transfer fluid

In solar thermal systems, sunlight is focused on a receiver where it is absorbed and ultimately converted to thermal energy. The thermal energy is typically delivered to a heat transfer fluid (HTF) through convection.

When absorbed photons originating from the sun thermalize in the receiver, the temperature will rise according to its heat capacity unless an equivalent amount of heat is removed from the receiver. At a steady-state operating temperature, the HTF removes continuously the heat generated due to the absorption of photons.

If no thermal storage is present, , the HTF can ether flow directly to heat exchanger, where it is transferred to a different working fluid which operates in the power block (indirect configuration), or it can be directly expanded in a turbine (direct configuration).

The HTF thermo-physical properties have a strong influence on plants' performances, cost and reliability, as the working fluid performances highly impact the performances of the power cycle. The properties for a good HTF could be different from the ones of a good working fluid.For this reason, an indirect cycle configuration is more advisable, permitting to select the most appropriate fluid for each part of the system.

2.3.1 Desired characteristics for a HTF

The heat transfer fluid ideally has to comply with the following specific requirements:

- **High thermal stability**
  As the concentration ratio is increased the optimal temperature and the solar to electric efficiency increases, it is therefore important for the heat transfer fluid to be able to sustain, without degrading, high temperatures.
- **Low freezing point**
  During night-time the temperature can be very low in desert areas where CSP plant are usually built, moreover the absence of irradiation from the sun could make the temperature of the fluid in the receiver fall almost to ambient temperature. In these conditions the fluid present in the pipes could solidify. Due to the absence of a good HTF with very low solidification temperature, some solutions are adopted: in solar tower the HTF is drained every night from the solar tower and stored in an insulated tank, in most CSP plant, also a heating system is used. A low freezing point is still helpful to reduce the heat tracing expenditure.
- **Good heat exchange**
  A good heat transfer is favoured by a high thermal conductivity and high convective heat transfer coefficient.
  The higher the concentration ratio on the solar receiver, the higher will be its thermal efficiency and the optimal temperature will be higher, with a consequent higher power block efficiency, but there is a limit imposed by thermal stress resistance of the material of the receiver's tubes. A heat transfer fluid with good heat transfer properties allows to reduce the temperature difference between the flow bulk temperature and the wall temperature of the receiver, rising the limit of concentration ratio, related to the maximum incident heat flux, and temperature.

- **high volumetric heat capacity and density**
  These properties are important to allow high heat fluxes at reasonable mass flow rates, moreover they are also good in case of direct thermal storage because a lower quantity of fluid can be used to store the same amount of heat.
- **Low Viscosity**
  Important in order to minimize friction in the receiver tubes. The lower pressure drop which is obtained allows a contained pumping power.

Other factors which need to be taken into account are:

- Operational aspects as safety (Low flammability and toxicity) and corrosive behaviour.
- Low cost per kilogram. Since a large amount of HTF is required to operate a CSP plant, its cost can have a strong impact on the overall cost of the plant.[46][3][12]

2.3.2 Heat transfer fluid types

Since a single HTF which has all of these characteristics hasn't been found yet, many fluids were analysed in order to find the best compromise.

The HTFs can be classified into five main groups based on the type of materials: gases, water/steam, thermal oils, molten-salts and liquid metals [49]. Figure 2.8 provides a comprehensive list of working temperatures of various HTFs.
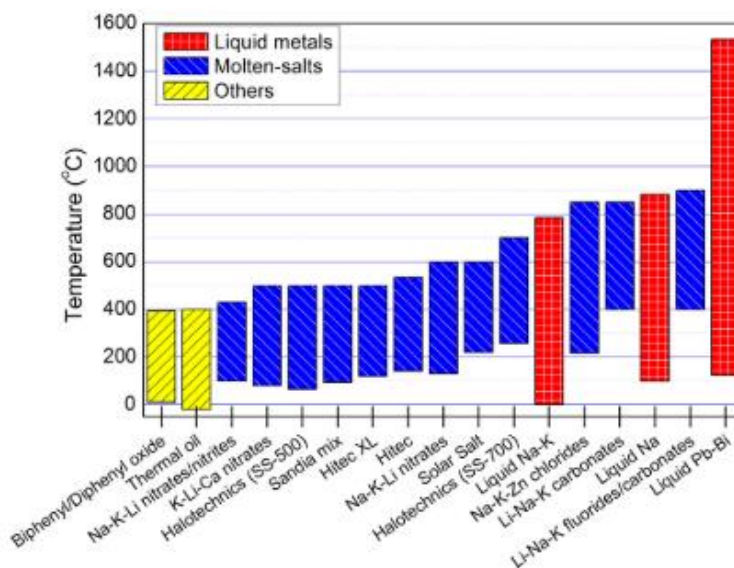
Figure 2.8 Operating temperature range for various HTFs [49]

2.3.2.1 Gases

Air is a relatively uncommon HTF in large CSP plants. Only one commercial scale system has been constructed, a 1.5 MWe precommercial receiver built in Jülich, Germany (Jülich solar tower) which began operation in 2009 [49].

The pressurized-air receivers currently studied are designed to heat compressed air to the entrance conditions of a gas turbine which then directly expands the gas in a direct open cycle. The biggest advantage of this HTF is the abundance and cost-free nature of atmospheric air and the wide temperature range in which it can operate, moreover it is environmentally safe, non-corrosive and easy to handle, indeed air gas turbines are a well-known technology.

Drawbacks are the very poor heat transfer properties: low heat transfer coefficient limits the maximum irradiance on the receiver tubes, and thus the concentration ratio, while small thermal conductivity causes a large temperature difference between the wall and the bulk flow, meaning both a low maximum temperature of air, given a limit in maximum wall temperature, which implies low thermodynamic efficiency of the cycle and high thermal stresses on the tube wall.

Although, since air has very low dynamic viscosity compared to other liquid HTFs such as molten salts or liquid metals, its velocity in vessels can be higher in order to enhance heat transfer, without the penalization of high pressure losses.[49].

Another drawback of using air is the large pumping power required due to the high pressure needed and high specific volume.

In addition to air, some other gases including helium and supercritical CO_2 (sCO_2) have also been investigated for use in CSP systems as HTFs.

Helium was widely used as a coolant in high temperature nuclear reactors therefore there is some knowledge about its use, it is also relatively affordable, since it is obtained in natural gas extraction processes[49].

Similarly to air, helium also has a broad temperature range of operation, reaching high temperatures it is possible to obtain higher thermodynamic efficiency of the cycle. Other advantages of helium for large power plants are that it is chemically inert and its specific heat is five times that of air[13]. The major disadvantages are the low heat capacity and heat transfer between the fluid and the internal surfaces of the receiver tubes. Therefore, high pressures and high fluid velocities are necessary.[49]

Carbon dioxide is a good candidate because it is a non-flammable and non-toxic fluid; it is widely available, in sufficient quantities and at a very reasonable cost.[13]

Supercritical CO_2 has the potential to be operated at very high temperatures and can be used both as HTF for the solar collector and as working fluid for the power block simplifying the power system configuration [7]. s-CO_2 cycles have been traditionally considered for application in nuclear power plants, but recently they have become increasingly popular also in relation to their potential application in CSP plants, due to the high performance that can be achieved at moderate maximum temperatures, and their contextual power block compactness and simplicity.[7]

The CO_2 supercritical state (s-CO_2) is observed at 73.8 bar and 31°C and favourable heat transfer and viscous supercritical properties permit to design innovative conversion systems. One challenge of using CO_2 as the receiver heat transfer fluid is its integration with storage.

Indeed, thermal storage of supercritical fluids was shown not to be viable, thus requiring intermediate heat exchange with a separate storage medium. In addition, efficient supercritical CO_2 cycles require high pressure, thus thicker tube walls and new welds are needed, moreover high pressure losses are expected. Therefore, it seems to be more suitable for central tower systems as there are extensive pipelines used in PTC and pressure losses would be prohibitive.[13]

2.3.2.2 Water/steam

First studies regarding water/steam as HTF in direct plant configurations, such as direct steam generating (DSG) parabolic troughs, date back to 1980s when the DISS test loop at the Plataforma Solar de Almerìa was erected[50]. The Solar One tower as well as the first two commercial solar tower power plants, PS10 and PS20 with a power rating of 10MWe and 20MWe used saturated steam as the HTF. The first two-large scale linear Fresnel solar power plants, PE1 (1.4MWe) and PE2 (30MWe), rely on the same HTF but evaporate the water in a line focusing system.[51]

Water presents many advantages as heat transfer fluid; it is cheap, non-toxic, and it presents suitable heat transfer properties. Since a heat storage with pressurized steam is not a feasible solution, it is commonly used in direct steam generation plants (DSG), where acts as both HTF and working fluid with consequent lower investment cost. This simplified system also has improved efficiency with respect to the indirect configuration, because in the latter one the additional heat exchanger introduces a loss.[12][49]

On the other hand, the implementation of the DSG technology shows some technical issues related to the hydrodynamic behaviour of a two-phase flow, as water faces the transient phase-change processes in the receiver tubes. Moreover, the employment of superheated steam can cause extreme tubes superheating in transient conditions due to its low heat transfer coefficient, that is of the order of $1/40_{th}$ with respect to the one of liquid water. For this reason, applications are limited to saturated vapor, requiring higher pressure to achieve the temperature target.[12]

2.3.2.3 Thermal oils

CSP plants initially started using synthetic oil, most widely known under the brand names Therminol VP-1 or Dowtherm A, in order to avoid the high pressure requirement and phase transition when using water. [13]

Their advantages are a low viscosity, that helps in containing the pumping power requirements, high heat capacity, which makes them suitable also for energy storage, and low freezing point, around room temperature, hence they can be used also in PTC.

There are three kinds of thermal oils: mineral oils, silicon oils and synthetic oils, all these three oils have almost the same thermal conductivity $\sim 0,1\frac{W}{mK}$ while the cost varies being the mineral oils the cheapest and silicone oils the most expensive. [49] In general, with respect to other HTF they are very expensive.

Moreover, these oils are only thermally stable to approximately 400◦C, after this limit the hydrocarbons break down producing hydrogen, and this is the reason they are not commonly used for high temperature and highly efficient solar thermal systems. Other disadvantages are flammability and degradation over time, which can increase makeup fluid requirements, reduce overall fluid lifetime, and cause build-up of sludge or other by-products that reduce the system heat transfer efficiency and increase maintenance costs.

2.3.2.4 Molten salts

Solar molten salts are salt mixtures, mainly nitrates, which can be used for thermal storage applications as well as heat transfer fluids thanks to their chemical characteristics. Molten salts also have properties comparable to water at high temperature including similar viscosity and low vapor pressure. Moreover, molten salts are cheaper and have less environmental impact than synthetic oil: they are non-polluting, non-flammable, more abundant and offer cost savings because of reduced thermal tanks and piping.

Heat transfer characteristics of molten salts are fairly good and this is why many SPT plants which are being designed and enter in operation in this period use this type of HTF, in particular Solar Salt represent the current SOA. The reasonably high density and mediocre specific heat capacity enable a low volume flow, although the low thermal conductivity leads to elevated temperatures on the outside of the receiver pipes, hence to high radiation losses and to the need of more resistant, thus expensive, materials for the receiver's tubes and the piping system. The heat transfer between pipe and HTF can be improved by increasing the fluid velocity and turbulence, but this increases pressure losses.

The major challenge of molten salts is their high freezing point which leads to operations and maintaining costs for freeze protection. The currently used synthetic oil freezes at about 15 °C, whereas ternary and binary molten salts freeze in the temperature range 120–220 °C. The high solidification temperatures of liquid salts are problematic especially in line-focusing CSP plants (parabolic trough or linear Fresnel receivers) because the HTF would freeze during the night or in times of low irradiation and it is too difficult to drain the horizontal tubes; whereas in SPT plants, the salt will normally be drained into an insulated tank while filling the receiver with gas. However, salt freezing, for instance, due to blocked valves, can still occur and cause failures. Other possible solutions besides draining include trace heating or circulation of stored hot salts but all of these would result in higher heat losses, electrical power consumption and/or investment costs.

To evade this complication, research is being done on liquid salts with lower melting points. [51] The problem with these new salts is that the solidification temperature is strictly related to the stability limit temperature, therefore, decreasing the lowest allowable temperature also decreases the maximum temperature of the salt penalizing the efficiency of the cycle.

Recently, increasing attention is paid on applications of molten chloride salts (properties in Table 2.2) in concentrated solar power (CSP) plants as thermal energy storage and heat transfer fluid materials due to their high thermal stability limits (>800°C) and low prices, compared to the commercial nitrate salt mixtures (decomposition at ~550°C) reported in Table 2.1.

As it is possible to notice, all the salts reported in Table 2.2 not only have a high stability limit, which will allow increasing efficiency of energy conversion using sCO_2 Brayton cycles, but they also have a high freezing point, meaning that they can only be successfully employed in plant configuration in which the working fluid enters the primary heat exchanger at already high temperature, condition found in recuperative gas cycles.

However, the higher operating temperature of TES/HTF materials causes additional challenges, particularly increased corrosiveness of metallic alloys used as containers and structural materials. This significantly limits the lifetime of the structural materials and increases the levelized cost of electricity (LCOE).[52]

Name	Composition (wt%)	Melting point (°C)	Stability limit (°C)	Viscosity (Pa s)	Thermal conductivity (Wm^{-1}K^{-1})	Heat capacity (kJ kg^{-1}K^{-1})	cost ($ kg^{-1})	Source
Solar Salt	$NaNO_3$ (60) - KNO_3 (40)	220	600	0.00326 (at 300°C)	0.55 (at 400°C)	1.1 (at 600 °C)	0.5	[49]
Hitec	$NaNO_3$ (7) - KNO_3 (53) - $NaNO_2$ (40)	142	535	0.00316 (at 300°)	~0.2 (at 300°C)	1.56 (at 300°C)	0.93	[49]
Hitec XL	$NaNO_3$ (7) - KNO_3 (45) - $Ca(NO_3)_2$ (48)	120	500	0.00637 (at 300°C)	0.52 (at 300°C)	1.45 (at 300 °C)	1.1	[49]
Na–K-Li nitrates	$NaNO_3$ (28) – KNO_3 (52) - $LiNO_3$ (20)	130	600	0.03 (at 300°C)	N/A	1.091	~1.1	[49]
K-Li-Ca nitrates	KNO_3 (50-80)- $LiNO_3$ (0-25) - $Ca(NO_3)_2$ (10-45)	<80	~500	~0.004 (at 190°C)	0.43 (at 300°C)	N/A	0.6-0.8	[49]
Na-K-Li nitrates/nitrites	$NaNO_3$ (14.2) - KNO_3 (50.5) - $LiNO_3$ (17.5) - $NaNO_2$ (17.8)	99	430	N/A	N/A	1.66 (at 500°C)	N/A	[49]
Sandia Mix	$NaNO_3$ (9-18) - KNO_3 (40-52) - $LiNO_3$ (13-21) - $Ca(NO_3)_2$ (20-27)	<95	500	0.005-0.007 (at 300°C)	0.654 (at 250°C)	1.16-1.44 (at 247°C)	0.62-0.81	[49]

Table 2.1 Low temperature molten salts properties[49]

Name	Composition (wt%)	Melting point (°C)	Stability limit (°C)	Viscosity (Pa s)	Thermal conductivity (Wm^{-1}K^{-1})	Heat capacity (kJ kg^{-1}K^{-1})	cost ($ kg^{-1})	Source
Li-Na-K carbonates	Li_2CO_3 (32.1)- Na_2CO_3 (33.4) - K_2CO_3 (34.5)	397	>650	0.0043 (at 800°C)	N/A	~1.4-1.5 (at 400°C)	1.3-2.5	[49]
Li-Na-K fluorides	KF (59)- LiF (29) – NaF (12)	454	>700	N/A	1.17(at (400°C)	1.9 (at 700°C)	>2	[52]
Na-K-Zn chlorides	NaCl (7.5)-KCl(23.9)-$ZnCl_2$ (68.6)	204	850	0.004 (at 600-800°C)	0.325 (at 300°C)	0.81 (at 300-600°C)	<1	[52]
Mg-Na-K chlorides	NaCl (14)-KCl(17.8)-$MgCl_2$ (68.2)	380	>800	N/A	N/A	~1 (at 500-800°C)	0.5	[52]
Mg – K chlorides	KCl (67) - $MgCl_2$ (33)	426	>800	0.0018 (at 600°C)	0.39	1.15137	0.35	[12]

Table 2.2 High temperature molten salts properties

2.3.2.5 Liquid metals

At the beginning of the second half of the 20th century liquid metals thermo-physical properties were totally unknown. The research regarding their properties began in the period going from 1950 to 1970 because of the need of nuclear power engineering for the development of fast cooling reactors. Several experimental tests that took place in this period of time lead to the development of proper thermophysical tables. However until then the only liquid metals that have had operational experience in nuclear systems as coolants have been sodium and lead-bismuth. [40]

In the whole literature there are three main categories of liquid metals which are taken in consideration for the application as heat transfer fluids: Alkali metals, Heavy metals and Fusible metals. Main HTF characteristics belonging to these groups are summarized in Table 2.3. As reported from Lorenzin and Abánades in [40] data regarding thermophysical properties of liquid metals in the literature is not exhaustive therefore some information might be uncertain.

Name	Melting point (°C)	Stability limit (°C)	Viscosity (Pa s)	Density (kg/m³)	Thermal conductivity (W/mK)	Heat capacity (kJ/kgK)	cost ($/kg)
Molten Tin (Sn) (at 600°C)	232	2687	0.00101	6330	33.8	0.24	15.9
Gallium (Ga) (at 700°C)	29.8	2403	0.00069	5637	59.5	3.75	252
Sodium (Na) (at 800°C)	98	883	0.0016	761	57.6	1.26	2
Lithium (Li) (at 1000°C)	180	1347	0.0002	436	63.3	4.16	11.82
Lead-bismuth (44.5 Pb-55.5 Bi wt%) (at 800°C)	125	1638	0.00133	9710	17.7	1.46	13
Galinstan (66 Ga − 20.5 In −13.55 Sn wt%) (at 20°C)	-19	>1300	0.0024	6440	16.5	0.29	450

Table 2.3 Liquid metals properties (The data regarding Galinstan is taken at room temperature (20 °C) since for the moment its flow has been studied only within micro-devices and too much variation has been found for its price).

As it can be assessed assess from the reported properties, liquid metals and their alloys don't have the problematic upper and lower operating temperature limitations of molten salt, they can have solidification temperatures below 0 ∘C and boiling temperatures above 1600 ∘C. Freezing of the HTF inside pipes, the receiver, valves and TESS can, therefore, practically be eliminated and energy consumption for heat tracing is lowered. At the same time, the HTF can operate at low pressures and still reach the temperatures required for a next-generation Rankine or a Brayton power cycle.[51]

Another advantage is the large thermal conductivity which implies wider heat transfer coefficients for elementary geometries (more than two orders of magnitude higher than molten salts) hence higher allowable heat fluxes.[40] Recent studies as [12] show that the improved heat transfer allows to design smaller receivers with respect to molten salt receivers, given the same thermal power output, due to higher allowable heat fluxes, and this reduction of heat exchanging area leads to improved receiver thermal efficiency, reduced temperature difference across tube walls thus lower stresses.

On the other hand, their relatively low cp discourages the use of direct TES concepts and indirect solutions are required. Lastly operational aspects and safety risk management must be taken into account.

Eventually, the decision shall be based on a detailed analysis of pros and cons. The relative importance of these is influenced by the level of maturity of the technology. Indeed, in the context of corrosion, operational and safety aspect, experience is a key factor. With their long history in the nuclear industry since the 1940s, liquid sodium and lead bismuth eutectic (LBE) are the most studied as HTF. In particular, liquid sodium has also been proposed and tested for solar applications since the early days of CRSs. [38] In 1968, the US Atomic Energy Commission compiled the extensive Sodium-NaK Engineering Handbook [5]. With around 50 contributors, the handbook brought together experiences from many sodium-cooled reactors and sodium test facilities world- wide.

Sodium has a lower melting point of 97.7 °C and a high boiling point of 873 °C, giving it a large operating temperature range. Its advantage over other liquid metals as working fluids is mainly it's low price and the knowledge which comes from nuclear experimentation.[3]

Liquid sodium was used as both HTF and storage medium in the SSPS project of the International Energy Agency, which started operating a 500 kWe tower system in 1981 in Almeria, Spain. The thermal performance of the high-intensity receiver was most satisfactory with peak heat fluxes over 2.5 MWm^{-2}. The overall operation was however not successful because of lack in suitable monitoring, handling and technological standard at that time, which resulted in a sodium fire.[38]

Indeed, the disadvantage of sodium is its high reactivity when in contact with water. Even if no air is present, a rapid and violent reaction will occur between sodium and water, with both hydrogen and steam evolving. If air is present, an explosive mixture will be generated as the hydrogen mixes with the air, when in contact with dry air, sodium burns releasing a high aerosol [3] However, this risk can be controlled, experience show how sodium fires can be safely and quickly extinguished with Soda Ash [53].

In Coventry et al. [54] safety risks of sodium receiver are analysed starting from Sodium-NaK Engineering Handbook and many safety measures which must be taken working with sodium are indicated. This study concludes that sodium is a hazardous substance, and that in developing CSP installations with sodium as the HTF, high standards of safety design and operator training are necessary. Although it is noted that security measures needed in a sodium HTF loop in a CSP plant are not very different from those found in other well-accepted industrial plants involving hazardous materials, such as a petrochemical refinery.

2.3.3 Conclusions

Taking in consideration the information summarized above it is clear that conventional fluids are not able to further improve CSP systems efficiency but that the industry needs to look towards higher stability limits fluids in order to have a consistent improvement of the overall

efficiency. For this reason the only HTFs which could be competitive are liquid metals and the new mixtures of molten salts which extend the temperature range up to 900 °C.

The evident disadvantages of using liquid sodium is that it is up to 200% more expensive per kilogram and that it must be completely isolated from the environment. Furthermore, its low volumetric specific heat capacity results in higher storage volumes, although this is reduced if sodium's higher temperature possibilities are utilised increasing temperature difference. If these limitations can be overcome, however, Boearema et al. [3] showed that there are several advantages in using sodium as heat transfer fluid. First, with a heat transfer coefficient that is an order of magnitude greater and a thermal conductivity that is two orders of magnitude greater than that for Hitec, liquid sodium will reduce the risk of hot spots and thus reduce pipe stresses. This can also mean much lower velocity for the same level of heat transfer. Lastly and more importantly, a better heat transfer allows reducing heat transfer areas in sodium receivers for the same power exchanged, with respect to molten salt ones, which implies higher thermal efficiencies at similar surface temperatures.

Polimeni et al. [4], which compared a liquid sodium receiver with a $KCl-MgCl_2$ one, both coupled with various sCO_2 cycles, proved that, with sodium, a higher efficiency receiver can be designed, with lower pressure drops and a smaller surface area exposed. Indeed a sodium receiver coupled with a recompressed intercooled sCO_2 Brayton cycle can achieve solar to electric efficiencies more than 3% higher than conventional solar salts coupled with a steam Rankine cycle and about 1.1% higher than innovative $KCl-MqCl_2$ salts coupled with the same sCO_2 cycle.

Moreover the HTF and storage costs (in case of direct thermal storage) are only an initial cost in case of liquid metals while in the case of molten salts used at high temperature these are O&M costs since molten salts need to be reintegrated continuously because of thermal degradation [40].

For all of these reasons sodium has been chosen for this study, although further technical studies should focus on whether the benefits of using sodium as HTF overcomes the safety risks and to verify its convenience in terms of LCOE.

2.4 Thermal energy storage system

Between different renewable energy options concentrating solar power (CSP) is of particular interest due to the applicability of a thermal energy storage (TES) system.

In CSP plants, TES serves multiple purposes. It balances the plant in transient periods, for example, during overcast, it enables stable turbine conditions and more full-load hours. The most important reason for the implementation of a large TES is, however, to be able to supply dispatchable or base-load power to the grid and even stabilize it on demand. This is also an economical advantage because CSP plant is able to supply energy at times of greatest need

which generally have the highest electricity tariff. Lastly TES increases the capacity factor of the power block and minimizes defocusing of mirrors [51][42].

The three types of TES systems, being developed today, store energy either as: sensible heat, latent heat from material phase change, a combination between these two (combined sensible-latent and thermochemical storage systems) or thermochemical heat, using the heat released (or absorbed) during chemical reactions occurring inside the material. [55] In this analysis the author chose a simple direct two tank sensible heat storage system and thermal losses inside the tanks have been neglected.

This approximation has been made for sake of simplicity, although it is an assumption which is usually made when designing a CSP system since tanks and pipes are insulated and traced with electrical resistances. The tracing system is not usually required if the stored fluid is used during the night because the heat loss in such a short time is minimal, it is instead used in case of long stops which are needed for maintenance. Moreover the decrease of temperature due to heat loss in the storage tanks and pipes can be partially compensated by the temperature increase due to irreversibility in the sodium pump, which is also neglected.

Figure 2.9 presents the schematic diagram of the two-tank molten salt storage system. The cold HTF is heated up from the solar field and flows directly in the thermal storage unit. When it is needed, part of the storage fluid (which in the direct case is also the HTF) is pumped through the heat exchanger of the power block.
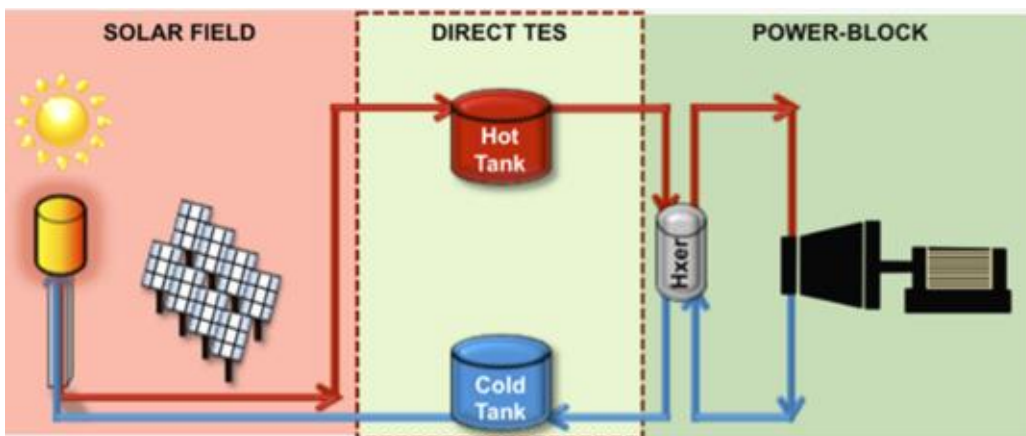
Figure 2.9 Direct thermal storage system integrated in the CSP plant with solar field and power block [42]

This TES system ensures the lowest ΔT between sodium and working fluid temperatures since there is no intermediate storage fluid, which would employ two heat transfers steps. The use of a thermocline could reduce investment costs, since only one tank (with the same volume of one tank of a two storage tank system) is necessary, although inside the thermocline heat is exchanged from the hot to the cold fluid, especially if the HTF is sodium which has a high thermal conductivity, therefore part of the heat accumulated is wasted. Besides the use of sCO_2

as working fluid in the power cycle matches well with sensible heat storage due to its single-phase operation (see Figure 2.10).
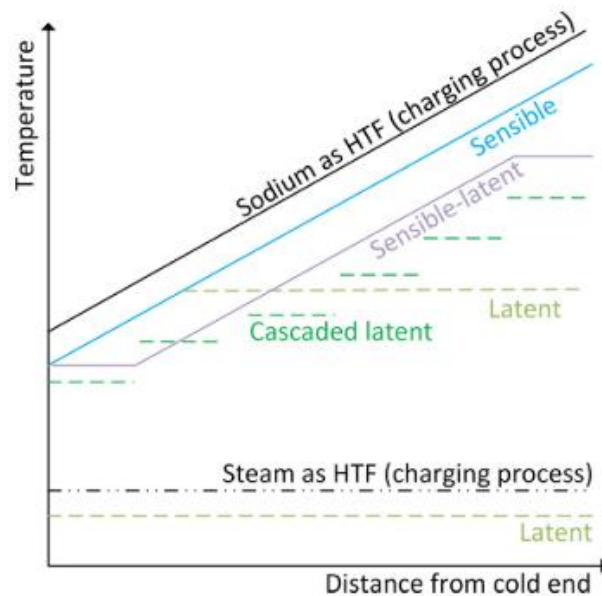
Figure 2.10 Schematic profiles of the HTF and sensible and latent storage option during the charging process [56]

Although this configuration has many drawbacks: mainly the high cost of sodium and its low heat capacity imply a very high cost of the storage. Moreover, there are several safety concerns in keeping a large quantity of sodium in a tank due to its high flammability and reactivity with water and humid air. This problem could be overcome with the use of several smaller tanks instead of a big one, but this solution would further increase the cost of the TES system.

The choice of this type of TES has been drawn by the maturity level of this technology, indeed the current state-of-the-art TES technology is the two-tank sensible energy storage using a molten salt [42] and this is the most commonly used storage technique in utility-scale CSP plants, moreover this type of TESS was also tested with Sodium as HTF and storage material in the IEA-SSPS project in Almeria in the 1980s.[56]

2.5 Electricity generation system

2.5.1 Working fluid

All the SPTs currently in operation are based on conventional Rankine steam cycles for the conversion of the thermal power [11]. Although, supercritical carbon dioxide (sCO_2) cycles are being evaluated for many applications, including CSP, due to their many positive characteristics. It is abundant in nature, non-toxic, non-explosive, non-flammable, it shows a very good thermal stability and high chemical inertness (considerably better than that of air or steam)[28][10].

50

sCO₂ cycles were first proposed in the late 1960s by Angelino in Italy [29][28] and by Feher in the United States [57] to overcome the performance improvement limitations for steam cycles. They have been traditionally considered for application in nuclear power plants [27], but recently they have become increasingly popular also in relation to their potential application in CSP plants, due to their potentiality to substantially drive down CSP LCOE [58].

Indeed, compared to steam Rankine cycle, this type of closed Brayton cycles have smaller weight and volume turbomachinery (the turbine size can be 10 times smaller than its equivalent steam [59]), lower thermal mass and less complex power blocks due to the higher density of the fluid and simpler cycle design [11]. It has to be considered, though, that efficient sCO₂ cycles are highly regenerative, therefore they require big regenerators.

sCO₂ Brayton cycles thermal efficiency can reach 50% [36] and when source temperatures are above 550 °C they can reach higher values than that of superheated steam Rankine cycles [31].

Other positive aspects of the use of CO₂ as working fluid are the eliminated concerns over blade erosion due to droplet impingement, since there is no risk of carbon dioxide undergoing a phase change from gas to liquid as it expands through the turbine, and that heat rejection for a sCO₂ cycle is not limited by the saturation temperature of the working fluid, offering the potential for cost-effective dry cooling (i.e., the use of ambient air as the sole heat rejection medium), which is very important in arid sites as the ones in which CSP plants are usually located.

A very interesting aspect of CO₂ as working fluid is its moderate critical properties. Indeed CO₂ has a critical temperature near the ambient temperature ($T_{crit} \approx 304\,K \approx 31\,°C$) and a relatively low critical pressure ($P_{crit} = 7.37\,MPa$) which leads to acceptable operative conditions.[36][59] This peculiarity allows to exploit the beneficial real gas effect arising in the region surrounding the critical point, which is inaccessible for other common gases.

Real gas behaviour manifests through two main effects:

- **Mechanical effect**
  The reduction of specific volume, due to the low value of the compressibility factor in close-to-critical conditions. This effect is reflected on a decrease of compression work, while expansion work remains unaffected due to its distance from the critical point.
- **Thermal effect**
  The increase of specific heat of sCO2 near the critical point. This effect is particularly evident on the fluid coming out of the main compressor, this fluid is heated from the low pressure fluid in a regenerator, the difference in fluids specific heat on the two sides of the regenerator leads to large irreversibility in the heat transfer process.

In order to obtain the highest possible efficiency, full advantage must be taken of the reduction in compression work and, at the same time, the detrimental effect of the differing heat capacity between the expanded and the compressed fluid must be minimized through convenient cycle layout [28]. For this reason, sometimes, cycle simplicity is sacrificed in favour of better efficiencies, the best performances obtained from the most complex cycles.

2.5.2 sCO₂ Brayton cycles configurations

Many configurations have been studied in literature[30][34], with a particular focus on CSP applications[4][6][11]. In [29] Angelino proposes various types of sCO_2 Brayton cycle including some condensation cycles. Condensing or partially condensing cycles ensure very high efficiency because they are able to exploit the liquid behaviour of CO_2 in order to decrease as much as possible the compression work (which is entirely or partially performed with a pump). Although the condensation of CO_2, whose critical temperature is about 31 °C, requires cooling water at temperatures not higher than 12-15 °C available all year around.

In CSP sites, ambient conditions do not allow this solutions, water is scarce and ambient temperature during the day ranges around 35 °C. An air-cooling system is then necessary and the minimum temperature of the cycle does not usually reach condensation temperature.

All CO_2 gas cycle use recuperation in order to recover part of the heat left in the low-pressure gas at the end of the expansion to heat up the compressed CO_2, in these cycles recuperation is very advantageous because the temperature of the fluid at the outlet of the turbine is high, thus recuperation reduces both the primary heat exchanger and the heat rejection unit duties increasing cycle efficiency.

The present work starts from the results of Polimeni et al. [4], [12] in order to choose the most performing cycle configuration to then investigate its technical limits.

In his study Polimeni chose four types of sCO_2 cycles to analyse their performance:

- The Simple Cycle (SC)
- The Recompressed Cycle (RC)
- The Recompressed Main Compressor Intercooling cycle (RMCI)
- The Partial Cooling Cycle (PC)

a   *b*

$$c \qquad\qquad\qquad\qquad\qquad\qquad d$$
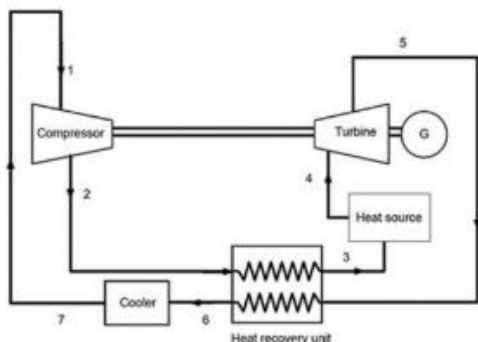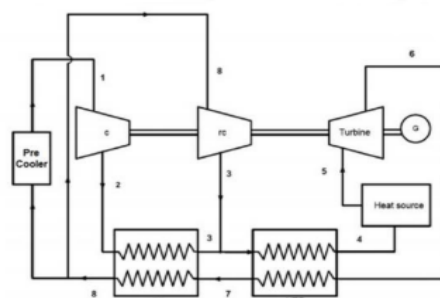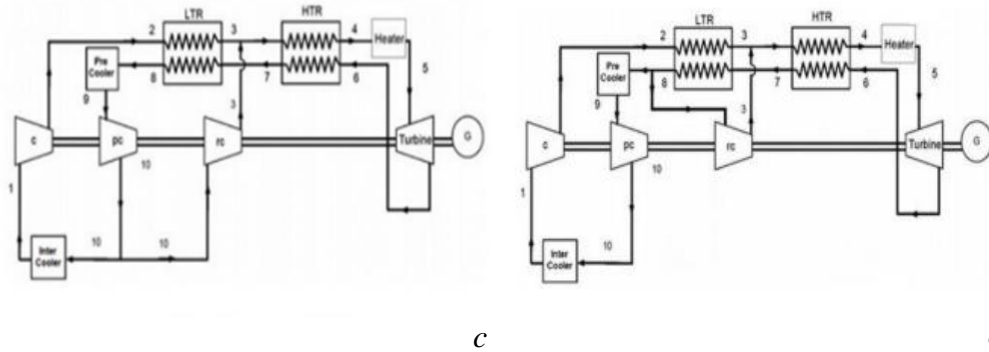
Figure 2.11 Plant configuration of a) Simple Cycle, b) Recompressed Cycle, c) Partial cooled cycle, d) Recompressed Main Compressor Intercooling cycle

The simple cycle configuration, which was first studied in 1968 by Feher [57], comprises a compressor, a turbine and three heat exchangers: a pre-cooler, a recuperator and a primary HX (Figure 2.11.*a*). It has the advantage of being very compact and it is the cheapest due to its simplicity. Although it is the least efficient one due to the real gas effects which penalizes the heat exchange in the recuperator, indeed the specific heat of the compressed fluid in the critical region (at the outlet of the compressor) is much higher with respect to the one expanded fluid which is instead far away from the critical zone, thus the average ΔT in the HX increases.

The recompression cycle configuration (Figure 2.11.*b*) is adopted to reduce the inefficiency due to irreversibility in the regenerator. Recompression reduces the efficiency loss due to irreversible heat exchange through the splitting of the fluid mass flow rate before the heat rejection unit. This ensures a lower mass flow rate of CO_2 on the cold side of the LTR, which is the one more affected by real gas effects.

A proper choice of the split ratio, defined as in Eq. 2.10 allows to balance the hot and cold fluid heat capacities and to minimize the temperature differences in the heat transfer process.

$$SR = \frac{\dot{m}_{LTRHPside}}{\dot{m}_{turbine}} \qquad\qquad Eq.\ 2.10$$

The optimal SR is the one that minimizes the overall entropy generation from the irreversible processes affected by the split ratio value.

Some studies [4] identify the split ratio that leads to an isothermal mixing of the two split flow rates as the one ensuring highest overall efficiency, its value can be obtained imposing equality to the temperature of the fluid flowing out the cold side of the LTR and the recompression outlet temperature.

A further improvement of the recompression cycle is to inter-refrigerate the main compressor reducing the work expenditure of the main compressor, that is divided in two stages (Figure 2.11.*d*). Since the average compression temperature is lower in a non inter-refrigerated

compressor, the working fluid operates closer to its critical conditions, and its specific volume is lower.

A useful parameter to identify the two compression stages is the ratio of pressure ratios RPR:

$$RPR = \frac{\dfrac{P_{high}}{P_{intermediate}} - 1}{\dfrac{P_{high}}{P_{low}} - 1}$$

The RPR parameter can be defined in order to optimize the intermediate pressure to obtain the minimum compression work possible.

A direct effect of the intercooling system, besides the higher useful work, is a lower temperature of the fluid coming out from the HTR, that means also, for fixed TIT, a larger temperature change of the HTF, that improves the receiver thermal efficiency [12] and reduces storage size.

The last configuration studied in the work of Polimeni et al. [4] is the Partial cooling cycle, also called recompression cycle with precooling. This cycle was designed firstly by Angelino [28] in order to decouple the turbine outlet pressure from the compressor inlet one, therefore there is more margin for optimization.

Results of the work of Polimeni et al. [4] significant for the choice of the cycle configuration are reported in Table 2.4.

$\eta_{overall}$	Ref	KCl-MgCl$_2$				Sodium			
	Steam	SC	RR	PC	RMCI	SC	RR	PC	RMCI
Design case	21.44%	21.34%	21.99%	23.69%	23.92%	22.17%	23.13%	24.69%	25.01%
Annual simulation in Seville (Spain)	18.46%	-	17.29%	18.52%	18.68%	-	18.91%	20.23%	20.45%
Annual simulation in Las Vegas (USA)	17.42%	-	16.58%	17.82%	17.97%	-	17.80%	19.03%	19.25%

Table 2.4 Polimeni et al. [4] *overall efficiency of the plant for the different configurations analysed*

From the cited study the highest possible efficiency in design conditions, with sodium as a heat transfer fluid, are achieved by the RMCI cycle followed by the partial cooling cycle. Efficiency of the RMCI is consistently higher than the result achieved by a conventional solar salt coupled with a steam Rankine cycle due to the combined positive effects of the innovative working fluid, which can reach higher temperatures, and the innovative sCO$_2$ cycle, with higher thermal efficiencies.

Regarding the annual analysis the cycles which scores the best results is still the RMCI followed by the partial cooling cycle, even if in this case the difference in overall efficiency with respect to the conventional configuration is less than 2 %, lower than the 3.5 percentage point earned in the design case.

From this analysis appears, as Angelino predicted in [28], that the most complex cycles are the most performing ones. Even if a techno-economic analysis might result in advising a different best configuration, the RMCI cycle was chosen in this study in order to investigate all the possible technical limits of the most complex cycle.

3 Models of the plant subsystems

In this section a detailed description of the models used to simulate performance of the power block, receiver and solar field is presented. The accuracy of these models is important to reproduce physical behaviour of the analysed subsystems.

All the models consider steady state and nominal conditions. The design starts from the power block where the electric power output is fixed at 30 MW (gross power output, only considering auxiliaries of the heat rejection unit), value which is similar to medium sized CSP plant. Receiver and solar field layouts are designed to ensure the PB required thermal power considering that a thermal energy storage is present, therefore receiver and consequently solar field power duties are multiplied by a solar multiple.

Some of the power block model outputs, such as thermal power input and sodium temperatures, are then part of the inputs of the receiver model. Receiver and solar field models are linked by a two ways dependency, therefore the procedure to match the solar field and the receiver designs is iterative (as shown in Figure 3.1).
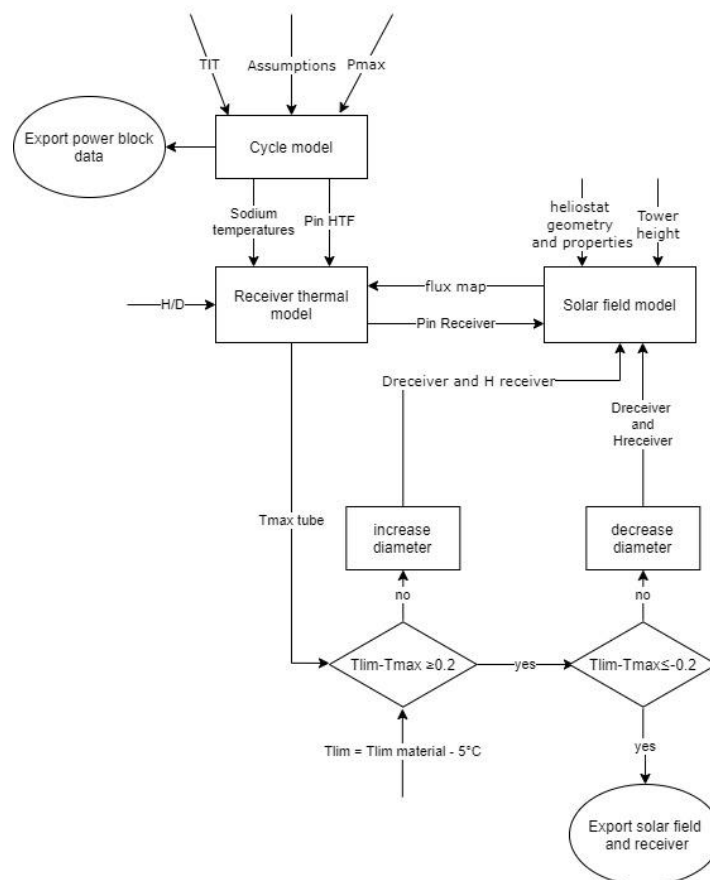
Figure 3.1 Flow diagram showing how the different models interact

3.1 Power block model

The present analysis started from the reconstruction of the RMCI sCO_2 thermodynamic cycle with the assumptions made by Polimeni et al. [4] in the Excel software, calculating fluid properties with the REFPROP add in for Excel starting from the pressures in each thermodynamic point, which are known once the pressure drops have been set, and a second property calculated through a cycle balance.

The results were subsequently compared with the ones of Polimeni et al. [4]. Then a further optimization of the cycle efficiency has been performed varying the turbine pressure ratio (consequently the minimum pressure of the cycle, being the maximum pressure fixed) and the Recompression Pressure Ratio (RPR); this analysis is reported in section 4.2.2.

In the RMCI cycle the sCO_2 exits from the turbine at a high temperature and goes directly in a High Temperature regenerator (HTR) and subsequently in the Low Temperature regenerator (LTR). After the LTR the hot fluid is split in two parts, one is furtherly cooled down to the entrance of the main intercooled compressor while the other is directly compressed up to the entrance conditions of the cold fluid in the HTR. The fluid is split in order to enhance the heat exchange in the LTR, indeed the capacity of the fluid on the cold side of the regenerator is much higher than the one on the hot side since the first is very close to the critical point.

The flow which is compressed in the main intercooled compressor is heated primarily in the LTR before being mixed with the fluid coming from the intermediate compressor. The fraction of fluid which is recompressed is chosen in order to minimize the inefficiency given by the mixing of the two fluids before the HTR. This choice was made on the basis of a previous analysis made by Polimeni [12] which optimized the SR.

Initially the assumptions reported in the second column of Table 3.1 were considered, subsequently a deeper study of pressure losses, aimed at verifying consistency of pressure loss assumptions made by Polimeni in [4] with the pressure drop model found in his thesis [12], was performed. The model used to describe the heat exchangers heat transfer and pressure losses, which comes originally from the thesis of Dostal [27], considers printed circuit heat exchangers and it is reported in Appendix A.

This analysis resulted in new assumptions for the cold sides pressure losses, this study will be presented in section 4.2.3.

Assumptions	From Polimeni et al. [22]	This work
Turbine inlet pressure [bar]	250	250
CO_2 minimum temperature [°C]	52	52
ΔT_{min} LT/HT regenerator [°C]	12	12
Turbine isentropic efficiency	0.93	0.93
Compressor isentropic efficiency	0.85	0.85

Mechanical/Electrical efficiency	0.99/0.99	0.99/0.99
Δp/p HP side of LT regenerator (Cold side)	0.1	0.0006*
Δp/p LP side of LT regenerator (Hot side)	0.015	0.015
Δp/p HP side of HT regenerator (Cold side)	0.1	0.0016*
Δp/p LP side of HT regenerator (Hot side)	0.015	0.015
Δp/p PHX (CO_2 side)	0.015	0.015
Δp/p precooler	0.02	0.02

*Table 3.1 Assumptions made by Polimeni et al. [4] and assumptions considered in this work *computed values in paragraph 90*

A simplified model of the heat exchangers was implemented in Exel, this model discretizes the temperature step over the HX since specific heat of the fluid changes with temperature due to real gas effects. The aim was to control the temperature difference in each segment of the HXs, the minimum temperature difference on the HTR is always on the cold end while the one on the LTR can vary between the cold end and the hot end depending on the split ratio. If the minimum ΔT on the HT regenerator is imposed also the hot end of the LT regenerator isn't a free parameter if isothermal mixing at the outlet of the LTR is assumed, therefore the ΔT of cold end of the LT regenerator is also imposed to be 12 °C in order to have an additional constraint which is needed to characterize all the thermodynamics points of the cycle.
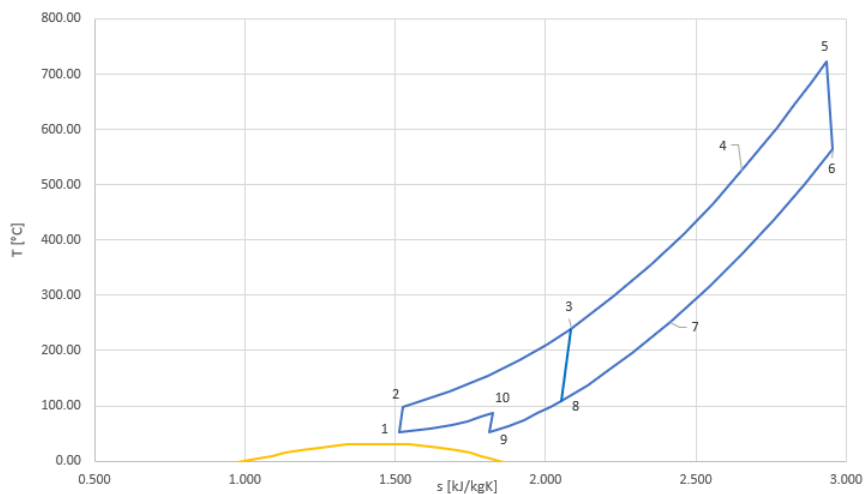
Figure 3.2 T-s diagram of the power cycle [12]

Once these assumptions were made the evaluation of thermodynamic cycle points started from the already characterized ones, which were:

- The turbine inlet (5), thermodynamic properties are calculated starting from pressure and temperature which is previously defined, the preliminary study has been conducted in the range [723.6; 785] °C.

- The main compressor inlet (9), thermodynamic properties are calculated starting from pressure and temperature which is assumed to be 52°C, this is a reasonable value in CSP locations where ambient temperature ranges around 35°C and an air cooling is necessary due to arid conditions.

It is possible to calculate the thermodynamic properties of the isentropic outlet of the turbine (6s) from the entropy value, which is equal to the entropy at the inlet of the turbine since the expansion is isentropic, and the pressure, given by the expansion ratio previously defined. Once the enthalpy of point 6s is specified point 6 properties can be derived from enthalpy calculated with the isentropic efficiency definition.

An initial value of RPR is guessed which is useful to calculate the thermodynamic properties of point 10 and 1. Point 1 is defined by pressure (Pmedium) and temperature (52°C), while point 10 is evaluated similarly to point 6 with the compressor isentropic efficiency definition. The same procedure is, then, used to evaluate point 2 starting from point 1.

Temperature in point 8 is defined from the ΔT of cold end of the LT regenerator. This point is the inlet of the intermediate compressor and therefore with the same calculations made previously for compressors we can obtain the properties of point 3 (outlet of the compressor) which coincides with the outlet of the LT regenerator due to the necessity to minimize the mixing inefficiency.

The SR, defined as in Eq. 3.1, correspondent to the non-mixing condition results from the enthalpy balance on the LT regenerator.

$$\alpha = \dot{m}_{cold\ side}/\dot{m}_{tot}$$ *Eq. 3.1*

Point 7 is characterized knowing the ΔT of cold end of the HT regenerator, while point 4 results from the enthalpy balance on the HX. Mass flow rates on the two sides of HT regenerator are the same because the heat capacities are pretty similar since this HX works in conditions far from the critical point.

Lastly from power production of the turbine has been subtracted the mechanical power consumption of the compressors and the electrical power consumed from the air condenser.

This auxiliary consumption has been calculated assuming a 15°C temperature variation of the cooling air hence obtaining the necessary mass flow rate to cool down the sCO_2 to 52°C. Knowing heat rejected, mass flow rate of air and the temperatures of air and CO_2 it is possible to calculate the UA of the heat exchanger.

Datasheet		
Power consumption	86	kW
Q rejected	4400	kW
Mass flow rate	459.02	kg/s

T min air	293.15	K
T max air	302.55	K
T min CO_2	304.55	K
T max CO_2	323.05	K
ΔT_{lm}	15.51	K
UA	283.73	kW/K

Table 3.2 Air cooler datasheet

Starting from data on the consumption of a real CO_2 air cooler found in an offer datasheet provided by ESE (Table 3.2) the power consumption has been adapted to each problem rescaling the consumed power from the reference air cooler considering the changed mass flow rate of air needed. This value can be calculated from the heat rejected and the air temperatures.

$$P_{extimated} = \left(\frac{\dot{m}_{air}}{\dot{m}_{air_{datasheet}}} \right) * P_{datasheet} \qquad \qquad Eq.\ 3.2$$

3.2 Receiver thermal model

The thermal model of the receiver has been developed starting from a solar salt receiver model made by ESE company in order to evaluate, given a required temperature change, a required heat input in the HTF and receiver geometry, the mass flow rate of the HTF and the thermal efficiency, through the estimation of reflective, radiative and convective losses.

The model takes in input the heat required by the power block which, multiplied by the solar multiple, is the power the receiver has to provide to the HTF and the inlet and outlet sodium temperature which are calculated from sCO_2 temperatures assuming a constant ΔT of heat exchange on primary heat exchanger of 15°C. In this work a solar multiple equal to three has been chosen, so that, coupled with a large thermal storage, it ensures an almost continuous operation of the power block. A continuous operation is favourable for many reasons: first to avoid less efficient part load operation of the power block, to avoid cyclic thermal strains to components such has heat exchangers and turbomachines and lastly because CSP can provide constant renewable power throughout the whole day without fluctuations. In a 100% renewables scenario CSP is expected to also cover peaks of the electricity demand, therefore working often in off-design, although this scenario doesn't seem to be imminent.

Other assumptions are the ambient conditions and the optical properties of the coating, reported in Table 3.3. The location of Ivanpah Solar Power facility (35.57°N 115.47°W) was chosen as reference, this site is located at an elevation of 1070 m therefore air pressure is lower than 1 atmosphere. Reference air temperature is so high since design conditions are the summer solstice ones, when the temperature is high.

Property	Value	Unit
Air Velocity	5	m/s
Air Temperature	35	°C
Air Pressure	998.5	mbar
Absorptance	93	%
Emissivity	87	%

Table 3.3 Reference ambient conditions and optical properties of the coating [60]

The model is adapted for a Sodium receiver introducing a module which calculates the sodium properties starting from correlations found in literature [13],[61] and reported in Appendix D, Table 11.1.

The existing solar salt model was also modified changing the internal convection correlations used for molten salts (Gnielinski correlation) with the Sleicher – Rouse correlation suggested by Benoit et al. in [13] and by Boerema et al. in [3] for sodium.

A simplified flow diagram of the processes is shown in Figure 3.3.

The model requires as inputs:

- the geometry of the receiver (height H and diameter D)
- the geometry of the tubes (thickness t and diameter d_{ext})
- the panel arrangement (number of parallel flow paths NFP, number of passes per path NP, number of parallel panels per path NPP, from which the model calculates the total number of panels and the number of tubes per panel)
- the inlet and the outlet temperature of the HTF
- the net power sent to the power block (after thermal losses)
- the ambient conditions (ambient temperature and wind speed)
- the map of the flux incident on the external surface, in this preliminary analysis the flux map is obtained multiplying the required average DNI in order to have a certain power input in the HTF (given by the model which accounts for the thermal efficiency of the receiver) with a coefficient map obtained by crossing two gaussian distributions on the two axes.
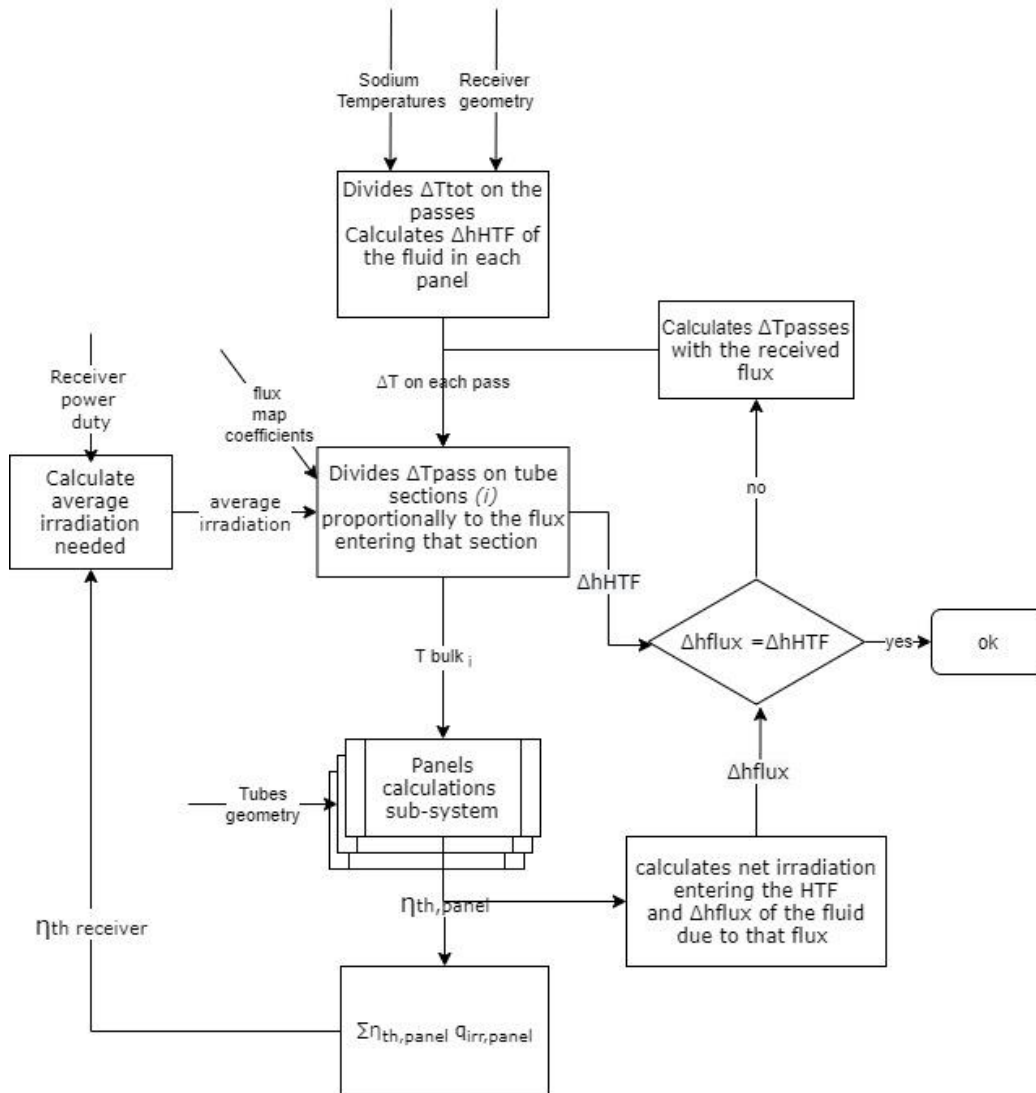
Figure 3.3 Receiver thermal model flow diagram

A preliminary thermal balance is performed dividing the total temperature difference of the HTF on the receiver by the number of passes and obtaining inlet and outlet temperatures of each pass, hence calculating the heat input required on each pass in order to reach the outlet temperature.

$$Q_{required} = \frac{\dot{m_{HTF}}}{2} * \left(h(Tout_{pass}) - h(Tin_{pass}) \right)$$

Eq. 3.3

These first guess temperatures will then be iteratively updated in order to match the heat input required with the solar heat input on the single pass, accounting also for heat losses.

$$Q_{provided} = q_{irr\,avg_{pass}} * \eta_{th_{pass}} * A_{pass}$$

In order to calculate losses each pass and the corresponding flux map is discretized in equal surface area segments, the number of discretization steps is one of the inputs (n_{segm}). The irradiation of the sun on each segment is different, due to the uneven flux map, therefore the temperature raise in a panel is not equally distributed on each segment.
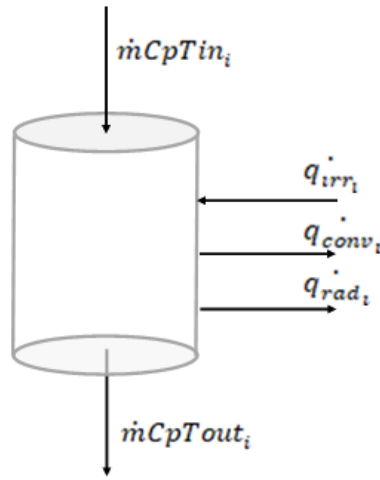
Figure 3.4 Control volume heat balance

The temperature of the fluid exiting the segment *i* is calculated as follows:

$$Tout_i = Tin_i + \frac{\Delta T_{tot,pan}}{\sum_i^{n_{segm}} q_{irr_i}} * q_{irr_i} \; [°C]$$

Where Tin_i and $Tout_i$ are the inlet and outlet bulk temperatures of the HTF passing through segment *i*, $\Delta T_{tot,pan}$ is the total temperature step of the fluid across the whole length of the pass and q_{irr_i} is the irradiation incident on the segment of pass, therefore the sum is the total irradiation on the pass.

In this way the bulk temperature distribution on the longitudinal axis of the tube can be obtained, this is the starting point to calculate convective and radiative losses, conduction losses to the tower structures are, instead, neglected.

To understand the heal losses mechanism it is useful to visualize it through a thermal network. From circuit theory, resistance across an element is defined as the ratio of electric potential difference ΔV across that element, to electric current *I* traveling through that element, according to Ohm's law reported in Eq. 3.6.

$$I = \frac{\Delta V}{R}$$

Within the context of heat transfer, the respective analogues of electric potential and current are temperature difference ΔT and heat rate q, respectively. Thus thermal circuits can be established similarly calculating thermal resistances R as in Eq. 3.7. In this study the thermal network built is specific to the surface area of each segment.

$$R' = \frac{\Delta T}{q}$$
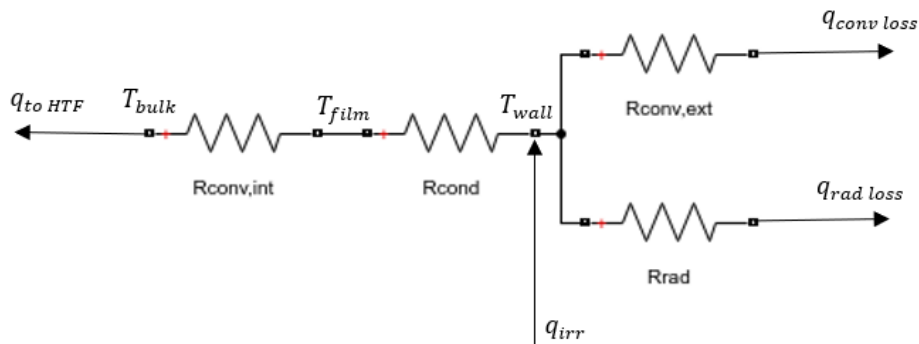
Figure 3.5 Equivalent resistance network

In this thermal network some resistances were neglected: the one due fouling on the internal and external wall of the receiver and the conduction resistance of the film coating, being it a very thin layer.

3.2.1 Internal convection calculation

When considering the internal convection inside the sodium receiver tubes the hydrodynamic entrance region of the tubes is neglected, in order to be able to use fully developed flow correlations. Inside the tube, temperature varies radially from the bulk temperature, in the area which is farther from the heat source, to the film temperature which is the temperature of the sodium in contact with the wall and, if the fouling resistance is neglected, also the temperature of the internal wall of the tube.

In order to calculate the film temperature starting from the bulk one an iterative procedure is needed because properties of sodium, which are used in the calculation, depend on the mean temperature of the fluid. Therefore the "iterative calculation" option in excel is used.

Guessed a film temperature it is possible to calculate the mean temperature (the bulk temperature is known from previous calculations, Eq. 3.5), hence thermal conductivity, specific heat and viscosity of sodium at that temperature.

The correlation used to calculate the Nusselt number is the Sleicher, C.A. & Rouse, M.W. correlation, specific for internal turbulent flow of sodium [3], [13].

$$Nu = \frac{h\,Din}{k} = 6.3 + 0.0167\,Re^{0.85}Pr^{0.93} \qquad \text{\textit{Eq. 3.8}}$$

Hence:

$$h = \frac{Nu\,k}{Din} \quad \left[\frac{W}{m^2K}\right] \qquad \text{\textit{Eq. 3.9}}$$

The film temperature can then be calculated has:

$$T_{film} = T_{bulk} + \Delta T_{int\ conv} = T_{bulk} + \frac{q}{h} \qquad \text{\textit{Eq. 3.10}}$$

Where q is the specific heat flux on the surface of the control volume $\left[\frac{W}{m^2}\right]$.

The process is then repeated until the assumed T_{film} and the calculated T_{film} coincide.

3.2.2 Conduction in the tube wall

To determine the outer temperature of the tube walls another iterative procedure is required, indeed the metal conductivity, needed to assess the equivalent conductive thermal resistance, depends from the mean temperature in the tube wall.

To begin with it's important to focus on some aspect regarding the thermal network resistance. In problems in which the equivalent resistance of the hollow cylinder (Eq. 3.11) is used, the heat flux incoming or exiting the tube is uniform on its whole cylindrical surface. In this case it is possible to consider a single heat source or sink and a single resistance for the whole cylinder lateral wall (see Figure 3.6).

$$R_{hollow\ cylinder} = \frac{\ln\dfrac{R_{ext}}{R_{int}}}{2\,\pi\,k\,\Delta l} \quad \left[\frac{K}{W}\right] \qquad \text{\textit{Eq. 3.11}}$$
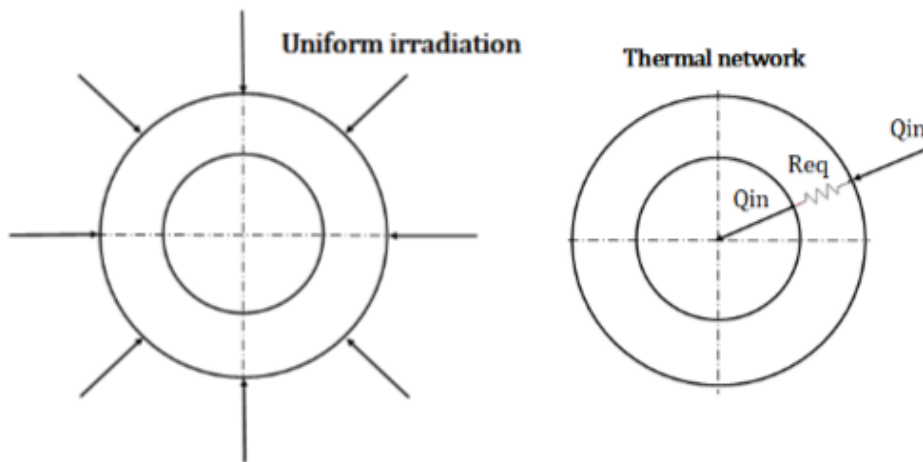
Figure 3.6 Thermal network in case of uniform irradiation

In the case of interest, although, irradiation is distributed only on one side while the back of the tubes is insulated (heat flux is approximated to be zero), therefore the single resistance of the tube walls must be divided in two parallel ones as in Figure 3.7.
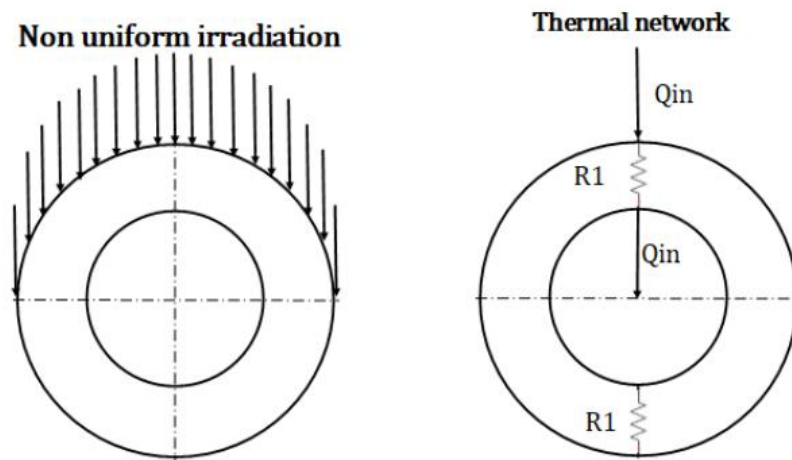
Figure 3.7 Thermal network in case of non-uniform irradiation

The resistances in this case can be obtained from the parallel resistances' formula:

$$Req^{-1} = \left[\frac{1}{R1} + \frac{1}{R1}\right]^{-1} \qquad \text{Eq. 3.12}$$

Hence,

$$R_1 = 2Req = \frac{\ln\dfrac{R_{ext}}{R_{int}}}{\pi \, k \, \Delta l}$$

The flux map gives a value of irradiation referred to the normal area of the tube, as it can be seen in Figure 3.8.
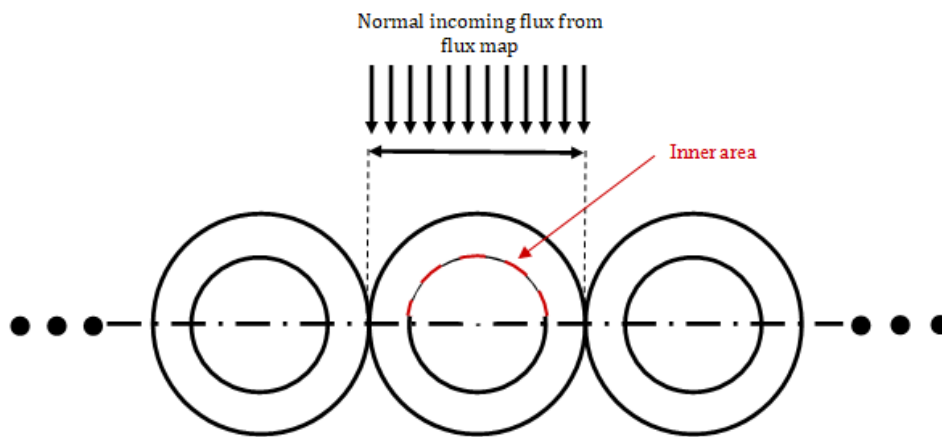
Figure 3.8 Representation of the normal flux to the receiver tubes

Radiation on the tube surface is directed in the normal direction to the receiver, thus the radiation incident angle on the tube surface varies between 90° and 0° at the tube lateral sides, for this reason temperature on the irradiated side of the tube will not be uniform. The normal flux value given by the flux map is rescaled on the area of the inner tube wall semicircle in order to calculate the mean external temperature, which is useful to evaluate the convection and radiative losses. The maximum wall temperature, which is expected to be on the portion of the tube where the irradiation is perpendicular, is calculated with the normal flux.

The flux referred to the inner area ($q_{inner\ area}$) is calculated as:

$$q_{inner\ area} = q_{normal} * \frac{A_{normal}}{A_{inner}} = q_{normal} * \frac{d_{ext} * \Delta l}{\dfrac{\pi}{2} d_{int} * \Delta l} = \frac{q_{normal}}{\dfrac{\pi}{2}\dfrac{d_{int}}{d_{ext}}} \quad \left[\frac{W}{m^2}\right]$$

The mean external temperature is calculated through the aid of the equivalent thermal network and, since the specific flux is referred to the inner area, also the equivalent resistance must be specified on the same area (Eq. 3.15).

$$R'_{cond} = \frac{\ln \frac{R_{ext}}{R_{int}}}{\pi \, k \, \Delta l} * \frac{\pi}{2} * d_{int} * \Delta l \quad \left[m^2 K \Big/ W \right]$$

The mean external temperature results from the following equation:

$$T_{wall \, ext} = T_{film} + q_{inner \, area} \, R'_{cond} \; [°C]$$

The computed value, then, substitutes the initial guess in the calculation of the average tube wall temperature, value which is used at the beginning of the iterative process in the assessment of the thermal conductivity of the tube metallic material.

It is also important to compute the maximum wall temperature, since it needs to be compared with the material limits. The maximum temperature is calculated using the Eq. 3.16, substituting the normal flux in place of the flux referred to the inner area (Eq. 3.17).

$$T_{max \, wall} = T_{film} + q_{normal} \, R'_{cond} [°C]$$

The analysis is conservative, indeed the obtained temperature is overestimated since the resistance is specified on the inner area, while the flux to the normal one which is smaller.

3.2.3 Convection heat losses

Knowing the surface temperature of the tubes it is possible to evaluate convective and radiative losses, both forced and natural convection are considered in this model. The method recommended by Sieber and Kraabel [14] to account for mixed convection is to combine estimates for forced and natural convection heat transfer coefficients for a given receiver in the following manner:

$$h_{mix} = (h_{fc}^a + h_{nc}^a)^{1/a}$$

The recommended value for a for a cylindrical external-type receiver is 3.2.[14]

3.2.3.1 Forced convection

If pure forced convection acts alone, a cylindrical, external-type receiver will look like a high temperature, short aspect ratio, rough cylinder with a spatially varying boundary condition (i.e. T_{wall} and q_{wall}) in a turbulent, and possibly non-steady crossflow.

The problem of spatially varying boundary condition has been already addressed by Sieber and Kraabel in [14], the authors recognize that the varying T_{wall} and q_{wall} most likely have some effect on the estimated heat loss, but they are not aware of any studies which address the case

of a cylinder in a crossflow with boundary conditions other than uniform heat flux or uniform wall temperature. They therefore considered a boundary condition with a constant average temperature of the wall, since it is probably easier to be estimated than the average q_{wall} and since little information exists for the uniform q_{wall} boundary condition.

The effects of surface roughness on forced convection heat transfer must also be considered. Sieber and Krabel for the same geometry investigated here, propose a set of correlations (Table 3.4) starting from a work of Achenbach [62], which is the most closely related study to forced convection on a rough receiver surface. Achenbach in his study considers a cylinder in crossflow with uniformly spaced, three-dimensional, pyramidal shaped roughness elements.

The results of Achenbach show that for rough cylinders there is a certain value of Re_D which must be exceeded before roughness has an effect on the average heat transfer from the cylinder. For Reynolds numbers below this critical Re_D, a smooth cylinder correlation can be used. The geometric parameter k_s/D also affects the choice of the correlation. k_s is the effective sand grain roughness height; for the geometry analysed in this work, Sieber and Kraabel [14] recommend the radius of a single receiver tube as an approximation for k_s.

Rugosity (k_s/D)	Region of validity	Correlation	
0 – smooth cylinder	All Re_D	$Nu_D = 0.3 + 0.488 Re_D^{0.5}\left(1 + \left(\frac{Re_D}{282000}\right)^{0.625}\right)^{0.8}$	*Eq. 3.19*
$75 x 10^{-5}$	$Re_D \leq 7x10^5$	Use smooth cylinder correlation (Eq. 3.19)	
	$7x10^5 \leq Re_D \leq 2.2x10^7$	$Nu_D = 2.57x10^{-3} Re_D^{0.98}$	*Eq. 3.20*
	$Re_D \geq 2.2x10^7$	$Nu_D = 0.0455 Re_D^{0.81}$	*Eq. 3.21*
$300 x 10^{-5}$	$Re_D \leq 1.8x10^5$	Use smooth cylinder correlation (Eq. 3.19)	
	$1.8x10^5 \leq Re_D \leq 4x10^6$	$Nu_D = 0.0135 Re_D^{0.89}$	*Eq. 3.22*
	$Re_D \geq 4x10^6$	$Nu_D = 0.0455 Re_D^{0.81}$	*Eq. 3.21*
$900 x 10^{-5}$	$Re_D \leq 1x10^5$	Use smooth cylinder correlation (Eq. 3.19)	
	$Re_D \geq 1x10^5$	$Nu_D = 0.0455 Re_D^{0.81}$	*Eq. 3.21*

Table 3.4 Correlations proposed by Sieber and Kraabel [14] *accounting for the effect of surface roughness in external receiver forced convection*

The receiver model calculates surface roughness for every receiver geometry considered. For the calculation of the Reynolds number properties of air at ambient temperature are used and the velocity is the one of the wind, which can be set in the input panel as the ambient pressure and temperature. The roughness and Reynolds number results show that the best fitting correlation for all the designs is the Eq. 3.22.

The convective heat transfer is calculated only once for all the panels as:

$$h_{fc} = \frac{Nu k_{amb\ air}}{D_{rec}} \quad \left[\frac{W}{m^2 K}\right]$$

<div align="right">Eq. 3.23</div>

3.2.3.2 Natural convection

If natural convection acts alone, a cylindrical, external-type receiver can be considered as a set of flat vertical panels. In the model, for each panel, an average surface temperature is calculated as it is recommended by Sieber and Kraabel [14] to account for the spatially varying boundary condition.

According to Sieber and Kraabel [14] no information is available on the effects of vertical ribbed roughness on natural convection from a vertical surface, although the fact that the roughness elements protrude through the viscous sublayer suggests that they will cause the heat transfer to be greater than that on a smooth surface.

It is recommended, as a best "guess" on the maximum effect of the vertical ribs on natural convection, to use of the total surface area of the ribs as opposed to the circumferential area of the receiver surface. This will be implemented by modifying the smooth surface h_{nc} by $\pi/2$, which is the ratio of the total rib surface area to the circumferential receiver area of the receiver surface.

Free convection is caused by a change in density of a fluid due to a temperature change or gradient. Usually the density decreases due to an increase in temperature and causes the fluid to rise. This motion is caused by the buoyancy force. The major force that resists the motion is the viscous force. The Grashof number is defined as the ratio of the buoyancy forces over the viscous forces, this number is used in natural convection correlation to assess the Nusselt number. Grashof number for the vertical flat plate is defined as:

$$Gr = \frac{g\,\beta\,\left(T_{avg\ panel} - T_{amb}\right) H_{rec}^3}{v_{air}^2}$$

<div align="right">Eq. 3.24</div>

Where g is the gravitational acceleration, β is defined as $^1/_{T_{amb}}$ and v_{air} in the cinematic viscosity of air at ambient pressure which is defined as $^{\mu_{air}}/_{\rho_{air}}$.

The correlation proposed by Sieber and Kraabel [14] for natural convection is:

$$Nu = 0.089 Gr^{\frac{1}{3}} * \left(\frac{T_{avg\ panel}(K)}{T_{amb}(K)}\right)^{-0.14}$$

<div align="right">Eq. 3.25</div>

Heat transfer coefficient for external natural convection is calculated from Nusselt number in the same way as for forced convection and then it is multiplied by $\pi/2$ to account for roughness as described above.

$$h_{nc} = \frac{Nu * k}{d_{ext}} * \frac{\pi}{2}$$

The mixed convective heat transfer coefficient is calculated with Eq. 3.18.

Convective losses specific on the control volume area can be evaluated as:

$$q_{conv} = h_{mix} * (T_{avg\ surf} - T_{amb})$$

3.2.4 Radiative heat losses

Radiative losses can be divided in two components, missed absorbance losses, due to the reflection of part of the irradiation hitting the receiver and emittance losses due to the phenomenon of emission of radiation from the tubes due to their high temperature.
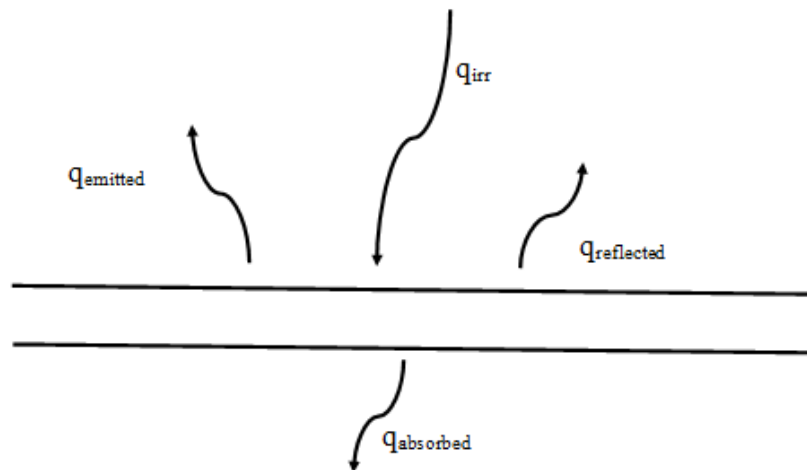
Figure 3.9 Radiative heat losses

Usually absorbance and emittance are linked together and if absorbance is high also emittance is high. In order to increase absorbance of the receiver a special coating is usually put on the external surface of the receiver tubes.

The most common absorber coating for external receivers is Pyromark 2500 [16], which is a black silicone-based paint with high temperature stability. It has a high solar absorptance of about 0.93 but also has a high emittance ($>$0.85) at elevated operating temperatures. Even if the high emittance penalizes the thermal efficiency of the receiver, this coating has been chosen for this work because it can sustain high temperatures, large heat fluxes, and a large number of thermal cycles before degrading.

71

Losses due to absorbance can be calculated as:

$$q_{rad,abs} = (1 - \alpha) * q_{irr} \quad \left[\frac{W}{m^2}\right]$$

Emittance losses are due to the fact that a body which is placed in a closed cavity with surrounding temperature T_{surr} emits radiation if its temperature T_{body} is higher than T_{surr}.

The receiver can be considered as a body with non-uniform surface temperature contained in a cavity, in this case the ambient has a uniform temperature T_0 which is always lower than the temperature of the receiver.

Assuming T_0 to be equal to the ambient temperature is wrong, as suggested by Castelli [45], because it would mean assuming that the temperature of the sky is equal to the ambient temperature, which is a bad approximation.

The temperature of the ambient must thus be determined taking into account both the temperature of the ground and the one of the sky.

The ground was considered to be at ambient temperature while the sky temperature must be estimated with the formula taken from Swinbank [63]:

$$T_{sky}(K) = 0,0552 * T_{amb}^{1,5}(K)$$

Hence, according to Berger et al. [64], T_0 can be calculated as:

$$T_0(K) = \sqrt[4]{\frac{\varepsilon_{sky} T_{sky}^4(K) + \varepsilon_{gr} T_{amb}^4(K)}{\varepsilon_{sky} + \varepsilon_{gr}}}$$

The radiation emitted is dependent from the wall temperature of the tube in the control volume:

$$q_{rad,emitt} = \varepsilon * \sigma * (T_{wall\ ext,i}^4(K) - T_0^4(K))$$

3.2.5 Conclusions

The calculation of thermal losses is an iterative procedure it self since the computation of the external temperature depends from the net flux, therefore inlet solar flux minus the losses, and thermal losses depend from that temperature, the flow diagram in Figure 3.10 shows the iterative procedure.
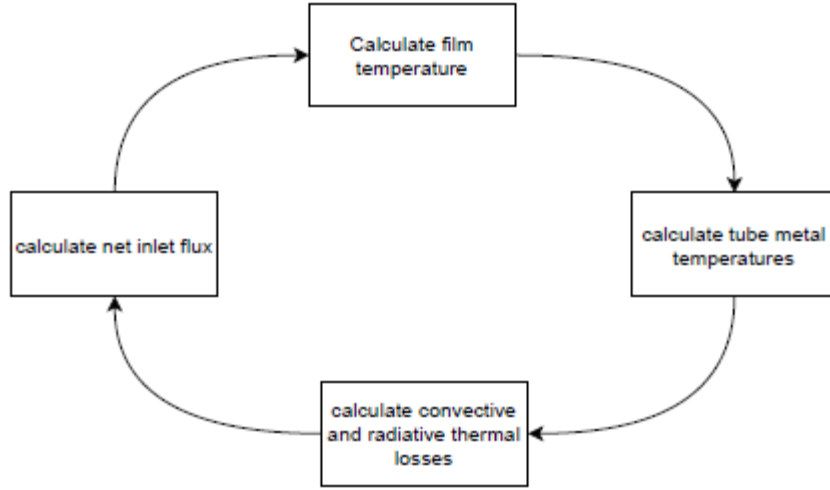
Figure 3.10 Panel thermal losses calculation flow diagram

Once all of the losses have been calculated the net absorbed radiation, calculated as the total radiation minus losses, can be used to calculate the thermal efficiency of the panel:

$$\eta_{th} = \frac{q_{abs,net}}{q_{irr}}$$

<div align="right">Eq. 3.32</div>

Then temperatures in the preliminary thermal balance sheet are adjusted to match the enthalpy rise of the fluid associated with net absorbed heat flux (Δh_{sun}) and the heat flux needed to have that temperature change of the HTF in the considered panel (Δh_{HTF}).

$$\Delta h_{sun} = \frac{q_{abs,net} * A_{panel}}{\dot{m}_{HTF}/n_{parallel\ passes}}$$

<div align="right">Eq. 3.33</div>

$$\Delta h_{HTF} = h_{HTF}\left(T_{out\ panel}\right) - h_{HTF}\left(T_{in\ panel}\right)$$

<div align="right">Eq. 3.34</div>

Lastly the total receiver efficiency is calculated as the average of the panels efficiencies, known this value the model adjusts the heat input required to supply the required the heat output.

3.3 Receiver pressure drop model

The evaluation of pressure losses in the receiver is fundamental to define the electric consumption of the HTF pump, which is the main auxiliary power consumption of the plant.
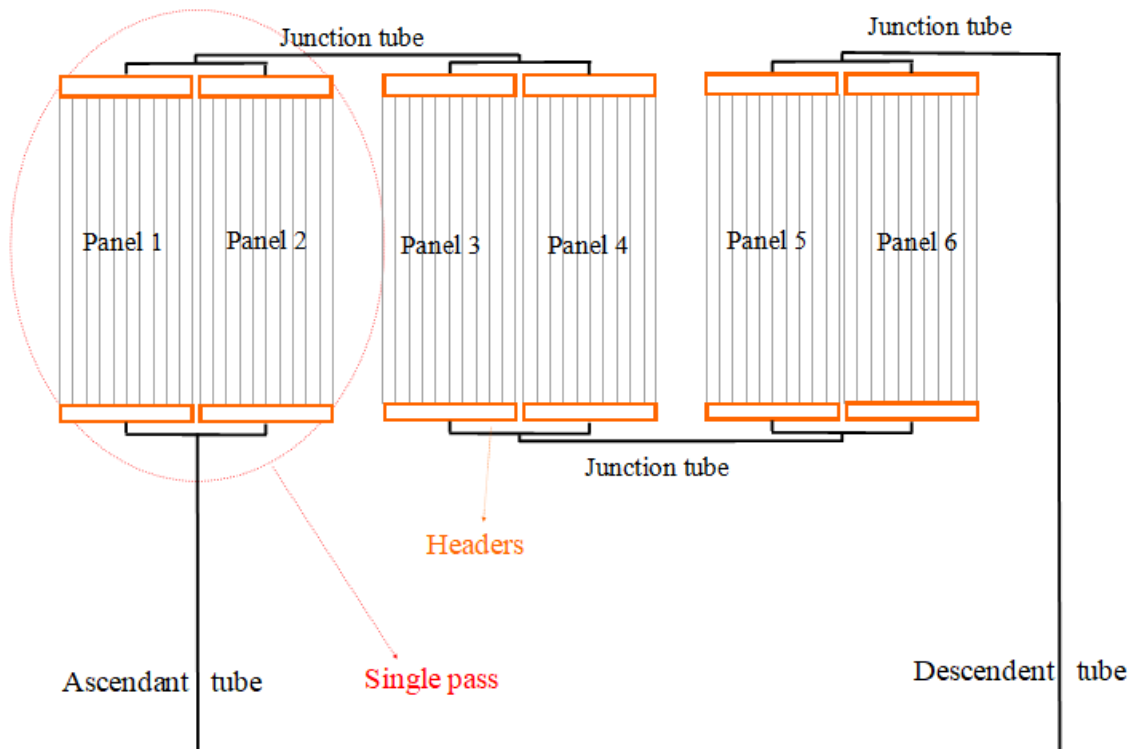
Figure 3.11 Receiver pressure loss scheme (single path representation)

The concentrated and diffuse pressure losses can be evaluated considering the geometry displayed in Figure 3.11; only one tube per pass is considered, since pressure losses in each tube do not sum due to the parallel flow arrangement. The distance travelled by the fluid in the header considered is the maximum one ($L_{header}/2$) in order to be conservative, junction tubes between parallel panels are considered long as the total width of a panel times 0.75, moreover the junction tubes between passes are considered to be long as half of the panel width plus the diameter of the receiver since consequent passes are usually put on two opposite sides of the receiver in order to balance the sun flux (see flow arrangement in Figure 4.10), this is a conservative approximation, indeed are long as a circumference chord with an angle of 120°. The last junction tube, which links the last header to the descending tube, is instead considered to be long half a diameter because the descending tube is supposed to be located in the centre of the tower.

Lastly also the ascending tube from the tower is considered. In the calculation of the pump head the pressure drops on the descending tube is not considered because the fluid in that section is

falling therefore part of the potential energy of the fluid is used to win friction resistance to the falling motion, the rest of this energy is dissipated at the end of the tube with a lamination valve.

Many others such as Rodríguez-Sánchez [65] or Polimeni [12] considered the use of a potential energy recovery system (PERS) which reduces the parasitic power consumption of HTF pump, recovering the potential energy of the HTF at the top of the tower. The PERS consists in a radial or axial hydraulic turbine on the hot sodium pipe coming from the receiver, close to the bottom of the tower (Figure 3.12).

In this work a traditional dissipative passive system has been considered instead of a PERS, since there are no information of an hydraulic turbine with high temperature sodium as working fluid.
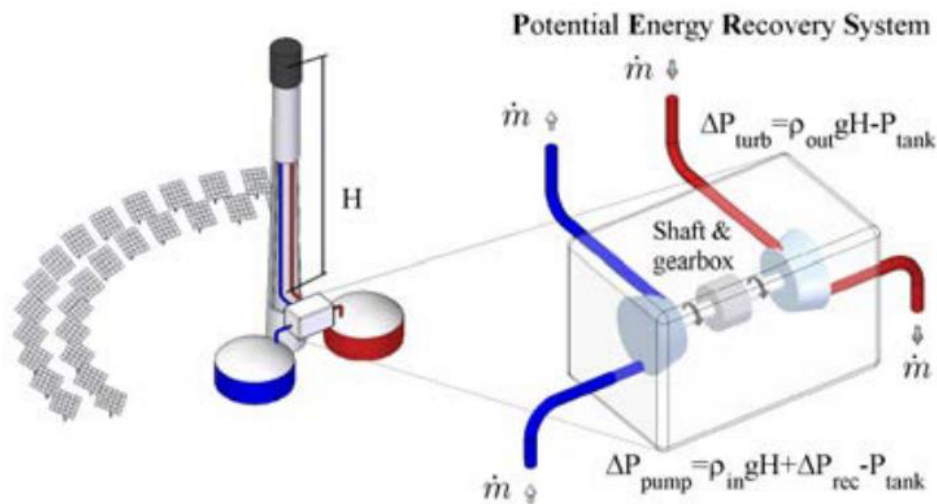
Figure 3.12 Potential energy recovery system (PERS) [12]

The model takes in input for each tube piece:

- Mass flow rate of the fluid ($\dot{m}$).
- Temperature in each tube section, which is useful to assess density (ρ) and viscosity (μ) of the fluid.
- Internal and external diameter (d_{int} and d_{ext}).
- Length (L).
- Roughness of the tube internal wall (ε), which in our case is always set to 45 μm.
- N° of inlets, outlets, curves at 180°, 90°, 45° or 30° and the N° of valves.

It subsequently returns as output the pressure drop in each section, which is calculated in a separate sheet using the input parameters and the calculated friction factor.

The model computes the volumetric flow rate $\dot{Q}$ in $[m^3/s]$, the flow area $[m^2]$ and the velocity of the HTF as:

$$v = \frac{\dot{Q}}{A_{flow}} \quad \left[\frac{m}{s}\right]$$

Reynolds number, which is useful in the calculation of the friction factor, is computed, it is also useful to assess the nature of the flow, which must be turbulent in order to insure a good heat transfer.

The friction factor λ is computed with the Colebrook equation for turbulent flow[3]:

$$\frac{1}{\sqrt{\lambda}} = -2\log_{10}\left(\frac{2.51}{Re*\sqrt{\lambda}} + \frac{\varepsilon/d_{in}}{3.71}\right)$$

Distributed losses can hence be calculated:

$$\Delta p_{dist} = \frac{\lambda}{d_{int}} * \frac{\rho * v^2}{2} * L \quad [Pa]$$

In order to assess the concentrated pressure drop (Eq. 3.38) the total concentrated loss coefficient is calculated multiplying the number of occurrences of each loss with their specific loss coefficient.

$$\Delta p_{conc} = \frac{C_{TOT} \, \rho \, v^2}{2} \quad [Pa]$$

The concentrated specific loss coefficients implemented in the model are the one reported in Table 3.5.

Concentrated loss type	C
Inlets	0.78
Outlets	1
180° curves	1.05
90° curves	0.75
45° curves	0.35
30° curves	0.525
Valves	0.45

Table 3.5 Concentrated loss coefficients used in the receiver pressure losses model

For the tubes in the panel six curve at 45° are considered due to their particular shape needed to avoid compression stresses when the material dilatates due to high temperature.

In order to evaluate the consumption of the pump both pressure losses and tower height must be considered, thus the total head of the pump is:

$$\Delta p_{pump} = \Delta p_{dist} + \Delta p_{conc} + H * g * \rho \ [Pa]$$

A reasonable value of 0.85 [66] has been assumed for the pump isentropic efficiency and the total consumption is:

$$W_{pump} = \dot{m} * \frac{v * \Delta p_{pump}}{\eta_{isentropic}} \ [W]$$

3.4 Solar field model

Simulation of the concentration of solar radiation incident on the heliostat field to the receiver aperture is handled using SolarPILOT, an open source software distributed by NREL[67]. SolarPILOT uses an analytical Hermite polynomial model to compute flux distributions on simple receiver shapes, such as the cylindrical receiver arrangement.

On the software, solar radiation can be modelled using a uniform angular distribution of intensity over the solar disk (0 to 4.65 mrad), also known as the "pillbox" sunshape. The solar radiation is reflected by the heliostats in the field towards the receiver.

Irradiation design conditions for the solar field are:

- 21 of June, summer solstice.
- Solar noon.
- Nominal irradiation of 950 W/m^2.
- Clear sky atmospheric attenuation model.

The location has been chosen near Las Vegas (35.57°N 115.47°W) where another CSP plant is built, the Ivanpah Solar Power facility, weather files for the specific location have been downloaded from NREL.

Many are the inputs required by the software, such as the tower height, which, in this case, is assumed to be 140 m as the one of Gemasolar Thermosolar Plant (19.9 MW), this assumption is reasonable since the electric power production is similar. A more accurate analysis should be made in future works in order to optimize solar tower height for this specific case.

Another input is the heliostat size, in order to implement realistic values in the software a commercial template supplied from CGGC-Supcon has been selected. The heliostats dimensions are 5.662 x 3.675 m and they are composed of 16 panels each, 4 rows and 4 columns. Optical performances of the heliostat have been assumed as the default values of SolarPILOT.

Once the inputs are given SolarPILOT builds a solar field optimizing the position of the heliostats over a selection of 4 representative days and 4 representative hours (simulation hour frequency of 5 h). The heliostat selection criteria chosen is "*total efficiency*", the software initially builds a layout which is compliant with land boundaries and layout rules, such as the maximum and the minimum field radius, subsequently it rates the efficiency of each heliostat, considering representative profiles, and lastly minimize their number, keeping only the most efficient heliostats, in order to comply with design power indications.

The aiming of the heliostats on the receiver is determined using an aiming strategy called "*Image Size Priority*" (ISP) to distribute the flux on the receiver aperture. The SolarPILOT user's manual explains "The image size priority aiming method determines heliostat aim position by sequentially placing heliostats on the receiver at points of lowest flux. The order in which images are placed is determined by the size of the image as it appears on the receiver. Therefore, images with significant distortion or at long distance from the receiver are typically placed first. After each heliostat placement, SolarPILOT identifies a local minimum in the flux intensity and locates the subsequent heliostat at that position. Heliostats aim points are placed within an allowable region that is determined by the size of image and the positioning cut-off value. The allowable region is offset from the edges of the receiver equal to a distance that is the product of the image size standard deviation times the positioning cut-off factor. As the image size or positioning cut-off factor increases, the allowable placement region contracts" [68].

The positioning cut off value influences the optical efficiency, which rises as the placement region shrinks, although if this parameter is increased too much the flux map is very concentrated, resulting in higher specific heat fluxes in the middle of the receiver which cannot be too high due to temperature limit of the receiver tubes' materials. For this reason, a brief analysis on the optimum cut off factor has been performed and will be reported in a later section.

For each layout studied, the receiver height and diameter, as well as the solar field design power, have been changed accordingly to the data obtained with the receiver design.

4 Preliminary design of the system

The purpose of this study is to extend the work of Polimeni [12], with knowledge coming from component manufacturers. The author performed some parametric analysis in order to optimize variables of the plant design, mainly taking in account technical limits coming from materials datasheet and the company's experience, in every layout considered receiver dimensions were changed in order to maintain a constant maximum temperature on the receiver surface.

The parameters optimized in the preliminary design regard mainly the receiver geometry, a few aspects of the solar field and the cycle parameters such as the expansion ratio of the turbine, which determines the lower pressure of the cycle considered a constant inlet pressure in the turbine, and the Ratio of Pressure Ratios (RPR) of the intercooled compressor. Lastly an analysis on the turbine inlet temperature was performed. The aim of these optimizations is to increase the efficiency of the single subsystems and, since many variables influence more than one subsystem, the overall solar to electric efficiency of the plant.

4.1 Technical limits for the preliminary design

In the preliminary design a few technical limits were accounted in order to design a plant which is not too far from reality. These limits were suggested by ESE and no in-depth research was performed.

4.1.1 Power block pressure

In the power block, maximum pressure has been set to 25 MPa as in Polimeni e al. [4], this limit must be placed due to stress resistance restriction of the material and the need to contain the costs, indeed a higher pressure would require more tenacious materials, higher thickness tubes and turbomachinery would have to work in harsher conditions, hence maximum pressure drives component cost. This limit value is consistent with the maximum pressure found in scientific papers on CO_2 cycles [30][69].

4.1.2 Temperatures

Another limitation is on the heat transfer fluid temperature: it cannot be lower than the solidification temperature of sodium (97.7 °C [3]), although this limit is not very stringent since the cycle is recuperated and CO_2 enters the primary heat exchanger at temperatures higher than 500°C; it cannot be higher than the evaporation temperature of sodium (873 °C [3]), therefore the film temperature (temperature of the fluid in contact with the tube wall) must be controlled.

The used absorber coating in this study is Pyromark 2500, which can sustain temperatures up to over 1000°C [16], hence it should not be a stringent limit. When this coating is exposed to very high temperatures, as the operating ones of these receivers, it degrades in a very short period of time. This degradation phenomenon happens for all temperatures above 600°C, the

higher is the exposure temperature the shorter is the time before degradation occurs. Many studies research the effect of temperature and coating thickness on the degradation phenomenon, such as Ambrosini et al. [70], for this study the article of Coventry and Burge [71] has been taken as reference. In their work Coventry and Burge study the effect of the thickness of the coating and of the base metallic material to assess the degradation of the coating paint after 10h, 100h and in some cases 200h. Using Haynes 230® as tube material the absorptance results showed in Table 4.1 are reported.

Thickness	Aging temperature	Absorptance			
		Initial	10 h	100h	200h
μm	°C	%	%	%	%
12	600	96.6	96.5	96.5	96.4
16	600	96.7	96.7	96.6	96.6
11	750	96.7	96.6	96.1	
14	750	96.7	96.6	95.7	
35	750	96.7	96.5	95.2	
11	850	96.7	92.7	92.3	
16	850		93.5	93.1	
36	850	96.7	93.1	93.2	

Table 4.1 Degradations results at various temperatures and thicknesses resulting from the work of Coventry and Burge [71]

At high temperature it is possible to assume an almost instant degradation (less than 10 h compared with a 20 years lifetime), although after the initial drop, the decline in absorptance appears to plateau, and even slightly recover [71], therefore an absorbance value of 93 % has been assumed, value which already accounts for high temperature degradation.

4.1.3 Stresses and cyclic strains

A very important limit which heavily influences the design is the receiver tubes material temperature limit. In order to evaluate the best possible performances of the plant, HAYNES® 230® alloy was chosen since it resulted, from a discussion with AC Boilers, the best candidate among the materials used for the manufacture of CSP receivers. This nickel-based alloy has high temperature strength and high thermal stability properties and it can sustain temperatures up to over 1000°C. Although, as for any metallic material, its strength properties degrade progressively rising the temperature, therefore an accurate stress analysis must be performed.

4.1.3.1 Tensile properties

Reported below in Table 4.2 are the tensile properties of the material taken from the alloy datasheet [18]:

Test Temperature	0.2% Yield Strength	Ultimate Tensile Strength	Elongation
°C	MPa	MPa	%
21	417	837	47.3
538	294	690	51.7
649	291	666	56.9
760	311	538	59.5
871	236	308	74.2
982	123	169	54.1
1093	69	90	37

Table 4.2 HAYNES® 230® tensile properties

The maximum stress sustainable at a specific temperature is calculated dividing the Yield Strength (YS) and the Ultimate tensile strength (UTS) by two different security coefficients (according to ASME design calculations [72]) and comparing them to choose the minimum value to be conservative.

$$\sigma_{max} = \min\left(\frac{YS}{1.5} \; ; \frac{UTS}{3.5}\right) \quad [MPa] \qquad \text{Eq. 4.1}$$

This stress was compared to the stress obtained with the Mariotte formula (Eq. 4.1) considering the worst working conditions of the receiver tubes.

$$\sigma_{mariotte} = \frac{PD}{2s} \quad [MPa] \qquad \text{Eq. 4.2}$$

To be conservative a pressure of 20 bar has been assumed, even if in the high temperature region pressure will be much lower (in the hottest regions it ranges between 5 and 12 bars), and the diameter of the tube has been set to 48.8 mm, an overestimated value since in all the designs the tube diameter is 33.4 mm.

4.1.3.2 Creep and Rupture Properties

Creep is the tendency of a solid material to deform permanently under the influence of persistent mechanical stresses and high temperatures. It can occur as a result of long-term exposure to high levels of stress that are still below the yield strength of the material, for this reason it is reasonable to assume that during its long lifetime the receiver will undergo this kind of degradation even if the stresses experienced are much lower than the yield stress.

From the datasheet [18], creep curves of the material at various temperatures can be extracted. The maximum allowable stress depends on the expected lifetime of the component and on the exposure temperature.
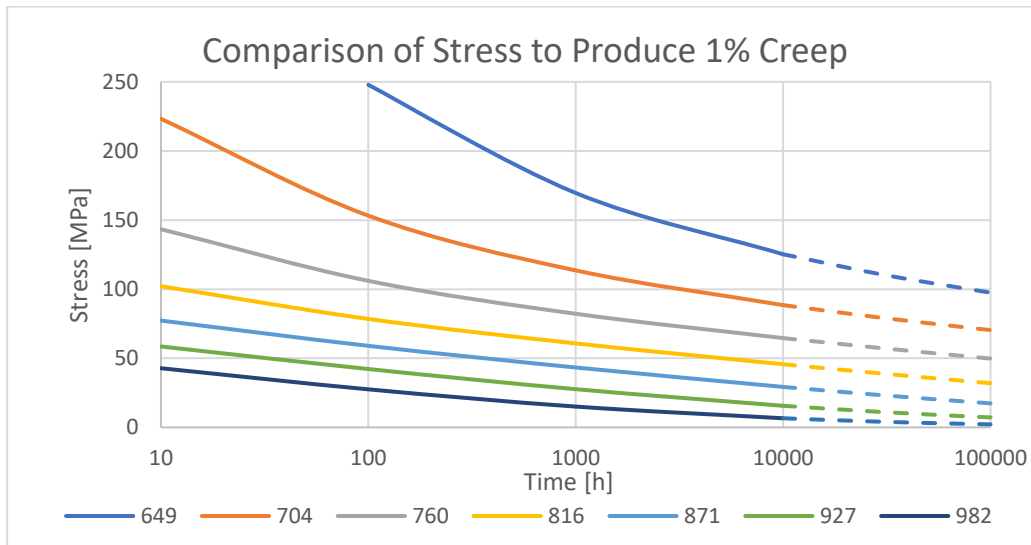
Figure 4.1 1% Creep curve for Haynes 230®

The chosen material has been tested only up to 10'000 h although a receiver with a 20 years long lifetime should work about 90'000 h, thus an extrapolation of creep data for a longer time is needed.

Creep data are often analysed using derived engineering parameters to correlate creep life (either time to rupture, or time to a specified strain) to applied stress and temperature. Commonly used formulations include Larson-Miller, Orr-Sherby-Dorn, Manson- Haferd, and Manson-Succop parameterizations, the Larson-Miller method was chosen for this study, due to its simplicity and since it is commonly used in the energy industry [73].

The Larson-Miller method of extrapolating stress rupture and creep results is based on the contention that the absolute temperature compensated time function should have a unique value for a given material depending only on the applied stress level σ:

$$\log \sigma = f[T(C + \log t)]$$

Eq. 4.3

where T (Kelvin) is temperature, t (hours) is either the stress rupture life t_r or the time to accumulate a certain amount of creep strain (e.g. 0.1% or 0.2%), and C is a constant usually assumed equal to 20, value verified for Haynes 230® [74]. The expression $[T(C + \log t)]$ is also called the Larson-Miller parameter.

Using the values listed in the datasheet it is possible to reconstruct the best fitting curve and then extrapolate the maximum stress values to obtain a creep of 1% at the chosen time and temperature.
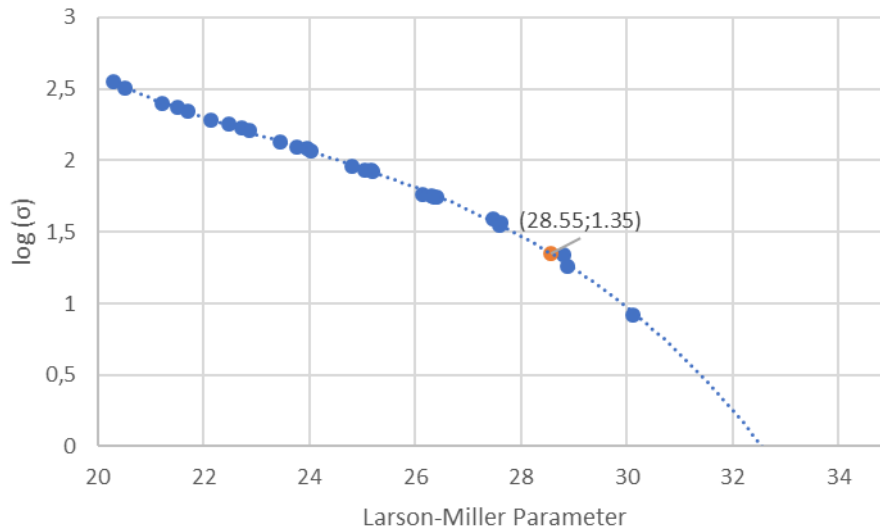
Figure 4.2 Larson-Miller extrapolation

A creep time of 90'000 h and a temperature of 871°C correspond to a Larson-Miller parameter of 28.55, which results in a maximum creep stress of 22.47 MPa. The maximum stress value is higher than the Mariotte stress calculated with an external diameter of 33.4 mm, a thickness of 1.65 mm and a pressure of 2 MPa, equal to 18.24 MPa; therefore operating the receiver at this temperature shouldn't provoke creep damages.

4.1.3.3 Low cycle fatigue

It's important to address also the problem of cyclic stresses in the tubes' material. Indeed tube walls experience high periodical thermal stresses which evolve in small cyclic deformation of the material, which influence the life of the receiver.

Axial stress arising from the thermal expansion of the receiver tube is managed through the use of bellowed tube or bends with oblique attachment to the manifold as it is shown in Figure 4.3. Under a non-axisymmetric heating condition, the tube front-side is hotter than the back-side which remains roughly at the temperature of the heat transfer fluid (Figure 4.3). The tube cross section net axial stress is zero but there exists a bending stress with compression front-side and tension back-side [75].
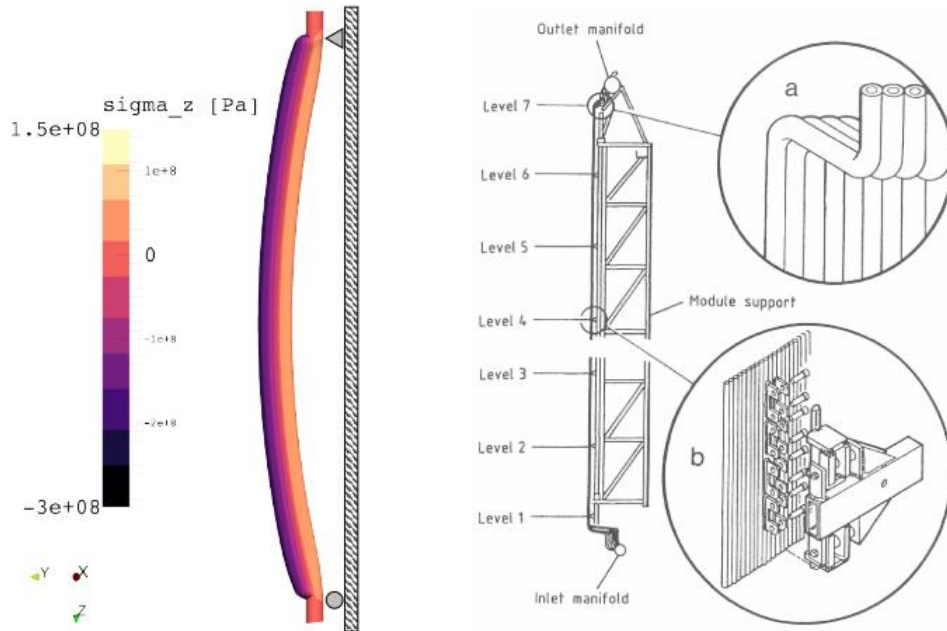
Figure 4.3 Stresses on the tube wall (a) and structure of the tubes on the panel (b) [75]

The equivalent axial thermal strain on the tube walls due to this phenomenon is a function of the temperature gradient between the front and back of the tube and can be calculated with Eq. 4.4, found in the work of Bradshaw et al. [76] written on the experience of the Solar two facility at Sandia National Laboratories in the U.S.A..

$$\varepsilon = a \left[\frac{T_{max\,wall} + T_{film}}{2} - \left(T_{bulk} + \frac{\left[\frac{T_{max\,wall} + T_{film}}{2} - T_{bulk} \right]}{\pi} \right) + \left(\frac{T_{max\,wall} - T_{film}}{2(1 - v)} \right) \right]$$

Eq. 4.4

where: ε = total thermal strain, $a = 10.9x10^{-6}$ = coeff. of thermal expansion, $T_{max\,wall}$ = maximum wall outer temperature, T_{film} = tube inner wall temperature T_{bulk} = sodium bulk temperature, $v = 0.24$ = Poisson's ratio.

The equivalent thermal strain must be compared to the maximum low cycle fatigue strain sustainable from the tube material. Low cycle fatigue is a phenomenon in which components are subject to mechanical cyclic plastic strains that cause fatigue failure within a short number of cycles. Indeed receivers are subject to a low number of cycles with respect to other pieces of equipment (for example a motor rotor experiences usually 3500 cyclic stresses per minute), although they experience high stresses which induce small periodic deformation on the tube

walls, in this thesis a value of 14'600 cycles has been assumed, considering two cycles a day (a cloud could obscure the sun on average of once a day) for 20 years of operation.

The alloy chosen for the receiver tubes is HAYNES 230® which exhibits the following low cycle fatigue properties at elevated temperature:
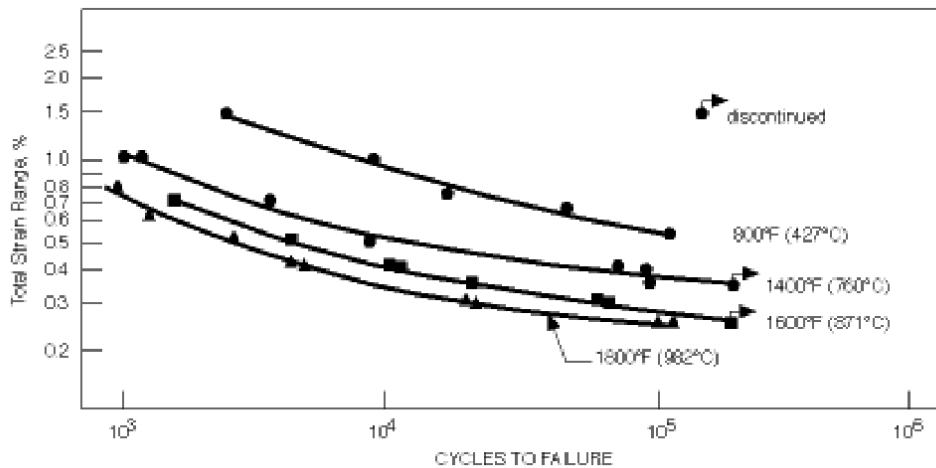
Figure 4.4 Low cycle fatigue properties of HAYNES® 230® [18]

The chosen limit for the maximum temperature of the wall of 871°C implies a maximum low cycle fatigue strain of about 0.3 for the assumed number of cycles.

When designing the receiver, the author had to be careful not to increase too much the temperature gradient across the tube wall to maintain the strain below this limit value. The choice of the flow path in the different passes of the receiver was influenced by this limit. Indeed, the inlet coldest fluid cannot cool down the panel which receives most of the flux, as it would be convenient in order to decrease the maximum wall temperature, because the resulting temperature gradient across the tube wall would be too high.

4.1.4 Flow velocity in tubes

Another limited parameter is the velocity of sodium in the receiver's tubes which cannot exceed 6 m/s due to corrosion and erosion problems, this value is suggested from Asselineau et al. in [77] where the Sodium-NaK engineering handbook [5] is cited, this book was sponsored by the U.S. government as a method to centralize the knowledge gained with the experience of nuclear sodium cooled fast reactors and to provide guidelines and information useful for the design, engineering, and development of sodium systems and their components.

Sodium velocity limit is higher than the one for water (5 m/s) because sodium is less dense, hence it is expected to cause less erosion in tube curves and valves.

4.2 Performed analyses

With the previously reported assumptions and models, various parameters have been optimized in order to have the best performances in terms power block efficiency, receiver efficiency and optical efficiency, still complying with cited limitations.

4.2.1 Comparison with previous studies

In this analysis some known inputs and outputs of Polimeni's work have been implemented in the power block model designed by the author. The outcomes of this analysis, reported in Table 4.3.

	Unit	Polimeni		This work		Discrepancy
CO_2 Minimum temperature	°C	input	52	input	52	
Tamb	°C	input	35	input	35	
ΔT cold end regenerators	°C	Input	12	input	12	
Turbine pressure ratio	-	input	3.5	input	3.5	
Maximum pressure	MPa	input	25	input	25	
Compressor efficiency	%	input	85%	input	85%	
Mechanical efficiency	%	input	99%	input	99%	
Electrical efficiency	%	input	99%	input	99%	
Δp p/ HP side of regenerator	-	output	not reported	input*	0.01	
Δp p/ LP side of regenerator	-	output	not reported	input*	0.015	
Δp p/ PHX	-	output	not reported	input*	0.015	
Δp p/ precooler	-	output	not reported	input*	0.02	
turbine efficiency	%	output	not reported	input*	93%	
TIT	°C	output	723.6	input	723.6	
CO_2 mass flow rate	kg/s	output	221.38	input	221.38	
RPR	-	output	0.458	input	0.458	
Paux	MW	output	0.44	input	0.44	
SR	-	output	0.662	output	0.670	1.24%
Tin PHX	°C	output	521.3	output	512.6	1.66%
Net power of the power-block	MW	output	26.28	output	27.57	4.91%
eff PB	%	output	46.59%	output	46.64%	0.11%

Table 4.3 Comparison with Polimeni's work [4]

Table 4.3 shows there is some discrepancy between the results reported in the article and the ones calculated with the present model. This discrepancy arises from the differences between the two models, indeed the power block model designed by Polimeni et al. [12][4] includes the iterative calculation of pressure drops and of the turbine efficiency, while in this work the

power cycle model is simplified in order to focus on the receiver model and on technical limits therefore these variables are assumed as inputs.

This difference could be overcome if the assumptions of this work where the outputs of Polimeni's work, although many outputs, such as the turbine efficiency and pressure drops, are not reported in the article.

4.2.2 Power cycle Optimization

The analysis started from the power block where the first parameter of optimization is the minimum pressure of the cycle, which can be calculated from the expansion ratio (β) of the turbine and the pressure losses in heat exchangers.

Another parameter which needs attention is the ratio of pressure ratios (RPR), defined as in Eq. 2.11. In conventional Brayton cycles using an ideal gas as working fluid the RPR which ensures the minimum compression work is the one that divides equally the pressure step on the two compressors ($\beta_1 = \beta_2$) [78]. When working with a real gas, however, this condition doesn't apply since real gas effects are present, hence an optimization of the recompression ratio must be performed for each minimum pressure considered.

4.2.2.1 Influence on optimal intermediate pressure of minimum pressure

Considering a turbine inlet temperature of 723.6 °C, starting value taken from the optimization found in the work of Polimeni et al. [4], a parametric simulation has been performed where the expansion ratio and the recompression pressure ratio has been varied, initially starting from optimum values reported by Polimeni et al. [4] with a wide discretization and subsequently moving to the optimum point with a tighter one. Results are reported in Figure 4.5.

a *b*
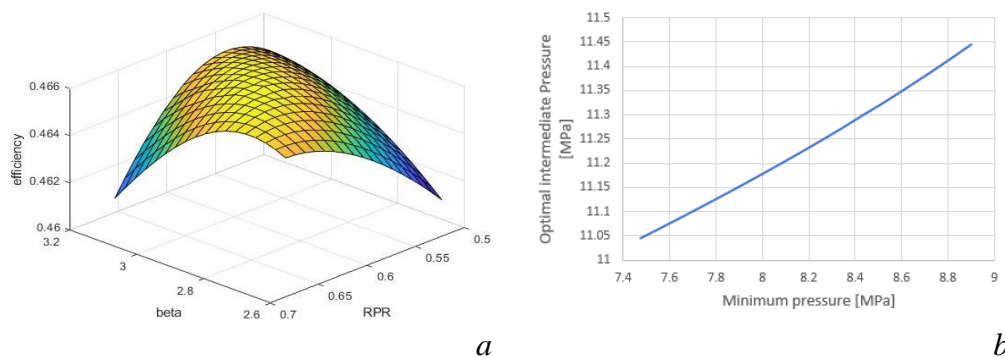
Figure 4.5 a) Optimization of β and RPR for the 723.6 ° C TIT case b) Optimal intermediate pressure as function of minimum pressure

The graph in Figure 4.5.*a* shows that the optimum value of RPR decreases as beta increases and therefore at lower minimum pressures, in order to explain this behaviour it is important to

remind that intermediate pressure is inversely proportional to the RPR and also to the turbine β.

$$P_{intermediate} = \frac{P_{max}}{1 + RPR + RPR \left(\frac{P_{max}}{P_{min}}\right)}$$

It's easier to understand the effect of minimum pressure on the optimal intermediate pressure graphing the intermediate pressure as a function of minimum pressure. Graph in Figure 4.5.*b* shows that the intermediate pressure increases increasing minimum pressure (hence decreasing β). This phenomenon can be explained by the fact that at lower minimum pressures the operating conditions of the first stage of the intercooled compressor are far from the critical point (blue T-s diagram in Figure 4.6), causing that stage to not benefit from the real gas effects. Therefore, to keep the compressor work as low as possible, the optimal $P_{intermediate}$ is lower.

At high minimum pressures, indeed, also the first stage of the compressor, as the second one, works in conditions close to the critical point (orange T-s diagram in Figure 4.6), hence the intermediate pressure can be increased without a strong penalization on the first compressor consumption, resulting in even better conditions for the second stage (due to the lower inlet specific volume).
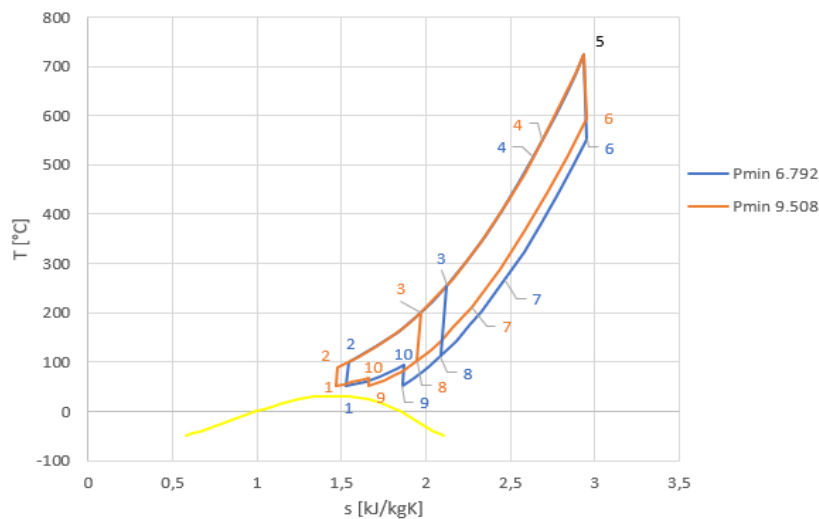
Figure 4.6 Comparison of T-s diagrams of a low minimum pressure cycle and a high minimum pressure cycle

Even if P intermediate decreases, it does not decrease as much as the minimum pressure, indeed the pressure ratio of the first compressor increases, this is due to the fact that in case intermediate pressure decreased too much, inlet conditions of the secondary compressor would

move to higher specific volumes and it wouldn't be possible to exploit beneficial real gas effects on the second stage either (concept can be visualized in Figure 4.7).
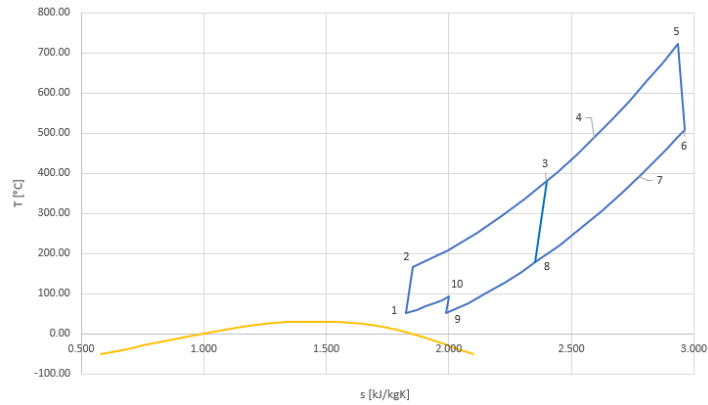
Figure 4.7 No real gas effect case: Pmin = 4.754 Mpa, Pint = 7.297 Mpa

4.2.2.2 Influence of the turbine inlet temperature on the optimal expansion ratio

As a second analysis the author investigated the relation between turbine inlet temperature and the optimal beta. In this parametric simulation temperature is progressively increased up to a value of 785 °C, beta and RPR are optimized with the SOLVER tool of Excel to increase as much as possible cycle efficiency.
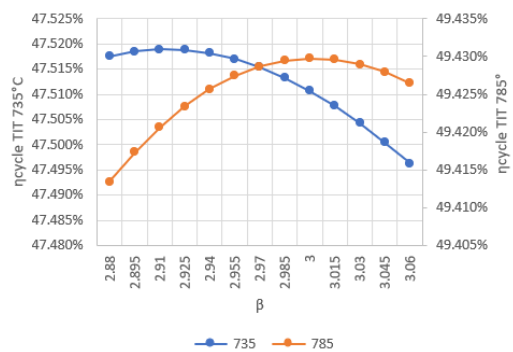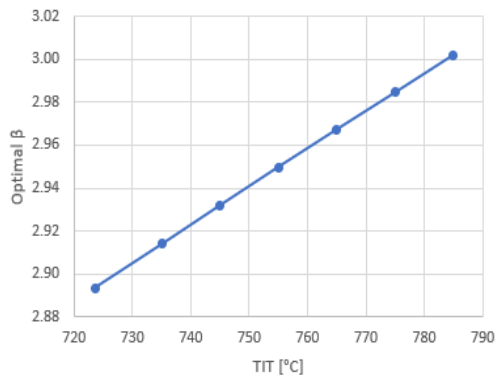
Figure 4.8 a) Optimal turbine expansion ratio as function of the turbine inlet temperature (RPR optimized); b) efficiency changing β for two TIT cases

The graph shows that the optimal minimum pressure (directly dependent from the expansion ratio since P_{max} is fixed) decreases as the maximum temperature is increased.

To explain this trend, it is useful to consider a simple closed Brayton cycle with an ideal gas as working fluid and real machines. Increasing turbine inlet temperature can be represented adding

89

a new part of the cycle. The new part of the cycle has higher efficiency that any real cycle since ideal the compression stage has higher than 1 efficiency. Thus the introduction of this part of cycle will enhance the overall cycle efficiency.
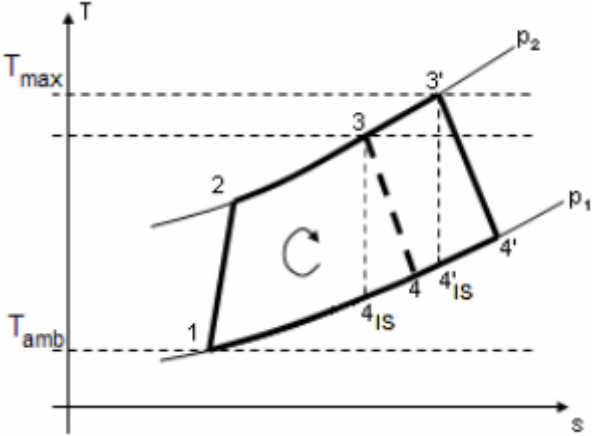
Figure 4.9 effect of increasing TIT on a real closed Brayton cycle operating with ideal gas

The increase of overall cycle efficiency due to increased temperature is enhanced by the increase of β, because it allows to reduce the inlet power and the rejected power.

In case regeneration is present optimal beta is decreased with respect to the optimal value for a simple cycle, because the heat recoverable is less when the outlet temperature of the turbine is lower (therefore with lower minimum pressure). The effect of increasing TIT maintains its effect on efficiency and optimal expansion ratio.

This cycle works in the real gas zone at low temperature and this has a positive effect on the compressor which needs less work in input. In order to obtain this beneficial effect the minimum pressure must be set similar to the critical pressure therefore optimal beta cannot increase too much. The turbine, instead, works in an ideal gas zone due to high temperatures, therefore the turbine inlet temperature shouldn't have an impact on real gas effects.

4.2.3 Heat exchangers pressure drops

The necessity of a modelization of pressure drops on the heat exchanges aroused from an examination of the absolute pressure drops on the cold side of regenerators resulting from results and assumptions found in the work of Polimeni et al. [4]. Indeed even if assumed specific pressure drop is lower on the cold side of HXs (Table 3.1) with respect to the hot side, the absolute pressure drop results higher for the cold side than for the hot side.

This condition is an anomaly since, in the considered pressure loss model, which can be found in Appendix A, geometry is assumed to be the same for the hot and the cold side, in the HTR mass flow rate is the same on both sides, therefore, due to the effect of lower density at higher

temperatures, the velocity of the fluid in the hot channels results higher than the one in the cold channels. This disparity is even more evident in the LTR where the mass flow rate of the hot fluid is imposed higher that the one of the cold fluid in order to have similar heat capacities on the two sides of the regenerator despite the real gas effects.

Pressure drops depend from the square of the velocity (Eq. 4.6), which, in turn, is inversely proportional to the density of the fluid (being the geometry fixed). Therefore pressure drops are inversely proportional to the density of the fluid, which decreases with temperature.

$$\Delta p = \frac{1}{2} f \frac{l_{node}}{d_{eq}} \rho v^2 + \frac{1}{2} C \rho v^2 = \frac{1}{2} f \frac{l_{node}}{d_{eq}} \frac{1}{\rho} \left(\frac{\dot{m}}{A_{channel}} \right)^2 + \frac{1}{2} C \frac{1}{\rho} \left(\frac{\dot{m}}{A_{channel}} \right)^2 \qquad \textit{Eq. 4.6}$$

Another parameter which influences pressure drops is the viscosity which is higher for colder flows. Friction factor increases for higher viscosities, although this effect is much less evident than the one of density.

The assumption on pressure losses must be consistent with these proportionalities, therefore a higher pressure loss on the colder side is not acceptable. For this reason, the author calculated the velocity which ensures the assumed pressure losses on the hot side. Given in input this velocity, temperatures on hot and cold side and the channel geometry, the model calculates pressure losses on the cold side and the channels' length.

Since temperatures across the regenerators are dependent from the pressure losses on the gas cycle, an iterative procedure to calculate pressure losses should be applied, although after the first iteration it was clear that the specific pressure loss on the cold side didn't vary much if pressure drops on the hot side were kept constant changing the velocity of the hot fluid, therefore a specific cold side pressure loss was assumed to be constant for each case (values reported in Table 3.1).

4.2.4 Receiver geometry

The receiver design is a complex task since this component has to operate at very high temperatures and heat fluxes, therefore many parameters must be kept under control, in order to comply with material limitations.

Many are the geometrical parameters which can be changed and optimized to observe these limitations, first of all the way the heat transfer fluid flows in the receiver.

Usually in commercial receivers there are two parallel flow paths each composed by a number of passes which are in series. Each pass can be composed from one or more panels with n tubes in parallel and two headers which distribute the flow equally in the tubes. If the pass has a too

large surface usually it is divided in more panels in order to ease transportability, moreover panels are flat, therefore the more there are the more the geometry of the receiver resembles a cylinder.

The number of parallel tubes on each panel depends on the width of the panel which is, in its turn, dependent from the diameter of the receiver. The simplified calculation of the number of tubes considers the receiver a perfect cylinder (Eq. 4.7).

$$n_{tubes\ in\ parallel} = \frac{\pi D_{receiver}}{n_{passes} D_{ext\ tube}}$$

The parameters which influence the velocity of the HTF in the receiver vessels are, according to the Eq. 3.35: most importantly the number of passes, which determines the number of parallel flows, the tube diameter, indeed when the tube diameter is increased the number of tubes which fit in a pass decreases, although the decrease of number of panels is directly proportional to the increase of the tube diameter while the increase of the flow area in each tube is proportional to the square of the diameter, therefore the total flow area increases linearly with the external tube diameter Eq. 4.8.

Lastly the flow area can be increased enlarging the receiver diameter although this parameter influences also the efficiency and the average specific heat flux incoming (considering a constant power), therefore it wasn't changed for the sole purpose of affecting the flow velocity.

$$A_{flow,tot} = n_{tubes\ in\ parallel} * \pi * \frac{D_{ext\ tube}^2}{4} = \frac{\pi^2 * D_{receiver}}{4 * n_{passes}} * D_{ext\ tube}$$

In order to comply with the velocity limitation of 6 m/s the number of passes has been decreased to three while the tube external diameter has been kept fairly small, 34.4 mm which corresponds to the 1 inch standard pipe. This choice was made since, considering a constant pressure, the Mariotte stress (Eq. 4.2) on the tube walls increases with the tube diameter. Since the Mariotte stress must be below the maximum allowable creep stress, the thickness, in case of higher tubes diameters, would need to be increased over the 1.65 mm previously assumed, which is not favourable for three main reasons: the heat transfer decreases, the temperature difference across the tube wall increase and the total cost of material increases.

The panels in series are connected so that the flow is distributed as symmetrically as possible on the cylinder, in this way when the operating condition is different from the design one, in example in the morning when irradiation comes mainly from the west (due to reflection of the mirrors), the outlet temperature of the two paths is not too different.
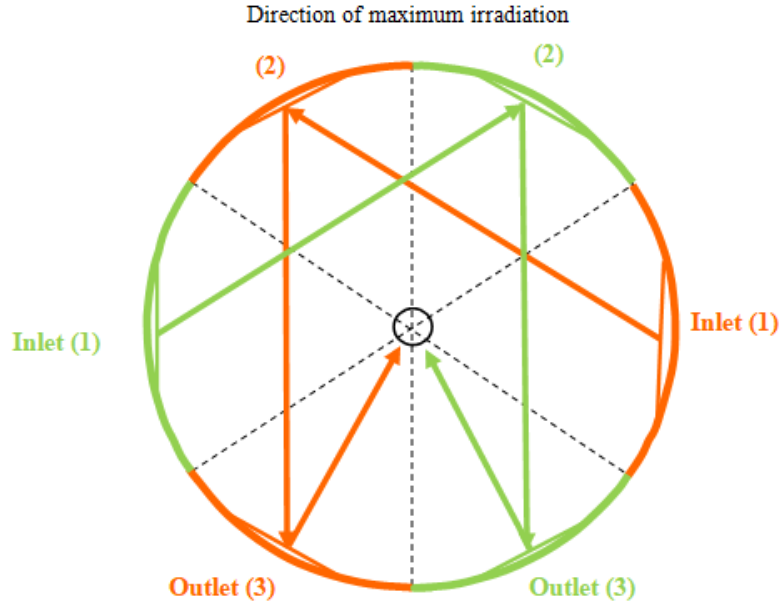
Figure 4.10 Flow scheme in the three passes receiver

In the reported flow scheme, which was chosen for this study, the HTF enters from the medium irradiated pass, goes in the highly irradiated one only once it is already heated up to a medium temperature and it flows in the least irradiated panel at last. It is convenient, to have a better cooling of the hottest area, to flow the cold HTF directly in the most irradiated area, although the high gradient between bulk temperature of the fluid and outside temperature of the tube contributes to the early failure of the material because of the cyclic different dilatation of the irradiated and the insulated parts of the tubes. In order to obtain a strain below the value of 0.3%, which is the maximum allowable to avoid low cycle fatigue failure during receiver lifetime, the maximum irradiated part must be cooled from the already heated HTF.

The total surface area of the receiver must be adjusted in order to comply with temperature limitations, in particular the most stringent constraint is the one on the tubes material, set to 870 °C, which results from the creep analysis of the Haynes® 230. If the surface area is increased the heat flux specific on the area decreases lowering the maximum temperature of the tube.

$$q_{irr\,avg} = \frac{P_{receiver\,duty}}{\eta_{th} S_{receiver}}$$ *Eq. 4.9*

The total surface area results from the choice of diameter and aspect ratio defined as:

$$AR = \frac{H}{D}$$ *Eq. 4.10*

The aspect ratio is optimized (optimization reported in paragraph 4.2.6) while the diameter is increased until the maximum wall temperature is below the limit.

4.2.5 Analysis on the positioning cut off factor

The flux map of the incident power on the receiver was initially approximated with a gaussian distribution (Figure 4.11) multiplied by an average value which ensures a certain power, although this distribution has lower peak fluxes given a certain average flux compared to a real flux map, in fact the shape of a real flux map is usually more concentrated in the middle of the height in order to decrease spillage losses.
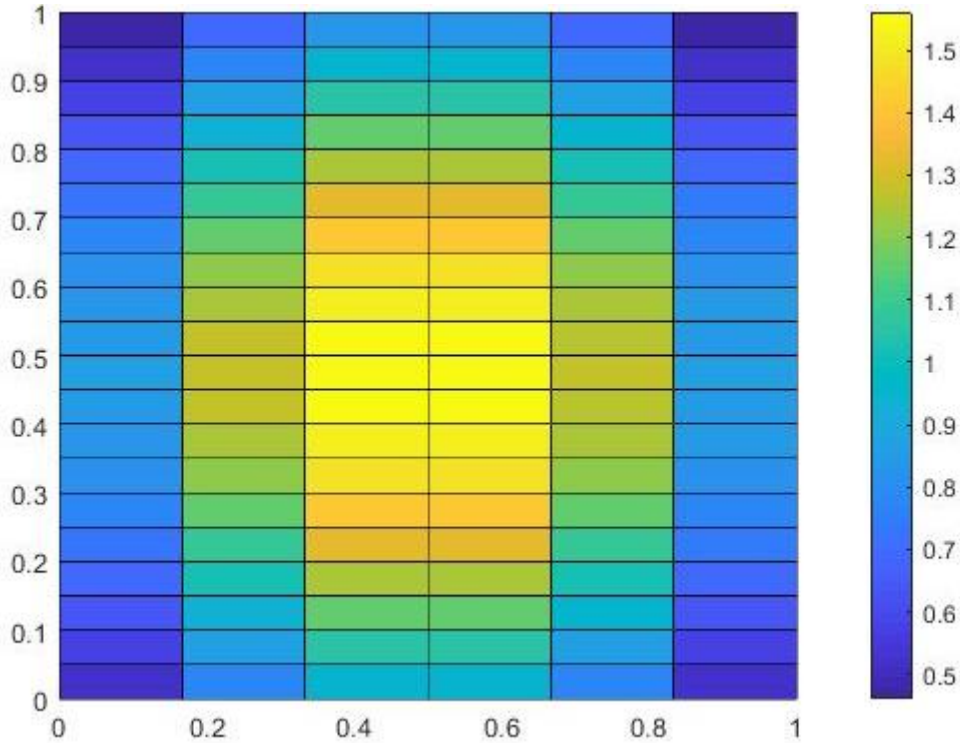
Figure 4.11 Flux map obtained with a double gaussian distribution

The real shape of the flux map depends from the aiming strategy which is used on the heliostat field, in this work the software SolarPILOT has been used to simulate a real flux map with the Image Size Priority aiming strategy, described in the solar field model.

When the software builds the flux map it places the reflection of each heliostat on the receiver surface starting from the farther ones, which project a larger image, and then proceeding to closer heliostats. Each heliostat image is focalized on the receiver surface maintaining a certain distance from the borders, this distance is calculated multiplying the cut off factor by the vertical dimension of the reflected heliostat image.

Changing positioning cut off factor the shape of the flux map changes, if this factor is increased the optical efficiency increases, particularly the image intercept efficiency, although the allowable aiming region shrinks resulting in higher peak fluxes in the middle of the receiver.

Although higher peak fluxes result in a local overheating of the material, to comply with temperature and stress limitations it is often necessary to increase the surface area of the receiver reducing the peak flux. With a larger receiver the power is distributed on a larger area therefore the average flux decrease, penalizing the thermal efficiency of the receiver due to the higher exchange surface area. In order to find the receiver size which would allow to maintain maximum tube temperature constant for each cut off factor case, an iterative procedure, described in the flow diagram in Figure 3.1, was used, this procedure take into account the interaction between receiver dimensions and flux map shape.

In Figure 4.12 the increase of receiver surface area is shown together with the increase of peak flux (lower that the increase which would result keeping the dimensions of the receiver constant) and lastly the decrease of average incident flux.
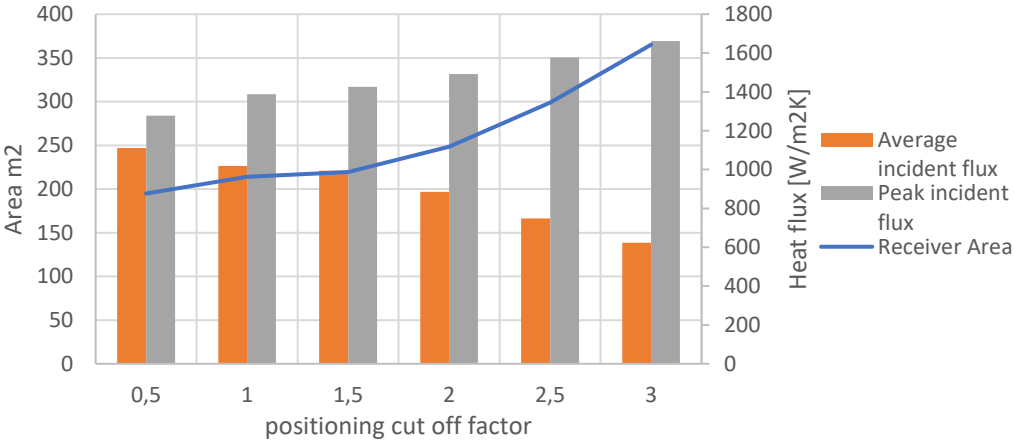
Figure 4.12 Cut off factor influence on receiver area and on peak and average heat flux

The trade-off between the optical and thermal efficiency has been investigated, choosing a constant aspect ratio of 1 and changing the cut off factor from 0.5 to 2.5. In this analysis the 765°C (TIT) cycle has been considered which correspond to a sodium outlet temperature of 780°C and inlet temperature of 583.3 °C, since a constant temperature difference of 15°C has been assumed both at the cold end and the hot end of the primary heat exchanger. Another constant parameter is the maximum tube wall temperature, which is kept fixed at 865°C.
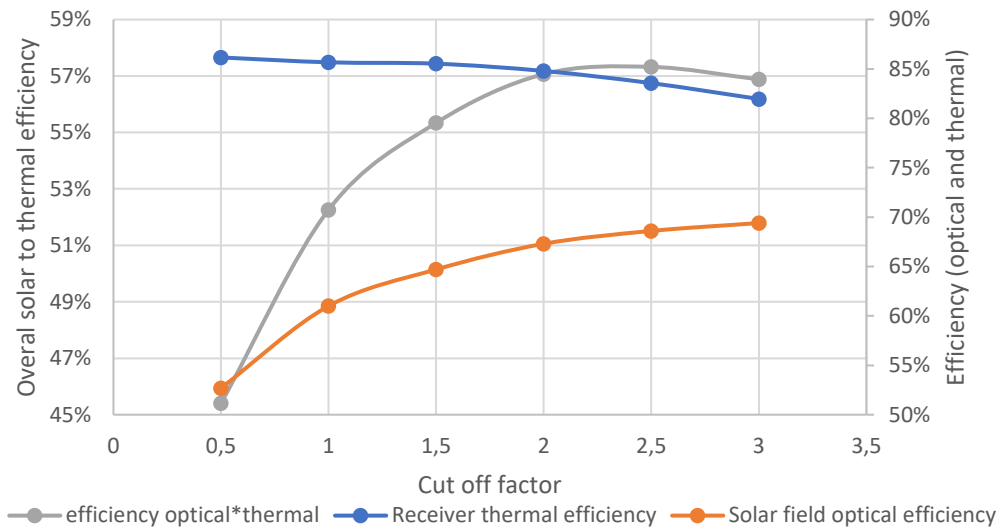
Figure 4.13 Cut off factor effect on optical and thermal efficiency

Trends of thermal and optical efficiency are the one expected, the overall efficiency solar to thermal power at the HTF increases up to a maximum around 2.5. Although efficiency is not the only performance parameter, indeed, as the cut off factor is increased, the surface area of the receiver increases more than proportionally (Figure 4.12). Since receiver area is linked to its cost a thermo-economical analysis should be made.

For the further analyses a value of 2 has been chosen, since total efficiency increases of less than 0.3% while to increase cut off factor from 2 to 2.5 area must be increased by 1/5 of the total surface.

4.2.6 Optimization of the aspect ratio H/D

The need of this optimization comes from the confusion which can arise due to the conflicting information which can be found in literature about receivers' height, indeed on the NREL site [67] it is possible to find information on solar towers operating or under construction and in some cases also the dimensions of the receivers. The reported height and diameter would suggest a tendency towards aspect ratios of about two. Although this information is misleading since the reported hights comprehend the insulated rings on top and bottom of the tube bundles. Data on receivers designed with the help of ESE, Engineering Services for Energy, such as Minos, suggest an aspect ratio closer to one, while usually AC Boilers designs receivers with aspect ratio H/D around 1.1-1.2 (DEWA CSP Tower Project, Solar One and Solar Two). Due to this uncertainty on the optimal aspect ratio an analysis on the optimization of efficiency changing H/D between 1 and 2 has been made.

What it is expected from this analysis is that an aspect ratio closer to one favours the optical efficiency, in fact the projection of the receiver on a flat surface is closer to a square, the

rectangle with the highest area/perimeter ratio, therefore, since spillage losses are related to the peripheric zones of the receiver, they should decrease when the perimeter of the 2D projection decreases.

Decreasing the aspect ratio is also beneficial in terms of flow velocity, since the flow distributes in more parallel channels, indeed the number of parallel channels depend on the receiver diameter (Eq. 4.8), but not on the receiver height. In this receiver design, adopting solutions which decrease flow velocity is important since, compared to solar salts receivers coupled with steam cycles, the temperature difference of sodium across the receiver is small (about 200°C compared to 250-280°C of solar salt plants) hence, to reach the same power, a high mass flow rate is needed.

Aspect ratio has been varied in the range from one to two, and for each H/D analysed a specific design of the receiver considering temperature and velocity limits has been made. The flux map is obtained with the software SolarPILOT considering a positioning cut off factor of two. Also for this analysis a constant turbine inlet temperature of 765°C has been considered, the power delivered to the HTF is also constant and it is derived from the optimization of the power block. The most important data on receiver design are summarized in Table 4.4.

H/D	-	0.98	1.1	1.3	1.5	1.8	2.1
$H_{receiver}$	m	8.584	8.991	9.632	10.523	11.428	12.293
$D_{receiver}$	m	8.759	8.028	7.525	7.110	6.530	5.910
Area	m^2	236.21	226.76	227.71	235.39	234.81	229.00
$D_{outTUBE}$	mm	33.4	33.4	33.4	42.2	42.2	42.2
Sodium flow velocity	m/s	4.94	5.42	5.79	4.57	5.03	5.59
max T tube	°C	865.10	865.03	864.99	864.98	864.95	865.05
n tubes per panel	-	68	62	58	44	40	36

Table 4.4 Receiver designs changing the aspect ratio

As the aspect ratio increases the number of parallel channels (n of tubes per panel Table 4.4) reduces resulting in a higher flow velocity (Table 4.4). For aspect ratios higher than 1.3 a tube outer diameter of 33.4 mm is not sufficient to keep flow velocity below 6 m/s, therefore the channel diameter must be increased up to 42.2 mm (standard 1-¼ inch pipe diameter) resulting in a worse heat exchange meaning that the metallic material is less cooled down from sodium, therefore the receiver area must be increased to avoid exceeding the temperature limitation. For this reason, increasing tube diameter is highly detrimental for receiver thermal efficiency and it should be avoided if possible.

The surface area of the receiver, needed to respect temperature limits, tends to decrease with higher aspect ratios and this is due to the fact that the positioning cut off factor decides the aiming position offset from the lower and upper border of the receiver without taking into account the height of the receiver, therefore the shortest is the receiver the smallest is the aiming

area resulting in a higher peak flux. As it was said before, there is a certain value of aspect ratio which maximizes the flow velocity with the diameter of 33.4 mm, consequently after that value of H/D a wider tube must be used resulting in a step increase of the surface area.
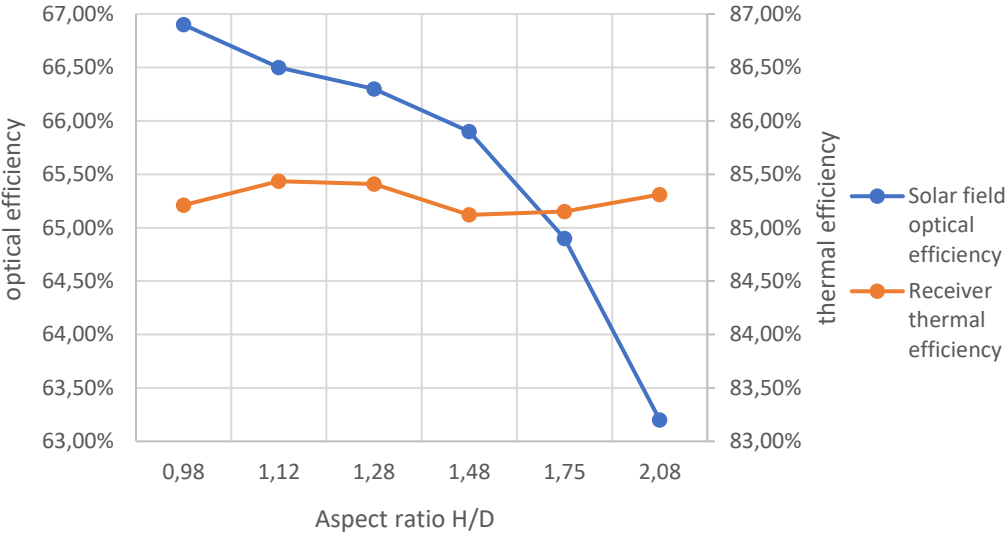
Figure 4.14 solar field optical and receiver thermal efficiency varying the aspect ratio of the receiver

As expected, the optical efficiency decreases as the aspect ratio increases not only due to the changing aspect ratio but also because of the decrease of the total receiver area, indeed between point 3 and 4 the slope of the curve is less steep because the area increases.

As it can be seen from Figure 4.14, thermal efficiency varies much less than optical efficiency. The expected trend would be for it to grow with the aspect ratio since the flux map is less peaked, but a negative step is expected between the third and the fourth point due to the increase of the tube diameter.
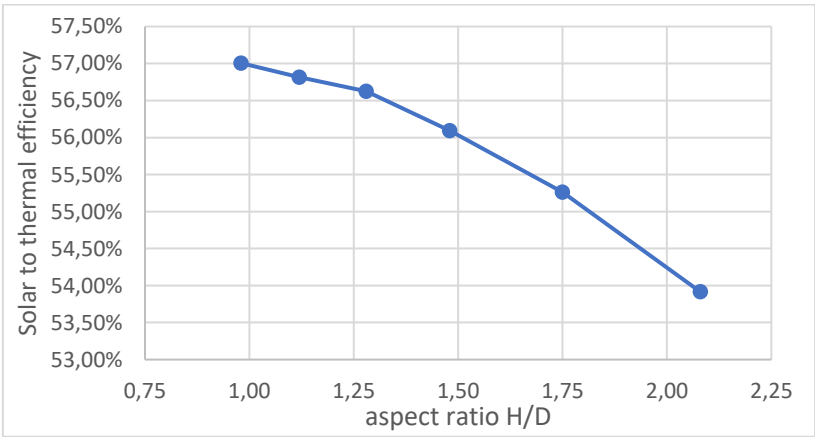
Figure 4.15 Total solar to thermal efficiency varying the aspect ratio of the receiver

Finally, an aspect ratio of 1 has been chosen for later analyses since the overall efficiency of the conversion from solar to thermal power of the HTF is monotonically decreasing for higher aspect ratios.

4.2.7 Turbine inlet temperature analysis

This is the most complete of the analyses performed since it optimizes the power block, the receiver and the solar field.

Turbine inlet temperature is changed from 723.6 °C (optimum temperature in the work of Polimeni et al. [4]) to 785 °C which correspond to a sodium temperature of 800°C.

For each temperature value the entire plant was designed starting from the power block, subsequently building the receiver and the solar field, which are linked together by the dependency of the flux map from the dimensions of the receiver and of the dimensions from the flux map, therefore an iterative procedure (described in the flow diagram in Figure 3.1) was actuated to find for each design the right diameter of the receiver which ensure a maximum temperature of the metal of about 865 °C (just below the temperature limit of 871°C). Lately pressure losses in the receiver have been calculated to assess the auxiliary consumption of the HTF pump from the tank to the receiver.

Starting from the power block, the model has been used in each case to optimize minimum pressure (optimizing β and fixing the maximum pressure to 250 bar) and recompression pressure ratio of the intercooled compressor. Mass flow rate of CO_2 has been calculated in each case in order to have a net power output of 30 MW, hence it depends from the efficiency of the power block.

Once the thermodynamic cycle has been designed the inlet and outlet temperatures of the CO_2 in the primary heat exchanger are defined. A constant temperature difference of 15°C has been assumed both at the cold end and the hot end of the primary heat exchanger, therefore sodium temperatures are given.

Another information used in the design of the receiver is the total heat exchanged in the PHX, which is, multiplied by the solar multiple (SM), the heat entering the HTF. In this work a SM of 3 has been considered since the plant needs to operate as base load, therefore the storage has to ensure 24 h operation at least in summer.

The receiver duty is in every case around 200 MW, the model of the receiver determines the average irradiation on the receiver surface which the solar field must ensure in design conditions. Many receiver specifications, such as the number of paths, passages and panels, the tube diameter and the thickness of the tube wall are not changed in the definitive layouts for the different cases, because they are optimized complying with the technical limitations. Aspect ratio and the positioning cut off factor have been optimized previously.

The solar field is designed using SolarPILOT, which requires in input the solar field design power (before the thermal losses), the dimensions of the receiver and heliostats, the solar tower height and the aiming strategy. With these indications the software creates an optimized solar field and calculates the flux map basing on the chosen aiming strategy. The flux map needs to be implemented in the receiver model because it influences the maximum temperature of the tube, therefore the receiver dimensions must be adjusted to comply with temperature limits. It's an iterative procedure since the shape of the flux maps depends from dimensions and vice versa.

Lastly the pressure losses in the receiver tower are calculated; since the velocity of the flow decreases with the TIT due to the increasing receiver diameter, the pressure losses decrease as well and the power consumed by the HTF pump is proportional to them.

In Table 4.5 the most important parameters of the designed plants are summarized.

		Units	Temperature [°C]						
			723.6	735	745	755	765	775	785
Power block	RPR*	%	60.56%	60.23%	59.94%	59.66%	59.39%	59.11%	58.84%
	B*	-	2.8949	2.9156	2.9336	2.9515	2.9692	2.9867	3.0041
	Pin PHX	kW	63800	63187	62667	62163	61675	61201	60742
	Tin PHX	°C	534.64	543.86	551.95	560.04	568.13	576.22	584.32
	mCO_2	kg/s	266.44	260.56	255.59	250.79	246.15	241.66	237.32
	PB efficiency	%	47.02%	47.48%	47.87%	48.26%	48.64%	49.02%	49.39%
receiver	$H_{receiver}$	m	7.878	8.042	8.193	8.361	8.616	8.905	9.470
	$D_{receiver}$*	m	7.878	8.042	8.193	8.361	8.616	8.905	9.470
	T_inlet	°C	549.64	558.86	566.95	575.04	583.13	591.22	599.32
	T_outlet	°C	738.60	750.00	760.00	770.00	780.00	790.00	800.00
	Na velocity	m/s	5.91	5.62	5.36	5.28	5.05	4.83	4.37
	max Ttube	°C	865.10	865.10	865.16	865.06	865.11	865.11	865.15
	max Tfilm	°C	756.88	767.00	776.23	784.97	793.90	803.05	811.92
	max strain	%	0.29%	0.27%	0.26%	0.24%	0.22%	0.20%	0.18%
	Receiver inlet power	MW	219.72	218.66	217.87	217.23	216.96	217.00	218.34
	Receiver duty	MW	191.40	189.56	188.00	186.49	185.02	183.60	182.23
	Thermal efficiency	%	87.11%	86.69%	86.29%	85.85%	85.28%	84.61%	83.46%
SF HTF pump	Aux receiver pump	MW	3.24	3.13	3.01	2.91	2.80	2.71	2.62
Solar field	Simulated heliostat area*	m^2	355878	351054	347360	344191	340740	338257	336743
	Simulated heliostat number*	-	17632	17393	17210	17053	16882	16759	16684

Average incident flux	kW/m^2	1126.6	1075.9	1032.7	988.9	930	870.9	775.6
Peak incident flux	kW/m^2	2115.5	1978	1865.8	1754.2	1606.7	1476.5	1328
Optical efficiency	%	65.00%	65.50%	66.00%	66.40%	67.00%	67.50%	68.20%
Net solar to electric efficiency	%	23.75%	24.15%	24.53%	24.84%	25.19%	25.46%	25.66%

Table 4.5 Design parameters of the different TIT plants (optimized parameters, all other parameters result from other choices)*

The power input required from the cycle decreases with higher TIT, and this is due to increasing cycle efficiency (Figure 4.17). The power block efficiency increases linearly with temperature and this is an expected trend since in can be explained with the Carnot efficiency.

Moving towards higher TIT, thus to higher sodium temperatures, the specific flux on the receiver must be lower in order to limit the material temperature, therefore the total surface of the receiver must grow (Figure 4.16).
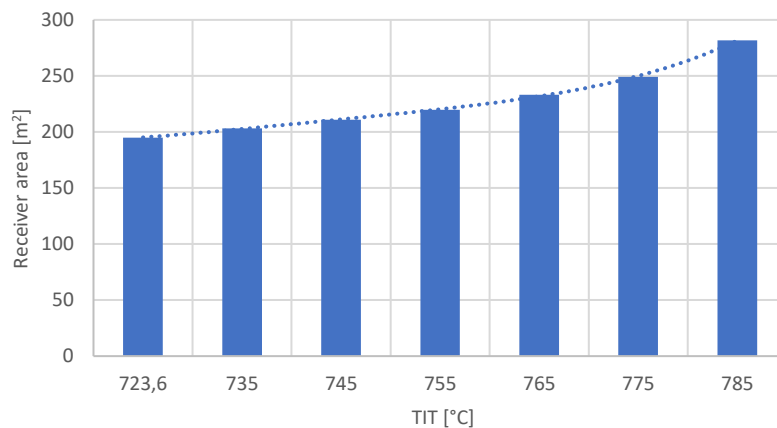
Figure 4.16 Receiver area varying the TIT

Even if the maximum surface temperature is the same and despite incident power decreases with TIT, in each layout the average surface temperature increases with the TIT affecting negatively the thermal efficiency, indeed the temperature difference between the receiver and the ambient increases and so the specific thermal losses. Moreover a larger surface area coupled with increased specific heat losses results in higher overall convective and radiative losses, penalizing receiver thermal efficiency, which decreases more than linearly with turbine inlet temperature (Figure 4.18).

The solar field optical efficiency (Figure 4.19) is influenced majorly from the increasing dimensions of the receiver, indeed, since the solar field has to ensure an almost constant power input, the number of rays deflected from the heliostats to the receiver are the same, although they are directed on a bigger area, therefore it is less likely that they miss the target.

The total solar to electric efficiency (Figure 4.20) is an indicator for the performances in design condition of the overall plant, with this analysis it can be demonstrated that, for a sodium receiver coupled with a recompressed intercooled sCO_2 Brayton cycle, the optimal efficiency is reached for very high temperatures, higher than the range studied, which is already very high with respect to studies found in literature.
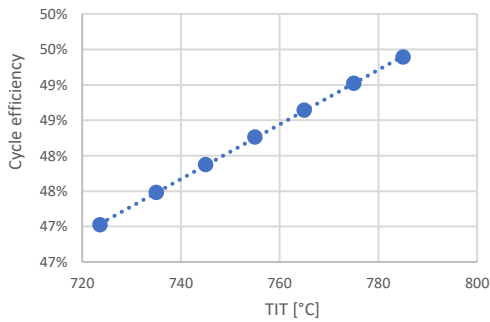
Figure 4.17 Power block efficiency varying the turbine inlet temperature (TIT)
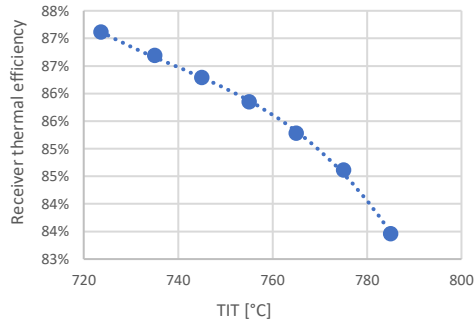
Figure 4.18 receiver thermal efficiency varying the TIT
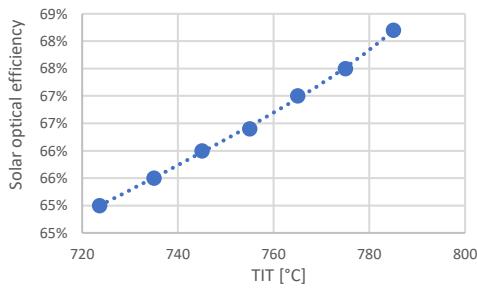
Figure 4.19 Solar field optical efficiency varying the TIT
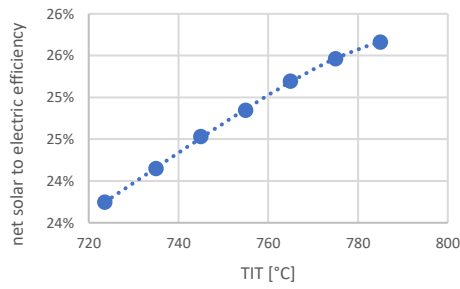
Figure 4.20 Net solar to electric efficiency varying the TIT

5 Ultimate design

In this chapter the assumptions made in the preliminary design and the feasibility of components design are verified in an industrial context A deeper research of the technical limitations has been conducted through a detailed literature review and with the help of industrial experts in the area of turbomachines, receivers and heat exchangers. The ultimate design considers the results of this research in order to represent a system which is compliant with limitations imposed by the industry.

5.1 Technical limits

This thesis work aimed at investigating real technical limits of the plant designed. Collaborations with manufacturing companies such as Franco Tosi Meccanica, AC Boilers and Alpha Laval was precious in order to find reliable information, where it wasn't possible to have direct contacts with the manufacturing companies, literature research focused on industrial articles.

5.1.1 Receiver

The panel design should be established by considering the action of internal pressure, deadweight, eigen-vibrations, wind, seismic, and thermal loads. In this study only internal pressure and thermal loads were considered, since a detailed 3-D structural analysis is out of the scope of the work, although a finite element analysis considering all these aspects would be necessary in the case of construction of the plant.

The mechanical design of the receiver panels defines the temperature limits and, consequently, the heat flux limits on the receiver surface. Some of the receiver limitations were already considered in the preliminary design, in particular temperature and stress limitations of the receiver material and temperature and velocity of the HTF in the pipes. In the previous analysis, however, the maximum creep stress and the maximum strain due to the low cycle fatigue where considered separately. In the analysis, stresses due to internal pressure (membrane stresses) and thermal stresses due to the hampered axial deflection of the receiver tube have been considered separately due to the different nature of the two stresses. In practical design, though, the damage due to creep and the damage due to low cycle fatigue combine into a cumulated damage which reduces the life of the component.

Babcock and Wilcox company describe in its text [20] the design procedure of all parts of a molten salt CSP plant. According to this text stress due to pressure and deadweight should be smaller than the allowable stress, defined as yield stress divided by 1.5. Since in this work deadweight is not considered, a security factor of 2 has been considered.

Babcock and Wilcox [20]suggests a simplified procedure to calculate axial stress due to the bending moment resulting from differently irradiated tubes. The axial stress induced by bending must be lower than 3 times the allowable stress, meaning approximately 2 times the yield stress. This procedure leads to the formula for the calculation of axial strains due to thermal stresses already used in previous calculations (Eq. 4.4).

In order to account for the creep effect, the pressure membrane stress must be lower than the stress which produces in the material 1% creep strain at 871°C temperature, after 91'250 hours (10h/day, 365 days/year, 25 years). The pressure membrane stress has been also compared to the maximum allowable stress in creep condition given by ASME code Section II, part D.

The strain due to thermal stresses interacts with low cycle fatigue behaviour of the material, therefore the thermal strain must be lower than the strain which induces creep initiation after 18'250 cycles (2 cycles per day, 365 days per year, 25 years) at 871°C temperature.

Finally, the cumulated damage due to creep and low cycle fatigue has been considered, since the two damage mechanisms interact further reducing the life of the component. The most common approach is based on linear superposition of fatigue and creep damage [79].

$$\sum \frac{N}{Nf} + \sum \frac{t}{t_r} = D < 1 \qquad \text{\textit{Eq. 5.1}}$$

where N/N_f is the cyclic portion of the life fraction, in which N is the number of cycles experienced by the component, N_f is the fatigue life at a given strain range and temperature, and t/t_r is the time-dependent creep-life fraction, where t is the time at a given stress and temperature, and t_r the time to 1% creep at that stress and temperature. The cumulated damage must be lower than 1.

Maximum membrane stress due to pressure experienced by the receiver tubes (Mariotte)	Yield stress of Haynes 230 at 871°C divided by 1.5 (Babcock and Wilcox company [21])	Maximum allowable creep stress taken from Haynes 230 datasheet at 871°C for a time of 91250 h	Maximum allowable creep stress for Haynes 230 at 875°C given in ASME section II, part D
9.58 MPa	157.33 MPa	19.19 MPa	13.8 MPa
Maximum thermal stress due to uneven irradiation on the tube surface (Babcock and Wilcox company [21])		Yield stress of Haynes 230 at 871°C multiplied by 2 (Babcock and Wilcox company [21])	
448.57 MPa		472 MPa	
Maximum thermal strain due to uneven irradiation on the tube surface (Babcock and Wilcox company [21])		Maximum allowable strain to have creep initiation due to low cycle fatigue at 871°C after 18250 cycles	
0.282%		0.357%	

Table 5.1 Creep and fatigue verifications

N	N_f	t	t_r	N/N_f	t/t_r	Cumulated Damage
18250 cycles	131072 cycles	91250 h	1015884 h	0.139	0.090	0.229< 1

Table 5.2 Cumulated damage verification

5.1.2 Heat exchangers

Heat exchangers are critical components of sCO$_2$ cycles because they have to operate under high temperature and pressure conditions. Heat exchangers operating in these conditions are subject to unique material challenges such as creep, reduced strength at higher temperatures, oxidation of material, corrosion, and thermal shock. As a result, expensive alloys that maintain their strength at elevated temperatures are usually the material of choice. However, these alloys typically have low thermal conductivity, and difficult manufacturability, and thus they present their own challenges in heat exchanger design and fabrication [80]. Moreover, these alloys have very high costs, which, combined with high thicknesses and volumes of the heat exchangers, make the cost prohibitive. Sunden [81] and Zhang et al. [80] are in agreement when saying that heat exchanger cost increases significantly with temperature above about 600-675°C.

As a result, there has been increased interest in Printed Circuit Heat Exchangers, which have reduced amount of material needed, due to the higher surface area to volume ratio, and thus lower cost. In this work, PCHE were previously considered for all heat exchangers present in the power block, although the manufacturing and operation of the Primary heat exchanger can present some critical aspects.

First of all, there are no presently manufactured PCHE which can sustain the operative conditions studied in this work. Indeed, Heatric, an Australian company manufacturing Printed Circuit Heat Exchangers since 1985, produce HX with the limitation presented in the graph in Figure 5.1.
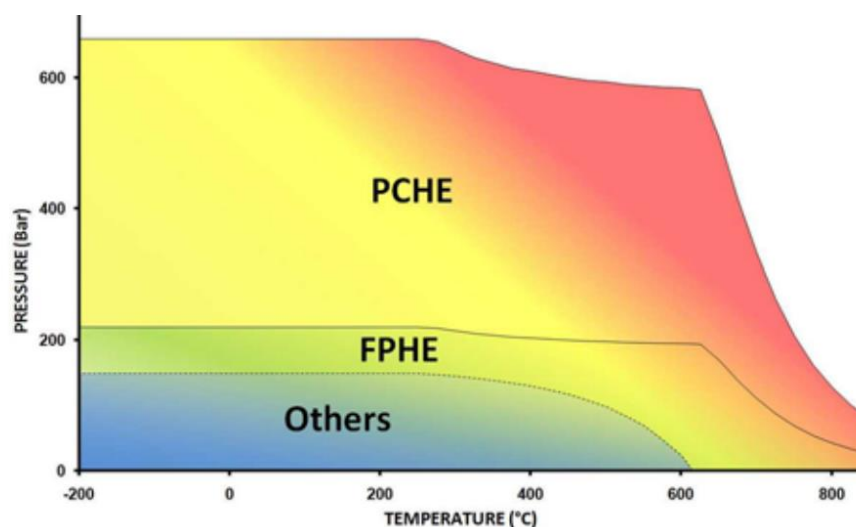
Figure 5.1 Heatric PCHE pressure and temperature limitations [22]

It is important to attain to limitations directly reported by manufacturing companies, indeed many papers have been written with various, often contradictory, claims about PCHE performance which ignore the impact of mechanical design issues on the design of PCHEs. For this reason Le Pierres et al., Heatric engineers promulgated the article [22], to clarify and correct these claims. From this graph (Figure 5.1) it can be extrapolated that for a pressure of 250 bar the limit temperature is below 650°C.

For this work also a direct contact with another PCHE manufacturing company was established, Alpha Laval, although this company only produce PCHE in stainless steel and therefore they can be manufactured only up to about 400°C.

A problem which could arise even if temperature and pressure conditions were below the limits of Heatric HXs is that, in printed circuit heat exchangers, both fluids pass in very small channels (hydraulic diameter is in the order of 1 mm), which can be easily clogged by solidified particles of sodium [82]. For this reason, Heatric in the article [83] suggests the use of hybrid heat exchangers (H^2X) in Figure 5.4, which are a combination of a Finned Plate Heat Exchanger (FPHE) in Figure 5.3 and a Printed Circuit Heat Exchanger (PCHE) in Figure 5.2.

Figure 5.2 Section of a PCHE (cross-flow) [83]

Figure 5.3 Section of a FPHE (cross-flow) [83]

Figure 5.4 section of a H^2X (counter-flow) [83]

These HX are formed from alternating layers of PCHEs, which are etched plates, and of FPHEs, which consist of fins (see fig. 3) bound by side bars and separated by flat parting sheets. With H^2Xs the sodium side can be selected to have a formed surface of larger hydraulic mean diameter although these types of HX have lower mechanical properties than PCHE and thus cannot sustain such high temperature and pressures.

Due to these limitations, the primary heat exchanger design was changed to a shell and tube HX, whose manufacturability was verified with Alpha Laval. The cost of this HX could be very high since it has a low heat exchange surface to volume ratio, moreover the high pressure design requires increased tube thicknesses and thus more costly material. For this reason a techno-economic analysis considering the price of this component should be performed in order to assess the convenience of increasing temperature and pressure above H^2X limits.

5.1.3 Turbine

The author has taken advantage of the cooperation with Franco Tosi Meccanica for the turbomachinery feasibility study. Franco Tosi, today Franco Tosi Meccanica (FTM) based in Legnano, is one of the most ancient power OEMs in Europe and today leverages on its proprietary state-of-the art technology in steam turbines to extend its design and manufacturing capabilities to sCO_2 field.

In its previous studies [23], FTM states that higher efficiency CO_2 cycles, which could be competitive on the market, can be obtained for TIT higher than 600 °C, up to about 700°C-750°C in case of closed cycles. Indeed, according the technology assessment carried out by FTM (and other technology leading OEMs, such as GE [84] and TOSHIBA [85]), in the range from 600°C to 700 and up to 720°C the sCO_2 development can rely on steam USC technology base, taking advantage of specific design features from gas turbine materials and cooling expertise. Further cycle maximum temperatures increase can, at the current state of the art, introduce important uncertainties on the technical-economical feasibility, since the cost reduction related to the power block weight reduction and the power loop simplification can be easily compensated from the need of high temperature strength materials, especially if very high pressure level are requested for the cycle efficiency optimization.

Above 750°C the oxy-combustion semi-closed cycle can be preferable from the techno-economic point of view. This approach is followed in the Allam cycle, to reach mainly two goals: the complete CO_2 capture and to reach higher efficiencies targeting temperatures as high as 1200°C, with a different thermodynamic scheme. These high temperatures are possible since the heat source acts directly within the power loop thanks to an oxy-combustion chamber connected to the turbine casing with an arrangement that is a good exemplification of how gas and steam turbine technology features combine together in the sCO_2 design.

The first prototype of the Allam cycle was built by Net Power, a 50 MWth natural gas demonstration power plant in La Porte, Texas [86]. Its turbine, manufactured by Toshiba, has

inlet temperature of 1150°C [85] making it the hottest CO_2 turbine ever manufactured. In their article Sasaki et al. [85], Toshiba engineers, explain some issues rising from the operation at such high temperatures which have been addressed in the manufacturing of these kind of turbines. Statements made by Toshiba in the article are in accordance with the information provided to the author from Franco Tosi Meccanica.

5.1.3.1 Material selection and limits

Even if the materials used to manufacture the turbine components seem to be subject to lower temperatures when compared to cutting-edge-technology in aeroderivative and heavy-duty gas turbines, few important considerations must be pointed out.

To meet minimum cost requirements of the power loop, main turbine parts such as the rotor, shall allow an operational life of not less than 80 kh; this is mainly due to the need of reducing the overall average time of outage, that can represent a major OPEX cost item. Accordingly, for the shaft, mainly, and the inner casing secondarily, an advanced Nickel - low Cobalt alloy can be selected, once detailed analysis of material thermal expansion coefficient and related structural issues has been carried out. Furtherly, it is important to point out as well that massive parts such as rotor shafts and disks in gas turbine and aero-engines don't experience higher temperatures than the ones foreseen for above 700°C sCO_2 turbine shafts, since in those applications the huge cooling air flow is conveyed towards the most massive engine parts, that are consequently kept at similar temperatures levels; in the case of sCO_2 machinery, as well as in steam turbines, a similar amount of cooling flow isn't allowable. On the other side, blading design can be carried out based on more severe creep conditions, since a shorter expected life (approximatively one third or half of the shaft lifetime) can be feasible if proper maintenance strategies are actuated. Moreover, alloys with higher creep resistances can be employed for the manufacturing of the blading, at least for the first stages, without affecting in a dramatic way the economics of the power block.

Even if sCO_2 machinery is much smaller if compared to steam or gas units of similar power, some components can be large enough to require a technological assessment of the forgings and manufacturing processes involving alloys containing high Ni – Co fractions. It will be especially important for future 100 MWel size turbines, before they enter the market. At least in the first development stage, to stick to A-USC materials studies could be of great help [85].

Many works such as [87] and [88] indicate which materials are suitable for the construction of high temperature parts of USC steam turbines, which have temperature and pressure conditions comparable with sCO_2 cycles.

In Table 3.5

Alloy	Potential applications for [88]	Potential applications for [87]
N06230	SH/RH, Pipes	Pipes

N06617	SH/RH, pipes (CCA 617)	Casing, rotor (IN 617)
Inconel 740	SH/RH, pipes (and 740H)	Casings, pipes
Haynes 282	Casings, Rotor	Casings, Pipes
N07263	Casings, Rotor (Alloy 263)	Casings (C 263)

Nickel-based alloys under evaluation both in [88] and [87] for the manufacturing of USC cycles components are reported, each material combined with its possible applications. No blades materials were evaluated from both references, Waspalloy and Nimonic 105 were advised in [88], while Inconel 100 in [87].

Alloy	Potential applications for [88]	Potential applications for [87]
N06230	SH/RH, Pipes	Pipes
N06617	SH/RH, pipes (CCA 617)	Casing, rotor (IN 617)
Inconel 740	SH/RH, pipes (and 740H)	Casings, pipes
Haynes 282	Casings, Rotor	Casings, Pipes
N07263	Casings, Rotor (Alloy 263)	Casings (C 263)

Table 5.3 Nickel based alloys under evaluation in [87], [88] *for USC applications*

As it was introduced before, blades can sustain higher temperatures than rotor disks due to their smaller size which allow the use of materials with higher high-temperature strength. Moreover, blades need to resist for a shorter time with respect to the rotor because they can be substituted before the end of the turbine lifetime. Rotors, instead, need to be forged, therefore materials must be more ductile and consequently less resistant to high temperature stresses.

In this work, according to a techno-economic study performed by FTM [23], a limit temperature of 750°C was considered in order to avoid internal blade cooling. Instead maximum temperature of the rotor was calculated from N07263 creep properties with the Larson miller extrapolation using the criteria of 100'000 h strength at 100MPa [88] and the calculated limit temperature is 725°C.

5.1.3.2 Turbine cooling

In order to raise the turbine inlet temperature over these values, with the aim to increase the efficiency of the cycle, some parts of the turbine should be cooled. To avoid the need of film cooling and internal convection cooling of the turbine blading the inlet turbine temperature must be lowered to 750°C. Although, at this temperature cooling of the rotor and rotor disks must still be performed.

The cooling fluid is injected in a cavity between a liner below the first stator and the rotor body. This liner is specifically realized to protect the rotor from the hot main flow. The cooling flow will then be discharged downstream the first stator ending its refrigerating action on the base of the first rotor blades.
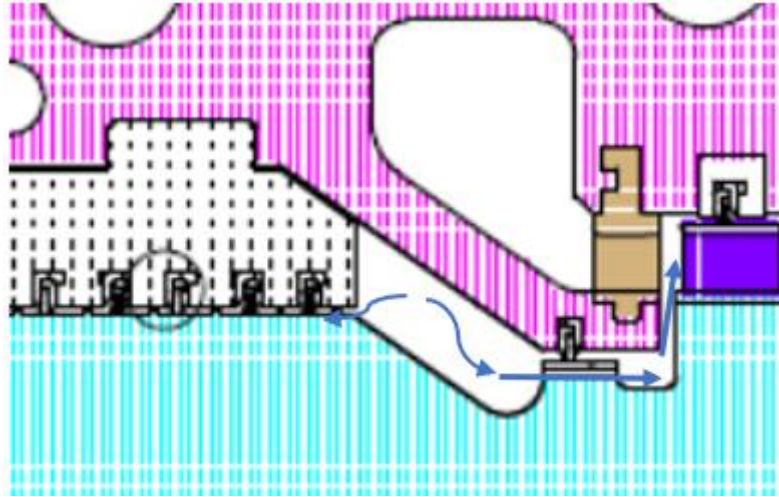
Figure 5.5 Cooling flow pattern scheme (property of FTM)

The extraction point of the cooling medium from the thermal cycle must be chosen depending on both its temperature and pressure. Pressure must be high enough to allow the injection downstream the first stator, considering pressure losses on the cooling fluid line and the necessity to avoid leakages of the hot working fluid in the refrigerant, which would cause a power loss and a decrease of the refrigerating efficacy of the cooling fluid.

Depending on the inlet temperature of the cooling medium the mass flow rate required changes, namely with a colder fluid a lower mass flow rate is needed, although it is important to avoid using a too cold fluid to prevent the material from experiencing high thermal gradients. For these reasons the output of the second regenerator was preliminarily chosen as the refrigerant extraction point, even if the pressure margin is given just by the pressure drops in the Primary Heat Exchanger.

5.1.3.3 Effectiveness of the cooling process

In order to allow an efficient refrigeration of the rotor body the convective heat transfer coefficient must be high. A brief analysis of the Nusselt numbers obtainable on the designed turbine with various mass flow rates was performed in this work, using Reynolds estimation and Nusselt correlations suggested by Franco Tosi Meccanica, these are used in the cooling design of steam and high-density-flow turbines.

CO_2 turbines are very similar to the high-pressure stages of steam turbines. There are many correlations for the calculation of the Nusselt number, in the conditions typical of convective heat transfer on steam turbine rotors. Most of them are variations of the Dittus Boelter correlation. A frequently used ones is the Gazley correlation [23]:

$$Nu = 0.023 \, Re_{u+v}{}^{0.8} \, Pr^{0.4}$$

<div align="right">Eq. 5.2</div>

For CO_2, Franco Tosi Meccanica studied a specific correlation validated through CFD simulations:

$$Nu = 0.0265 \, Re_{u+v}{}^{0.8} \, Pr^{0.4}$$

<div align="right">Eq. 5.3</div>

Reynolds number are calculated on the relative velocity referring to the combined effect of the mean peripheral velocity of the rotor and the axial velocity of the fluid, assuming the mean peripheral velocity in the boundary layer as half of the superficial tangential velocity of the rotor.

$$Re_{u+v} = \frac{\rho \, \delta}{\mu} \left[\left(\frac{\omega \, D_i}{4} \right)^2 + \left(\frac{\dot{M}}{A \, \rho} \right)^2 \right]^{0.5}$$

<div align="right">Eq. 5.4</div>

Where:

δ is the gap between liner and rotor

$\dot{M}$ is the mass flow rate of cooling fluid

A is the cooling fluid flow area (between the liner and the rotor)

ω is the rotational speed of the rotor

The heat transfer coefficient can then be computed as:

$$h = \frac{Nu * k}{\delta}$$

<div align="right">Eq. 5.5</div>

For the calculation of the Nusselt number the geometrical parameters reported in Table 5.4 have been considered, these values come from the turbine layout definition. The cooling fluid inlet temperature is the discharge temperature of the second regenerator, for the TIT 750°C case, 554.4°C.

δ	[m]	0.002
Rotor rotational speed	[rpm]	4600
Do	[m]	0.5
Di	[m]	0.496
A	[m²]	$= (Do^2 - Di^2) * \dfrac{\pi}{4}$

Table 5.4 Nusselt number calculation geometrical parameters

From the analysis (Figure 5.6) it is possible to deduce that an effective refrigeration of the turbine rotor is possible also in case of CO_2 because heat transfer coefficients are very high also

for low mass flow rates. These values are higher than usual heat transfer coefficients in steam turbines for a few reasons:

- Being smaller, CO_2 turbines have a higher optimal rotational speed, the increase of rotational speed compensate the smaller diameter influence on the mean peripheral velocity in the boundary layer, therefore peripheral velocities are comparable on the two turbine designs.
- The density of CO_2 at these temperature and pressures is much higher than the one of steam (118.6 kg/m^3 of CO_2 compared to 50- 60 kg/m^3 of steam in typical applications) increasing the Reynolds number.
- A minor effect is also given by the smaller flow area (A) due to reduced rotor diameters.
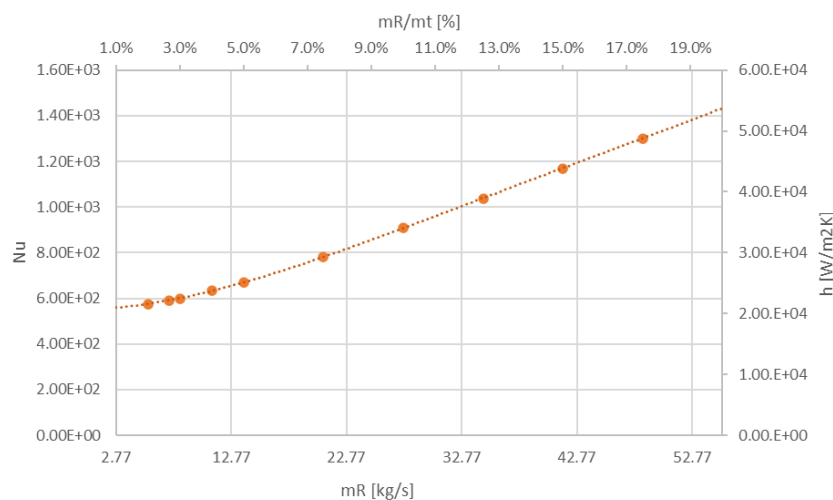
Figure 5.6 Convective heat transfer coefficient between rotor and cooling fluid varying the cooling fluid mass flow rate

5.1.3.4 Efficiency loss due to refrigeration

The cooling mass flow rate ($\dot{m}_c$) is extracted at the end of the second regenerator and then injected at the end of the first stator of the turbine, therefore this portion of the total mass flow rate ($\dot{m}_t$) is neither heated in the PHX nor expanded in the first stage, the mass flow rate expanded in the first stage will hence be:

$$\dot{m}_t - \dot{m}_c$$

Eq. 5.6

While from the second stage the mass flow rate will be the total one and the inlet enthalpy will be the product of the mixing between cooling fluid and main flow.

Pressure at the inlet of the first stage will be reduced due to the difference between the working fluid mass flow rate being expanded in the first stage and the total mass flow rate in case of no refrigeration.

112

Considering, as a good approximation, the blading efficiency (η_{blades}) unchanged [23], the effective power produced can be calculated as:

$$P_C = \eta_{comp}\eta_{blades}[(\dot{m}_t - \dot{m}_c)\Delta h_{is\,I} + \dot{m}_t\,\Delta h_{is\,II-Last}]$$

<div align="right">Eq. 5.7</div>

Where η_{comp} is the compensator efficiency, η_{blades} the group blading efficiency, $\Delta h_{is\,I}$ is the isentropic enthalpic step on the first stage and $\Delta h_{is\,II-Last}$ the overall one on the other stages.

The ratio between the refrigerated turbine power and the non-refrigerated one is:

$$\varepsilon_C = \frac{P_C}{P}$$

<div align="right">Eq. 5.8</div>

If the temperature conditions at the inlet and outlet of the PHX are unchanged, the ratio between the inlet thermal power in the refrigerated turbine cycle and the one on a non-refrigerated turbine can be defined as in Eq. 5.9.

$$\alpha_{th} = \frac{\dot{m}_t - \dot{m}_c}{\dot{m}_t}$$

<div align="right">Eq. 5.9</div>

The efficiency of the cooled turbine cycle can be hence calculated as a function of the non-cooled one (Eq. 5.10).

$$\eta_C = \frac{P_C}{P_{th\,C}} = \frac{\varepsilon_C\,P}{\alpha_{th}\,P_{th}} = \frac{\varepsilon_P}{\alpha_{th}}\,\eta$$

<div align="right">Eq. 5.10</div>

In Figure 5.7 the efficiency reduction of the cooled cycle with TIT 750°C at different cooling mass flow rates is compared with the efficiency of a non-cooled one with TIT 725°C.
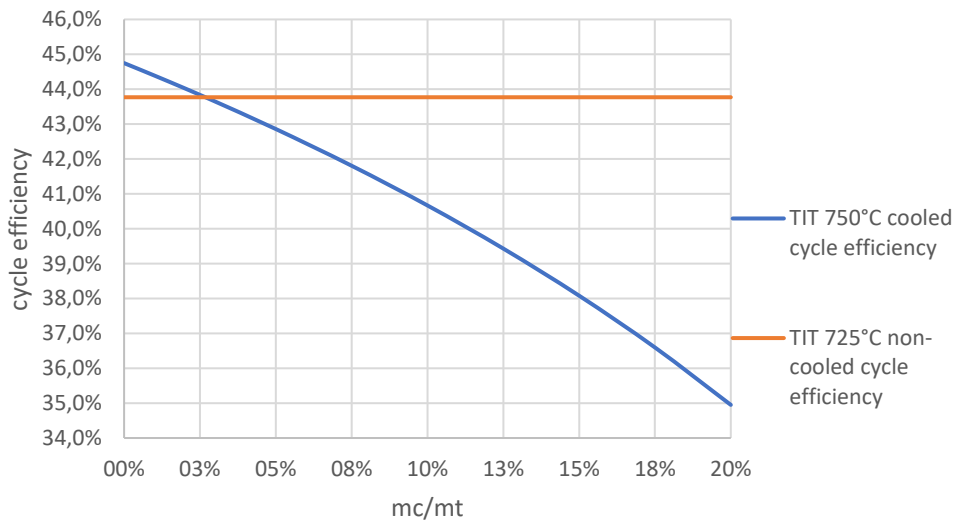
Figure 5.7 Efficiency variation of the TIT 750°C cooled cycle compared to the TIT 725°C non-cooled cycle

Only up to a cooling mass flow rate which is 2.66% of the total one it is convenient to increase the turbine inlet temperature up to 750°C (maximum temperature to avoid blade refrigeration) and refrigerate the turbine rotor. If, instead, the required mass flow rate is higher that this percentage, it is more convenient to decrease the inlet turbine temperature down to 725°C.

Since this percentage is very low and it is difficult to determine with precision the mass flow rate needed to cool the rotor material down to 725°C, without a detailed turbine design, in the ultimate design a non-cooled turbine with inlet temperature of 725°C was chosen.

5.1.3.5 Turbine feasibility design

The selection of radial or axial turbomachinery design is performed typically on the base of operating conditions, the most efficient configuration for the turbine and compressor transitions from radial to axial at approximately 30 MW and 100 MW, respectively [89]. Turbine in this work is in the range of 50 MW and an axial design was chosen. FTM performed actual 1-D calculations of the possible sCO_2 axial turbine blade design, results are shown in Table 12.1 and Table 12.2. These calculations were performed through the use of a FTM standard proprietary code, based on FTM standard profile performance curves, applied to CO_2 using NIST Refprop fluid proprieties tables. This code was obtained adjusting the 1 D steam HP/IP turbine section calculation code for CO_2. Due to the degree of confidence in this kind of calculations, the results presented in Table 12.1 and Table 12.2 can be considered highly reliable.

Two different preliminary blading paths are investigated; one full 50% reaction degree, full arc, ten stages, and a second one with variable reaction degree, full arc, seven stages configuration. The adoption of a variable degree of reaction design allows to reduce the number of stages and to reduce the outlet temperature of the first stages which are more loaded, making it possible to use lower grade materials for the last stages and to reduce the overall cost of the turbine. This solution, although, has a lower efficiency (92.26% of blading efficiency compared to 93.19% of the 0.5 degree of reaction case), due to the higher loading of the first stages. In the next calculations the design considered is the most efficient one since cost has not been taken into account in this analysis. Calculation tables with the detailed results (Table 12.1 and Table 12.2) can be found in Appendix E, while an extract is reported below in Table 5.5.

	1° stage	2° stage	3° stage	4° stage	5° stage	6° stage	7° stage	8° stage	9° stage	10° stage
Degree of reaction	0.5	0.5	0.5	0.5	0.5	0.5	0.5	0.5	0.5	0.5
	0.35	0.37	0.4	0.44	0.5	0.5	0.5			
Stage outlet temp [°C]	710.8	697.1	683.1	668.8	654.3	639.6	624.4	609.0	593.2	577.1
	702.3	683.5	664.1	644.2	622.1	600.4	578.0			
Stator eff	0.9505	0.9493	0.9511	0.9497	0.9493	0.9500	0.9512	0.9506	0.9530	0.9508
	0.9513	0.9511	0.9447	0.9463	0.9485	0.9555	0.9546			
Rotor eff	0.9482	0.9490	0.9486	0.9494	0.9489	0.9514	0.9506	0.9522	0.9524	0.9493
	0.9194	0.9323	0.9370	0.9442	0.9458	0.9490	0.9490			

The efficiencies reported in the calculations tables are the bladed group isentropic and volumetric efficiencies, the first one takes into account all the efficiency loss mechanisms: blading fluid-dynamic losses, blade leakage losses and friction losses of the rotoric parts of the turbine. It has been considered to adopt brush type seals for the blading and for the thrust balancing piston, brush seals consist of fine diameter fibres densely packed between two plates, a support plate that is called as "backing ring" or "backing plate" is positioned downstream of the bristles to provide mechanical support for the differential pressure loads [90] (Figure 5.8). This type of seals allows a lower compensation loss meaning a smaller leakage flux flowing through the seals, the leakage flow (about 1% of the entire mass flow rate) was considered in the energy balance subtracting it by the mass expanding in the turbine and considering a mixing at the turbine outlet.
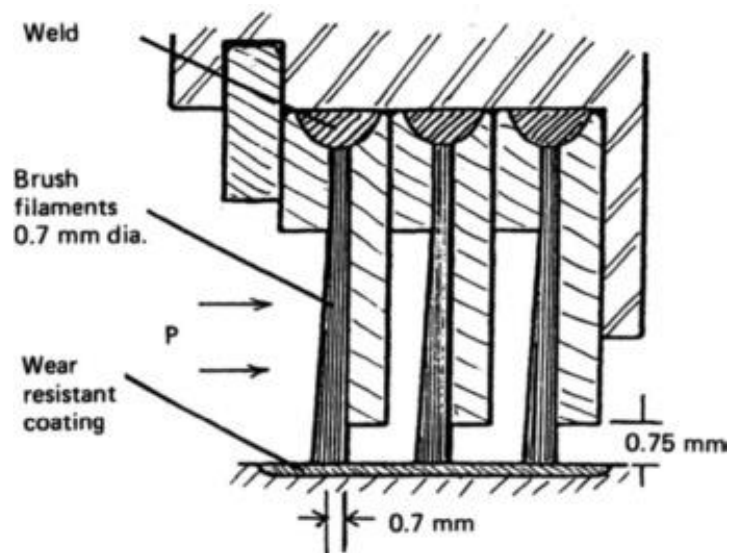
Figure 5.8 Brush seals [91]

115

A typical five stage, 650°C / 200 bar inlet conditions, FTM sCO$_2$ turbine simplified sectional drawing is reported in Figure 5.9.
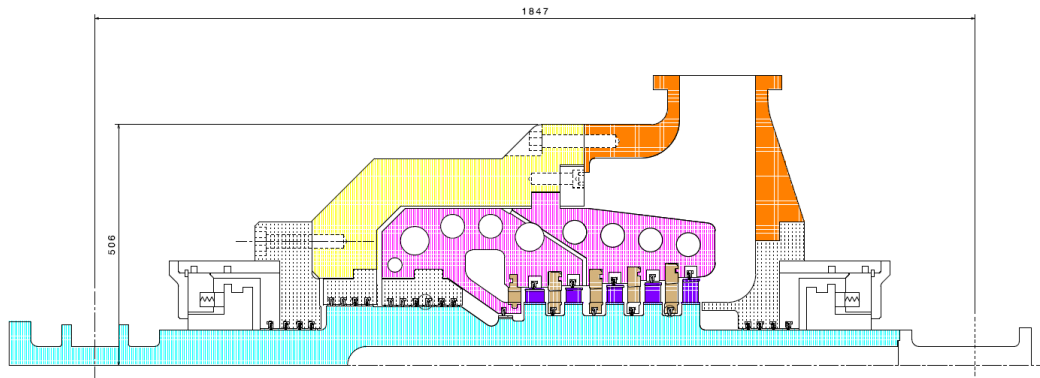
Figure 5.9 Franco Tosi meccanica (FTM) 25 MW class 650°C sCO$_2$ turbine

5.1.4 Compressors

As turbines, also sCO$_2$ compressors feature small overall dimensions, this is due to very high fluid density [89]. One of the most important advantages of sCO$_2$ Brayton cycles is the possibility to have the compressor operating near critical conditions, taking advantage of the high density of the fluid, so that the compression work can theoretically be reduced to values comparable to those of liquid compression of a Rankine cycle. For this reason, at most scales (below 100 MW [89],[92]), the compressors in sCO$_2$ turbomachinery designs are centrifugal, thanks to their lower volume flow and lower susceptibility to varying inlet conditions [93].

Compression in condition very close to fluid critical ones is anyway challenging, since small deviations in pressure and, mainly, in temperature, can cause huge variation in fluid density, with the possibility of heavy off design operating conditions for the compressor that can even result in surge arising. The design of the compressor and of the power cycle must take into account this aspect, which is strongly related to ambient conditions and their variation.

Another problem caused by operation very close to the critical conditions can be the condensation of part of the working fluid creating a mixture of vapor and liquid droplets, this is due to pressure reduction at the compressor. Transient behaviour of the flow may cause serious issues in operation of the cycle and degrade the materials used in the design, this problem is studied by Ranjan in [94].

To avoid these problems, it is good practice to maintain some margin from the saturation dome in the design process.

Due to high ambient temperature and dry cooling of CSP plant, design working conditions are far enough from the critical point to avoid these issues, problems can arise during off design

conditions. It is, therefore, advisable the operation with constant inlet temperature of 52°C and varying HRUs power since compressor efficiency is very negatively affected from partial load operation.

A simple dimensioning of the one stage radial compressors was developed with the aid of FTM in order to primarily assess compressors mean diameter and rotational speed.

Defining the compressor specific speed and the specific diameter as respectively in Eq. 5.11 and Eq. 5.12.

$$\omega_s = \omega \frac{\sqrt{\dot{Q}_{in}}}{\Delta h_{is}^{0.75}}$$

Eq. 5.11

$$D_s = D \frac{\Delta h_{is}^{0.25}}{\sqrt{\dot{Q}_{in}}}$$

Eq. 5.12

The Balje diagram specific for radial one stage compressors can indicate optimal specific rotational speed and specific diameter in order to obtain high compressor efficiency and good operational flexibility. In Figure 5.10 an extract from the Balje diagram, found in the article of Pesatori et al. [95], showing compressor efficiency in relation to the specific speed and optimal specific diameter in relation to the specific speed. Form this graph it is possible to asses that if the compressor is well designed 85% efficiency is reachable, and that specific speed must be between 0.7 and 2 in order to ensure good compressor efficiency and flexibility, indeed efficiency doesn't decrease abruptly if inlet volumetric flow rate varies slightly. These values of specific speed correspond to specific diameter in the range 2.5-4 approximately.
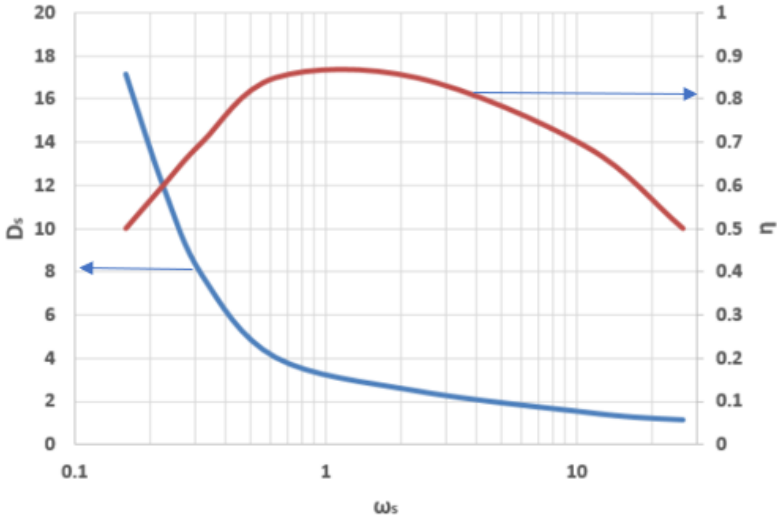
Figure 5.10 Extract from the Balje diagram, compressor efficiency over specific speed (red line) and optimal specific diameter over specific speed [95]

Table 5.6 shows calculations for the sizing of the three compressors. All the compressor's optimal speeds are much higher than the turbine optimal one, either a specifically designed gear box, or an electrical high-speed compressors drive system must be employed.

		Main Compressor 1	Main compressor 2	Recompressor
mass flow rate	kg/s	195.99	195.99	93.07
pressure	Mpa	8.07	11.20	8.24
temperature	°C	52.0	52.0	106.5
density	kg/m3	216.1	484.3	141.4
volumetric mass flow rate at the inlet	m3/s	0.907	0.405	0.658
$\Delta h_{isentropic}$	J/kg	13671	25130	76926
$\omega_{optimal}$	-	1.0	1.0	0.64
$\omega_{theoretical}$	rad/s	1328	3137	3644
$N_{theoretical}$	rpm	12679	29960	34797
N_{chosen}	rpm	13000.0	30000.0	35000.0
ω	rad/s	1361.4	3141.6	3665.2
ωs	-	1.0	1.0	0.64
$Ds_{optimal}$	-	3.2	3.2	4
D	m	0.282	0.162	0.195

Table 5.6 Compressor sizing calculations

Initially the optimal specific speed of 1 was assumed for each compressor, although it resulted in a rotational speed of almost 55'000 rpm for the recompressor. This speed is too high and can cause issues related to centrifugal stresses, therefore specific speed was lowered to 0.64, which allows to keep rotational speed below 35'000 rpm.

Since optimal rotational speed of the three compressors are very different, a different configuration of the turbine and compressors coupling could be considered, with the main compressor directly driven by the main turbine through gear boxes, while the recompressor, which must rotate at much higher speed, coupled with a booster turbine expanding sCO2 coming from a bleeding in the main turbine, as suggested in the work of Pesatori et al. [95].

5.1.5 Sodium related attentions

The design of a sodium plant has some peculiarities which are needed in order to ensure a safe operation. The sodium heat transfer circuit is designed as a single-circuit system (no intermediate heat exchanger, the HTF is also the storage fluid) and it includes one loop for the receiver and another for the PHX. Both parts of the system are hydraulically independent of each other, the open connection being provided only by the two storage vessels. Both loops are filled with liquid sodium and, differently from molten salt systems, an inert gas (usually argon). It is, indeed, not possible to have an open system where an air tank is pressurized and depressurized to control pressure inside the receiver system, due to sodium reactivity with air. For this reason, a cover gas system which supplies pressurized argon to the whole heat transfer

system is necessary. Furthermore, a sodium purification system is used in order to ensure high sodium purity to avoid operational difficulties [39].

For the same safety reason a sodium leak-collecting cavity is situated below all parts of the heat transfer systems, including the storage vessels [96]. As for the molten salt system tracing is needed, since solidification temperature of sodium is higher than the ambient temperature, although installed power required should be lower since the solidification temperature is lower (90°C).

Specific attention must be given to the sodium pumps acting in the loops. Literature about liquid sodium pumps mostly refers to sodium cooled fast breeder nuclear reactors. In a fast breeder reactor, the liquid sodium coolant is circulated through the core using vertical centrifugal pumps. The rotor assembly (in Figure 5.11) consists of a shaft on one end of which is mounted the impeller immersed in sodium. The rotor assembly is supported inside sodium by means of a pocketed hydrostatic bearing that is supplied with high pressure sodium from the pump discharge. The free surface of sodium in the pump tank is topped by argon cover gas at a pressure slightly above atmospheric pressure [97]. The gas is sealed from the atmosphere using triple mechanical seals. Bearings and seals are lubricated ad cooled by a dedicated oil circuit. One of the potential issues of these pumps is oil leakage in the sodium circuit since the consequent clean-up of sodium from oil could result in long shutdowns of the plant. To eliminate this problem Sreedhar et al. [97] introduced a design variant that eliminates the use of oil in seals and bearings.

Another study by Chellapandi et al. [98] was performed to evaluate the lowering speed of the pump into the sodium vessel. Indeed, the pump, which before lowering it into the sodium vessel will be at ambient temperature, experience thermal stress due to the hot shock offered by the sodium. This paper addresses the thermo-mechanical analysis carried out towards establishing the preheating temperature and speed of lowering the pump in the sodium pool.

Many studies have been carried out one the use of electromagnetic (EM) pumps instead of mechanical pumps, e.g. Nasa report on liquid metal pumps technologies [99] or Ota et al. [100]. The adoption of EM pumps in sodium cooled nuclear reactors can be preferred when it is highly desirable to avoid wear issues, mechanically induced vibrations, and sealing difficulties associated with incorporating reciprocating or rotating machinery into a liquid-metal flow system [99].

An electromagnetic pump is a static equipment that circulates coolant sodium by electromagnetic force, utilizing Na as a good electric conductor. This type of pump has the potential to increase reliability and reduce plant cost for these four reasons:

- A free surface level of sodium in the pump is not necessary, meaning that the pump can be on the same plane of other pieces of equipment like HXs instead of being lifted, reducing the amount of material needed and construction cost.

- Since sodium can be circulated in fully confined condition, it is possible to decrease potential Na leakages.
- Auxiliaries (such as a reduction gear, a mechanical seal, a lubricating oil system, and an oil lifter) can be eliminated.
- Since it is static equipment which requires very few renewal parts or consumable parts, it is possible to improve its reliability and maintainability.
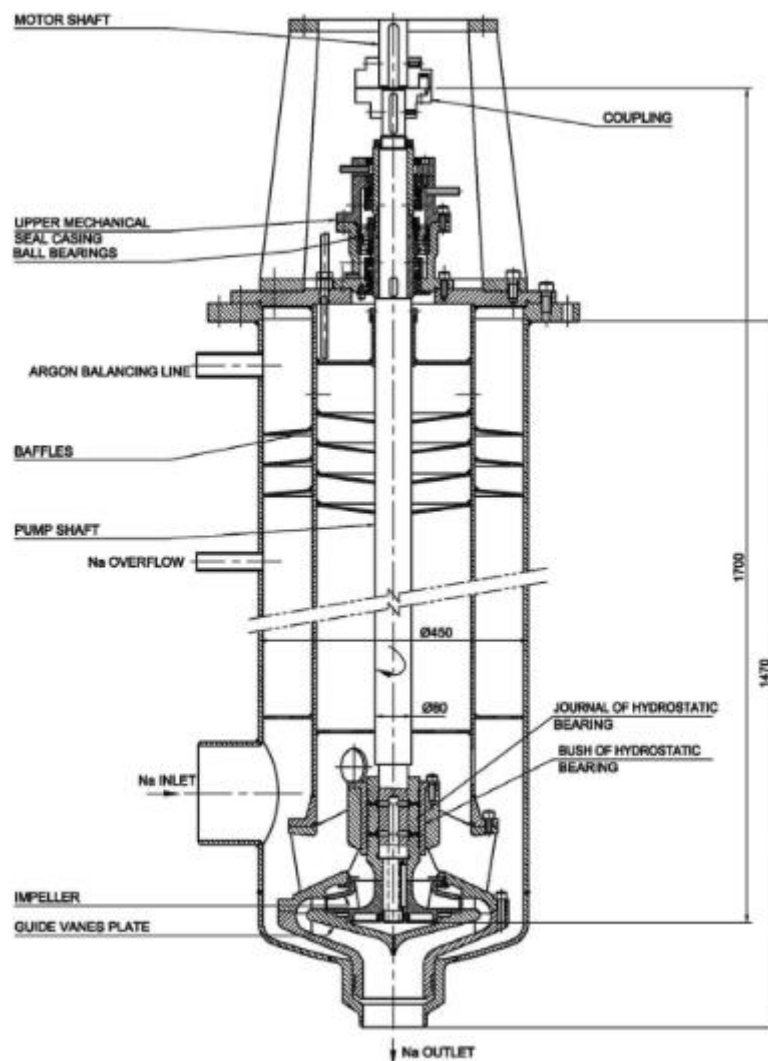
Figure 5.11 Mechanical drawing of a vertical centrifugal sodium pump [66]

Even if EM pumps have many advantages, they aren't used in most cases because their efficiencies range between 3% to maximum 50% [99], making them not competitive. For this

reason, a mechanical pump was considered in this work design, considering its realization possible. Although it has to be noted that all the cited studies consider lower temperature of operation, since fast breeder reactors work with a maximum HTF temperature in the range 400°C – 600°C [99]–[101]. Pump operation under very high temperature conditions could be critical, therefore testing of the pump in these conditions is advised.

5.1.6 Supercritical CO_2 corrosive behaviour

The use of sCO_2 Brayton cycles in place of equivalent steam cycles is also motivated from the corrosive behaviour of steam at very high temperatures. The adoption of sCO_2 can hinder this problem, although considerations on materials degradation due to interaction with sCO_2 at high temperature must be done.

Due to the increasing interest in sCO_2 cycles a few studies on compatibility of structural alloys with sCO_2 at high temperature have been conducted, Sandia National Laboratories conducted a study on sCO_2 corrosive and Erosive mechanisms [82] and Oak Ridge laboratories a study about compatibility of sCO_2 at high temperature with structural alloys [102]. From these studies emerged that systems working with pure sCO_2 only limitedly suffer corrosion and erosion issues, but that CO_2 purity is a very important aspect in the corrosion mechanism, since impurities can relate to the formation of corrosive acids. As reported in [82] it is expected an increase in the corrosion rates for higher temperature sCO_2 systems and for higher pressures, due to an increasing solubility of water in CO_2, which directly correlates to concentrations of carbonic acid. Therefore, further studies have been carried out from the two laboratories on the influence of impurities in SCO_2 corrosion mechanisms [103], [104], indeed even closed commercial sCO_2 systems may work with lower purity CO_2 (Industrial Grade CO_2, IG) compared to what is used in most laboratory experiments (Research grade CO_2, RG). Surprisingly both studies resulted in assessing that little differences are observed for RG CO_2 and IG CO_2.

Furthermore, results coming from Pint and Keiser [104] are unexpectedly reassuring, since nor high pressure or CO_2 impurities had a significant impact on oxidation. This article focuses on the influence of CO_2 purity on oxidation in very high temperature systems (750°C), considering in their analysis two different pressure values (1 bar and 300 bars) and several alloys. Pint and Keiser state: "In a few cases, pressure appeared to affect the results, particularly for the Fe-based alloys 25 and 310HCbN. However, in most cases, the difference between the 1 and 300 bar results was minimal. Likewise, only minimal differences were noted between IG and RG CO_2." Another important result, for the purpose of this work is that best corrosion performances were observed for the solid solution strengthened Ni-based alloys.

Carburization is another materials degradation concern in high temperature sCO_2 systems. Carburization is the formation of metal carbides in a material as a result of exposure to a carbon containing atmosphere. This corrosion process, referred to also as "Metal Dusting" results in

surface attack and the formation of a powdery residue, it can result in loss of mechanical properties over time in addition to wastage of the material.

Consequences of carburization are complex, if carbon uptake occurs too quickly, some of the carbon becomes trapped in the oxide scale, increasing porosity. Next, as carbon diffuses into the metal matrix, formation of chromium carbides occurs, effectively sensitizing the steel and increasing susceptibility to stress corrosion cracking.

Fleming an Kruizenga [82] state that carburization was found on the base alloy at temperatures as low as 550°C. Since carburization information on austenitic and nickel-based stainless steels is incomplete it only can be said that at high temperatures, carbon activity may have detrimental effects in terms of the stability of chromium carbides, which may reduce the corrosion resistance of austenitic alloys.

5.2 Design choices

The ultimate design was modified in accordance to the technical limitations reported in paragraph 5.1, design choices and results are reported in the following paragraphs.

5.2.1 Power block

The major limit of the power block is given by the maximum turbine inlet temperature, which was set to 725°C. This limit temperature is the one seen from the turbine rotor, therefore, considering an isenthalpic pressure loss on the turbine inlet valve of 0.02 $\left(\frac{\Delta P}{P}\right)$ and an isenthalpic pressure loss on the pipeline linking the PHX to the turbine of 0.15, the maximum temperature reached at the outlet of the PHX is 725.19°C. Efficiency of the turbine in the product of the blading efficiency (93.19%), resulting from the turbine design, and the compensator efficiency (99%), accounting for the flux leakage through the pressure compensation system. A mechanical power loss of 250 kW is accounted for the friction loss in bearings, while the efficiency of the gear box and generator were considered to be respectively 98.8% and 98.6%. These assumptions where advised by FTM.

Pressure losses assumptions aren't varied from the preliminary design, only the pressure loss on the piping line from the PHX to the turbine and the pressure loss on the turbine inlet control valve where accounted.

In order to ensure a constant minimum temperature of the cycle (52°C) in all power block working conditions, which depend from ambient temperature, the design of the heat rejection units was performed in the worst case, meaning with the highest ambient temperature measured on site, 45°C. This different design resulted in a higher HX area and higher nominal air mass flow rate, at lower ambient temperatures fan power is decreased, decreasing air mass flow rate, in order to keep the power exchanged constant.

Parameters and main results of the power block ultimate design are reported in Table 5.7, while the thermodynamic points of the cycle are reported in Table 5.8.

ΔP/P HP side of LTR	0.06%	Pmax	25.437 Mpa
ΔP/P LP side of LTR	1.50%	Pmin	8.073 Mpa
ΔP/P HP side of HTR	0.16%	Pmed	11.199 Mpa
ΔP/P LP side of HTR	1.50%	P at the outlet of the PHX	25 Mpa
ΔP/P PHX	1.50%	RPR	0.5910
ΔP/P precooler	2.00%	β turbine	2.9445
ΔP/P pipeline from PHX to Turbine	1.50%	mCO_2	289.06 kg/s
ΔP/P inlet control valve	2.00%	SR	0.6780
UA HT reg	4120.75 kW/K	Turbine Rotational speed	4600 rpm
UA LT reg	2817.18 kW/K	Compensator efficiency	99%
UA Precooler	816.30 kW/K	Blading efficiency	93.19%
UA intercooler	1466.44 kW/K	Total turbine efficiency	92.26%
ΔTmin LT/HT regenerator	12 °C	Bearings power loss	250 kW
ΔTmin air in precooler and intercooler	15°C	Gear box efficiency	98.8%
Design ambient temperature	35°C	generator efficiency	98.6%
Inlet thermal power	68006.6 kW		
Gross el power	31191.01 kW		
Aux (heat rejection)	162.53 kW		
Net el Power	31028.5 kW		
Cycle efficiency	45.63%		

Table 5.7 Power block ultimate design parameters and results

	mCO2 (kg/s)	P (Mpa)	T (C°)	h (kJ/kg)	s (kJ/kgK)	cp (kJ/kgK)	C (kW/K)
1	195.99	11.20	52.00	361.4	1.501	5.73	1123.30
2s	195.99	25.44	92.54	386.6	1.501	2.22	435.16
2	195.99	25.44	94.54	391.0	1.513	2.21	433.63
3 LT Reg	195.99	25.42	224.83	617.3	2.047	1.40	274.30
3s comp	93.07	25.46	215.28	603.8	2.019	1.43	132.68
3 comp	93.07	25.42	224.83	617.3	2.047	1.40	130.26
3 tot	289.06	25.42	224.83	617.3	2.047	1.40	404.56
4	289.06	25.38	539.60	1018.5	2.674	1.25	362.51
5	289.06	25.00	725.19	1253.8	2.938	1.28	370.21
5 after pipeline	289.06	24.63	725.11	1253.8	2.941	1.28	370.03
5b after inlet control valve	289.06	24.13	725.00	1253.8	2.945	1.28	369.79
6s	289.06	8.49	568.82	1067.0	2.945	1.21	350.14
6	289.06	8.49	580.74	1081.5	2.962	1.21	351.10
7	289.06	8.36	236.83	680.3	2.365	1.13	327.95

8 tot	289.06	8.24	106.54	526.8	2.019	1.32	381.11
9	195.99	8.07	52.00	439.9	1.773	2.40	469.55
10s	195.99	11.43	79.59	453.6	1.773	2.21	432.64
10	195.99	11.43	80.69	456.0	1.780	2.16	423.63

Table 5.8 Cycle thermodynamic points

5.2.2 Receiver

From the receiver mechanical analysis, it resulted that temperature limits chosen in the preliminary design (871°C) on the basis of Creep and Low cycle fatigue can be sustained if the tube diameter is kept 33.4 mm and thickness is 1.65mm. The ultimate design of the receiver was performed in order to keep maximum temperature of the receiver surface around 865°C, once de sign was made pressure drops were calculated in order to double check that internal pressure could be sustained by the tubes in the whole receiver.

Inlet parameter in the receiver model are reported in Table 5.9.

Parameter	Value	Notes
Sodium inlet temperature	556.5 °C	Calculated as Tin PHX + 15°C
Sodium outlet temperature	740.2 °C	Calculated as Tout PHX + 15°C
Receiver power duty	202.0 MW	Calculated as SM (3) times the inlet thermal power of the power block
Flux map	In Figure 5.12	From the solar field model given receiver dimensions and power duty

Table 5.9 Input parameters in the receiver model
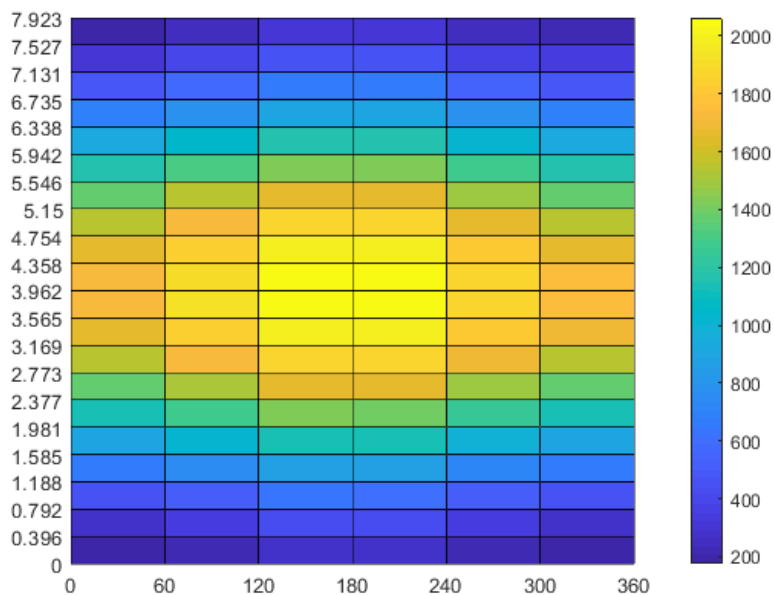
Figure 5.12 Flux map accounted in the ultimate design

From sodium temperatures and power requirement the HTF mass flow rate can be determined, 877.6 kg/s. The receiver flux arrangement has been modified from the preliminary design, the flow is divided in two paths, three passes and two parallel panels. The aspect ratio was modified to 0.95 (below the range of investigation of the optimal aspect ratio) in order to comply with fluid velocity limitations (6 m/s) without increasing the tubes diameter which would be detrimental for the heat exchange and it wouldn't be allowable due to stress limitations and to maintain maximum temperature of the receiver tubes equal to 865°C. Receiver geometrical characteristics and main calculation results are reported in Table 5.10.

Geometrical parameters		Results	
$H_{receiver}$	7.923 m	Sodium average velocity	5.933 m/s
$D_{receiver}$	8.34 m	Max tube wall temperature	864.92 °C
# parallel paths	2		
# passes in series	3	Max HTF film temperature	758.28 °C
# parallel panels	2		
DoutTUBE	33.4 mm	Max tube strain	0.28%
Thickness	1.65 mm	Mean heat flux	1118.06W/m^2
DinTUBE	30.1 mm	Max heat flux	2053.62 W/m^2
Ntubes/panel	65	$\eta_{thermal}$	87.02%

Table 5.10 Receiver ultimate design geometrical parameters and results

In order to evaluate, as precisely as possible, the pressure losses in the receiver all the tube links between the inlet and the outlet vessel were dimensioned, a detailed pipe-list of the receiver is reported in Table 5.11. Total pressure loss resulted to be 10.89 bar, considering also a geodetic step of 147.92 m the pump consumption is 3.51 MW.

section name	N of sections in parallel	Mass flow rate [kg/s]	Temperature [°C]	OD [mm]	Thickness [mm]	Length [mm]	Rugosity [μm]	Nr. entrances	Nr. exits	Nr. 90° curves	Nr. Valves	$\Delta P_{section}$ [bar]	Pressure bar
Inlet common pipe	1	877.6	556.5	660.4	12.70	147.92	45	1	1	2	1	0.30	11.89
Inlet tank to 1st panel	2	438.8	556.5	323.9	9.55	4.17	45	1	1	1	1	0.70	11.59
Link 1 in	4	219.4	556.5	273.0	9.27	1.64	45	1	1	1	0	0.30	10.90
1st panel Inlet Header	4	219.4	556.5	323.9	9.52	1.09	45	1	1	1	0	0.14	10.60
Panel 1 / stubs	**260**	**3.38**	**587.5**	**33.4**	**1.65**	**8.42**	**45**	**1**	**1**	**6**	**0**	**1.72**	**10.46**
Outlet Header	4	219.4	618.6	323.9	9.52	1.09	45	1	1	1	0	0.14	8.74
Link 1 out	4	219.4	618.6	273.0	9.27	1.64	45	1	1	1	0	0.30	8.59
Link 1 to 2	2	438.8	618.6	323.9	9.55	8.34	45	1	1	1	0	0.65	8.29
Link 2 in	4	219.4	618.6	273.0	9.27	1.64	45	1	1	1	0	0.30	7.65
Inlet Header	4	219.4	618.6	323.9	9.52	1.09	45	1	1	1	0	0.14	7.34
Panel 2 / stubs	**260**	**3.38**	**652.6**	**33.4**	**1.65**	**8.42**	**45**	**1**	**1**	**6**	**0**	**1.75**	**7.20**
Outlet Header	4	219.4	686.5	323.9	9.52	1.09	45	1	1	1	0	0.15	5.45
Link 2 out	4	219.4	686.5	273.0	9.27	1.64	45	1	1	1	0	0.31	5.30
Link 2 to 3	2	438.8	686.5	323.9	9.55	8.34	45	1	1	1	0	0.66	4.99
Link 3 in	4	219.4	686.5	273.0	9.27	1.64	45	1	1	1	0	0.31	4.33
Inlet Header	4	219.4	686.5	323.9	9.52	1.09	45	1	1	1	0	0.15	4.02
Panel 3 / stubs	**260**	**3.38**	**713.4**	**33.4**	**1.65**	**8.42**	**45**	**1**	**1**	**6**	**0**	**1.78**	**3.88**
Outlet Header	4	219.4	740.2	323.9	9.52	1.09	45	1	1	1	0	0.15	2.09
Link 3 out	4	219.4	740.2	273.0	9.27	1.64	45	1	1	1	0	0.31	1.94
Link to outlet vessel	2	438.8	740.2	323.9	9.55	4.17	45	1	1	1	0	0.63	1.63

Table 5.11 Ultimate design receiver pipe-list and pressure losses

5.2.3 Solar field

Solar field was designed to supply 232.10 MW$_{th}$ of incident thermal power to the receiver during design conditions (summer solstice, solar noon). None of the solar field parameters chosen in the preliminary design have been varied with the exception of the receiver size and power duty.

The design resulted in the adoption of 18786 heliostats disposed as in Figure 5.13, which results in a concentration ratio (CR) equal to 1883.02.
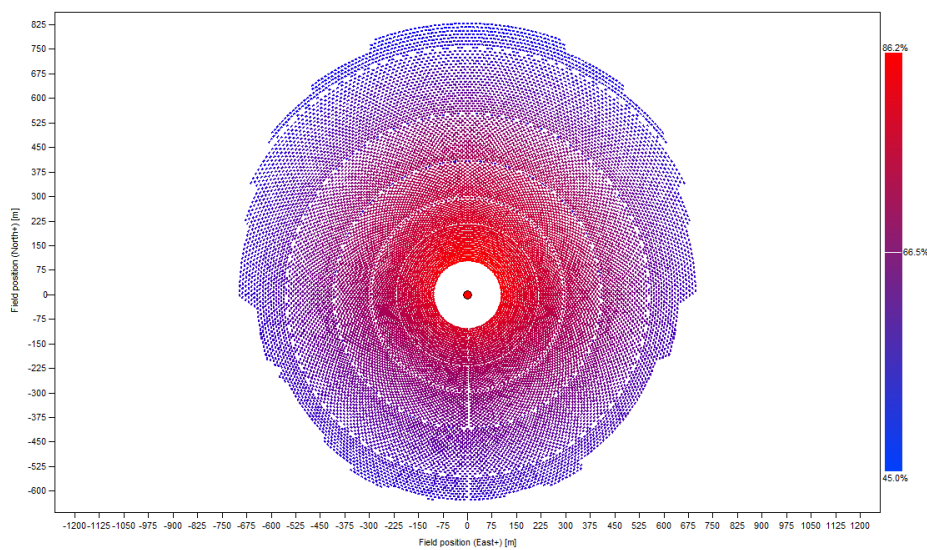
Figure 5.13 Solar field heliostats disposition in the ultimate design. Colours indicate heliostats total efficiency.

Average solar field efficiencies in design conditions are reported in Table 5.12.

	Units	Value	Mean	Minimum	Maximum	Std. dev
Cloudiness efficiency	%	100	100	100	100	0
Shading efficiency	%	100	100	100	100	0
Cosine efficiency	%	82.69	82.69	70.78	97.97	5.6572
Reflection efficiency	%	90.25	90.25	90.25	90.25	0
Blocking efficiency	%	99.79	99.79	71.68	100	1.3856
Attenuation efficiency	%	95.02	94.96	91.59	97.57	1.4682
Image intercept efficiency	%	91.45	91.12	58.26	99.94	9.0046
Absorption efficiency	%	100				
Solar field optical efficiency	%	64.71		39.85	86.17	9.9122

Table 5.12 Solar field design condition efficiencies

Where the minimum and maximum values are referred to the single heliostat while the first reported value is the nominal, field-wide, value that represents the best summary of the simulated system.

6 Annual simulation

An annual simulation was accomplished to determine the annual performances of the proposed layout. Annual weather data in the location near Las Vegas (35.57°N 115.47°W) which were used in the solar field design (where Ivanpah Solar Power facility was built), were downloaded from the U.S. National Solar radiation database. The database contains DHI, DNI, Wind Speed, Relative Humidity, Temperature and Pressure values discretized every half an hour for every day of 2018, which will be the reference year considered.

The significant data used for the performance analysis of the plant are the DNI, ambient temperature and wind velocity

These parameters influence the working condition of the receiver and power block, thus affecting their efficiency. For the annual simulation, also the thermal storage must be modelized since its design influences the annual electricity production.

6.1 Solar field annual optical efficiency

Solar field efficiency changes during the year and day since it depends from the incident angle of the sunray on the solar field heliostats' surface, it does not depend, instead, from the DNI. The incident angle depends on the solar azimuth and zenith which vary during the year as they depend on earth position with respect to the sun. In order to consider the effect of varying solar optical efficiency through the year and day, an efficiency matrix was computed through a parametric simulation performed with SolarPILOT. This matrix is then interpolated to find optical efficiency for every day of the year and hour of the day. The zenith angle is calculated from the horizontal plane, therefore 0° means the sun is at its maximum altitude and 90° means the is on the horizontal plane.
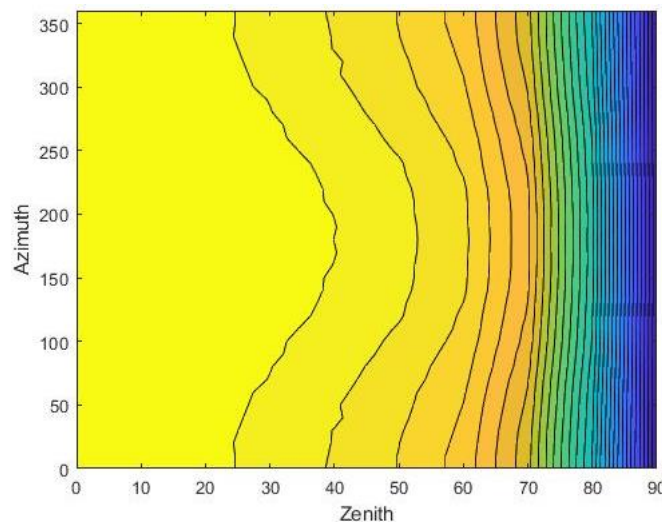
Figure 6.1 Solar field optical efficiency changing solar azimuth and zenith

6.2 Receiver annual thermal efficiency

Receiver efficiency is highly dependent on the irradiation hitting the receiver surface, which depends from the DNI and the solar angle (which affects solar field optical efficiency).

Irradiation has the most important effect on receiver efficiency. Although also ambient temperature and wind velocity influence it. Indeed, as wind velocity increases the external forced convection coefficient rises resulting in higher convective losses. As temperature decreases convective and radiative losses increase.

An analysis the influence of the three ambient parameters was performed. First the effect of irradiation and wind combined was evaluated with a parametric simulation varying them in the range of interest, 0%-100% of the nominal irradiation and from 0 to 11 m/s of wind speed. Then the same analysis was performed changing irradiation and ambient temperature in the range: -5°C to 45°C. These are the range of variation of DNI, ambient temperature and wind velocity in the reference site.

Results from these analyses are shown in Figure 6.2 and Figure 6.3, it can be seen that for irradiations close to the nominal one the effect of both temperature and wind velocity is small, the last one having a slightly higher impact. For lower irradiation percentages the effect of wind is much more significant, while the effect of temperature is still very little.

The total thermal losses in the receiver, depicted in Figure 6.4and Figure 6.5, depend on the irradiation since, decreasing power load, surface temperature decreases. Losses variation due to wind is much more evident than the one due to varying ambient temperature and it does not depend from power load, meaning that high wind speeds have the same detrimental effect in terms of losses independently from irradiation.
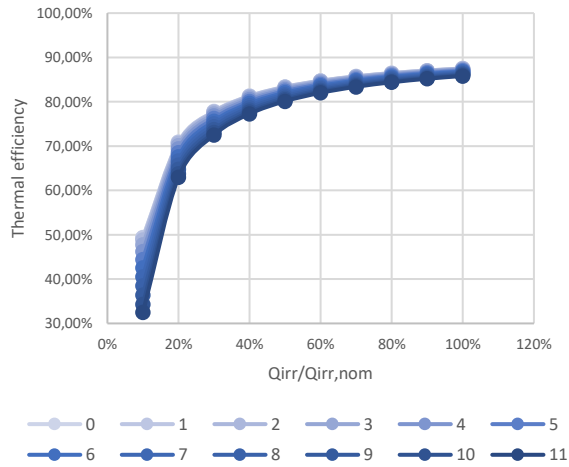
Figure 6.2 Effect of wind velocity and irradiation on receiver thermal efficiency
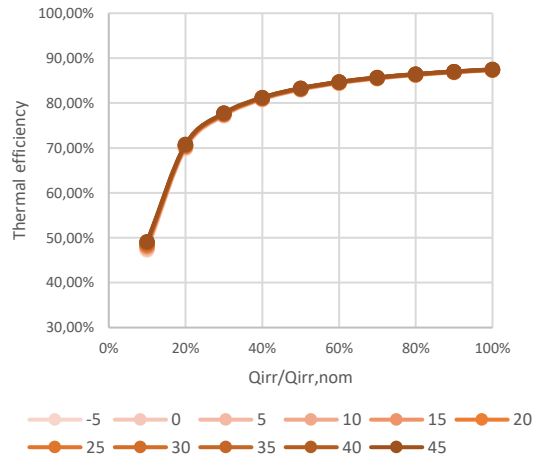
Figure 6.3 Effect of ambient temperature and irradiation on receiver thermal efficiency
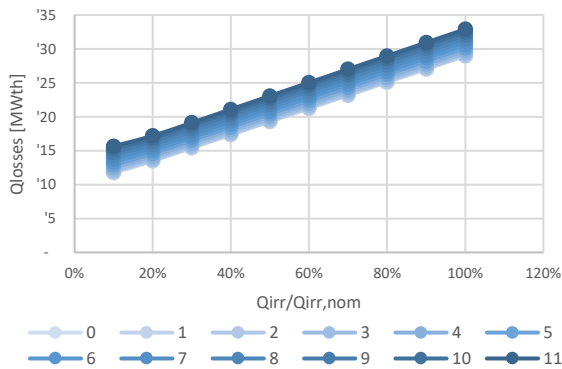
Figure 6.4 Receiver thermal losses varying irradiation on the receiver surface and wind velocity
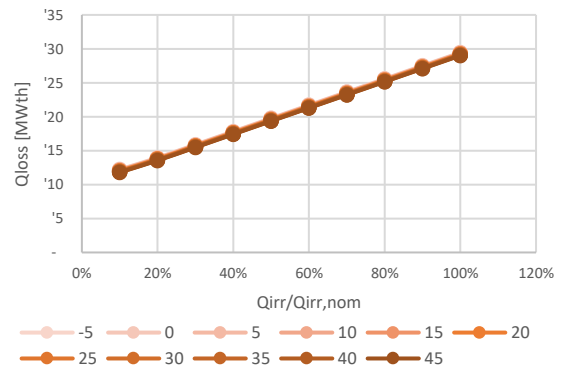
Figure 6.5Receiver thermal losses varying irradiation on the receiver surface and ambient temperature

Wind velocity has a more important effect on receiver thermal efficiency both for high and low irradiation values, while the efficiency variation due to temperature difference is significant (1% or higher) only if solar irradiation is below 20% of its nominal value. For these reasons only irradiation and wind velocity effects on receiver thermal efficiency have been taken into account in the creation of a thermal efficiency map for the annual simulation.

During the off design analysis also the maximum temperature of the receiver tube during off-design conditions was evaluated. Results (Figure 6.6 and Figure 6.7) show that wind speed and ambient temperature do not influence appreciably maximum temperature, while the partial load operation decreases the maximum wall temperature due to lower heat flux absorbed. The worst condition in terms of wall temperature is the 100% load, 0 m/s of speed and 45°C which results in a maximum receiver temperature of 865.5°C.
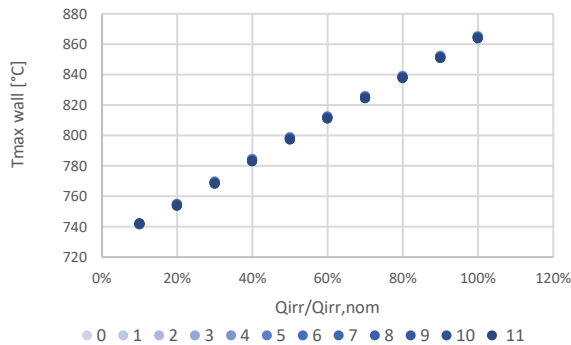
Figure 6.6 Maximum wall temperature varying irradiation load and wind velocity
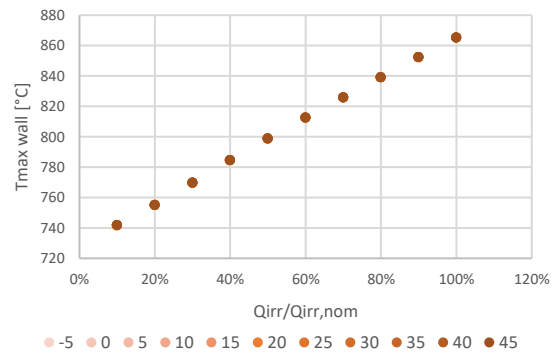
Figure 6.7 Maximum wall temperature varying irradiation load and ambient temperature

The effect of varying of the flux map shape wasn't taken into account because previous analyses [12],[4] showed that it doesn't have an important impact on the receiver performances.

It has been evaluated that for partial loads lower than 10% it is not possible to ensure with certainty the safe heat removal from the receiver tubes, keeping the outlet temperature constant, due to the too low velocity of the HTF in the tubes, moreover below 10% the thermal efficiency rapidly degrade resulting in values below 0 for partial loads of 5%. Therefore, when irradiation on the receiver is lower than 10 % heliostats will be defocused.

6.3 Thermal storage control strategy

The design of the thermal storage has a significant impact on the annual performances of the plant. The most important parameter which has to be chosen is the storage size. This parameter is usually expressed in equivalent hours of nominal power, 1 equivalent hour of storage corresponding to the thermal energy needed to work the power block at full load for 1 h.

Increasing the storage size is always favourable from an energy point of view since the bigger is the storage the lower will be the lost energy due to defocusing, although the storage hours must be chosen wisely in accordance with the Solar Multiple value because increasing the size of the thermal storage also the cost rises. If the solar multiple was too small, the choice of the maximum storage size could result in unnecessary oversizing of the storage tanks, which would never completely fill. Usually the storage size is defined in order to limit defocusing power to below 5% [105].

In order to calculate the total annual energy produced a storage control strategy was evaluated and it is reported in the flowchart showing in Figure 6.8.
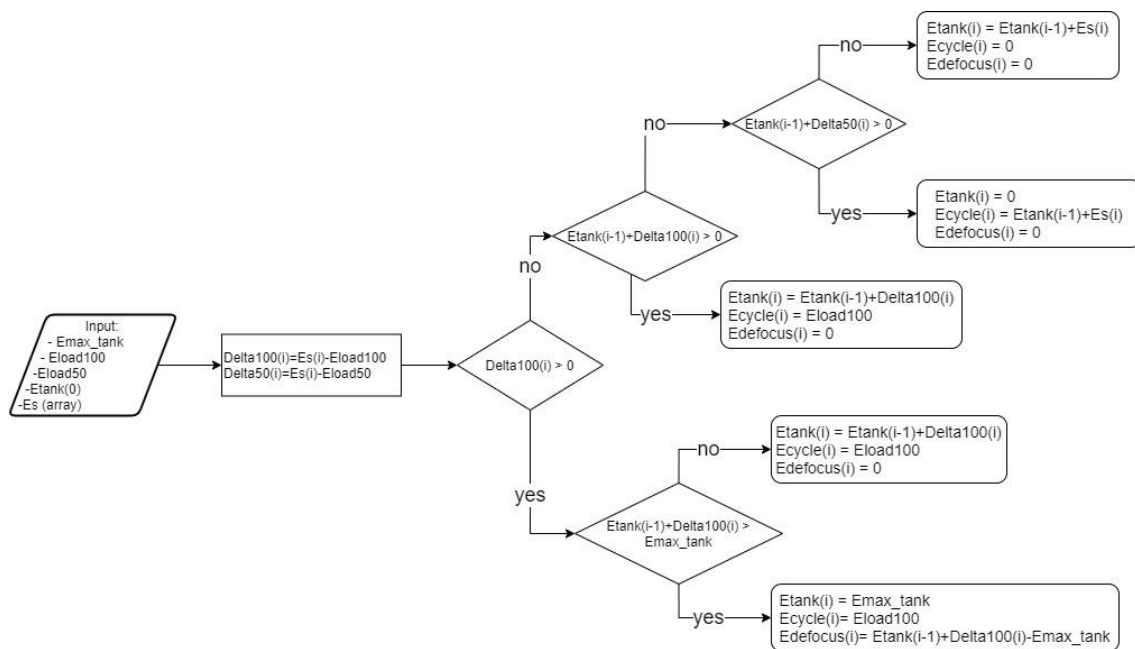
Figure 6.8 storage control strategy flowchart

The storage fills up only when:

- the energy entering the HTF from the sun is higher than the one required by the power block to work at 100%.
- The hot tank is not full.

In case the hot tank was full, only part of the heliostats would be focused on the receiver in order to inject in the HTF only the energy which is consumed by the power block.

In case the energy entering the HTF was lower the one needed to work the PB at 100% load the control system checks if the power stored in the hot tank until than moment is sufficient to integrate the power coming from the sun and to supply to the PB the full load thermal input, if this is possible the hot tank supplies the requested power.

In case the previously stored energy plus the entering energy from the sun is not sufficient to supply the PB at 100% load, the control system checks also if this total energy is able to supply at least 50% of the load, in this case there could be three possible responses of the system:

- Working the power block at 100% load for half the time
- Working the power block at partial load
- Store the energy in the hot tank to consume it later.

It is reasonable to assume that the first kind of response is adopted when the plant was working full load up until that moment and is about to switch off for a longer time (night time), in this case since the power block works at nominal load the efficiency is the nominal one. The second

kind of response is instead adopted when the plant was off before or it is a cloudy period therefore incoming energy is expected to be below the one required to supply the PB with 100% load for a longer period of time, although working the PB at partial load is detrimental for its efficiency therefore this strategy is often avoided in favour of the third. The third kind of response preserves the efficiency of the plant but it can mean that in some days in winter, when for many hours the irradiation is not sufficient to supply the full load thermal input requirement, the plant switches on and off many times a day, which is absolutely unwanted because time and energy required for the start-up and shut down of the plant cannot be neglected. The best control strategy in winter could be probably to follow the market prices stocking the energy when electricity is least requested and working the PB when electricity prices are high since filling of the hot tank is not a problem.

For the sole scope of determining the energy produced annually the strategy adopted in winter is not influent since none of these control strategies will influence defocused power and if the second strategy is avoided power block efficiency is constant. In summer, instead, it is rare that the energy in the tank plus the one coming from the sun is not sufficient to supply the full load thermal input, it can happen only at the end of the day if the tank isn't full enough to supply 100% load for the whole night, therefore the first control strategy is adopted without penalizing cycle efficiency.

In this work the solar multiple was assumed previously to be 3; with receiver and plant size fixed, the storage size was changed between 10 and 25 equivalent hours in order to evaluate the trend of the defocused power, considering only the portion defocused due to full storage and not the portion defocused due to lower loads than the minimum threshold (10%). Results from this analysis are reported in Figure 6.9.

As it can be seen from Figure 6.9, increasing the storage size up to about 14 heq, the defocused power decreases parabolically, after 14 heq, increasing the storage size is less effective on reducing the defocused power: indeed this loss decreases linearly.
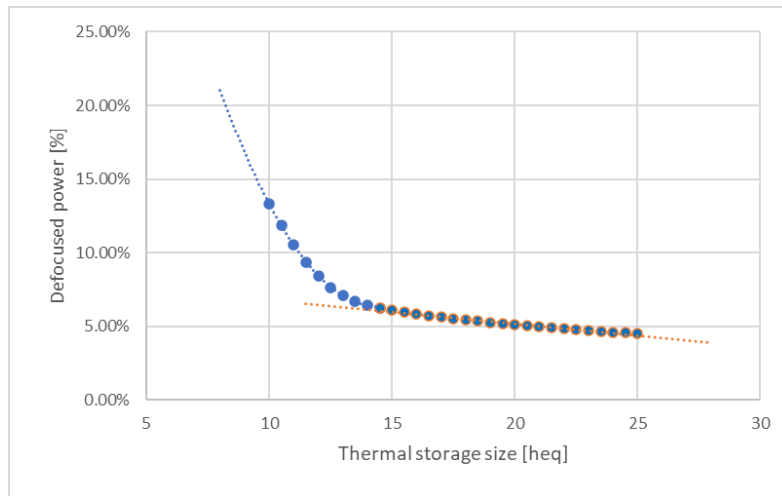
Figure 6.9 Percentage of the HTF incoming power which is defocused due to storage size limitations over storage size in equivalent hours

In order to explain this trend, it can be interesting to look at the storage tank energy variation through the year (Figure 6.10). If the PB is able to discharge the whole tank during the night, an increase in the storage size will reduce the energy defocused proportionally to the hours of storage added. There are periods of time, during summer, when the PB, instead, is not able to discharge the energy accumulated during the day; therefore, after a filling period, the tank is never emptied and it reaches its maximum filling capacity every sunny day. If there are consequent days in which the hot storage tank never empties, an increase in the storage size can only increase the duration of the initial filling time and the final emptying time, but during the period in which the tank never empties an increase in storage capacity does not contribute in any way to the reduction of the defocused energy. This happens since during these periods the storage tank can be filled only by an amount of energy equal to the energy which was discharged the previous night.

As it can be seen from graphs in Figure 6.10 for storage capacities higher than about 14h, most of the energy is defocused during long non-emptying periods, hence the further increase of storage capacity has a lower impact on the defocused energy.
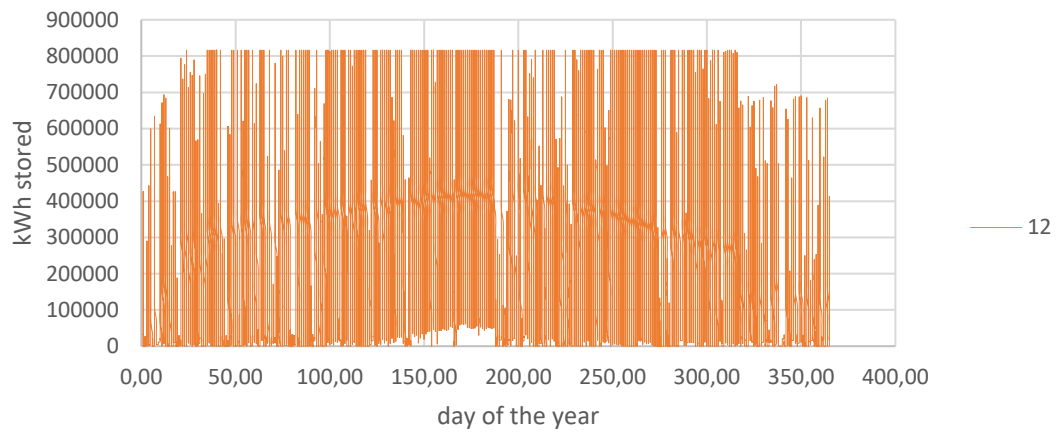
a
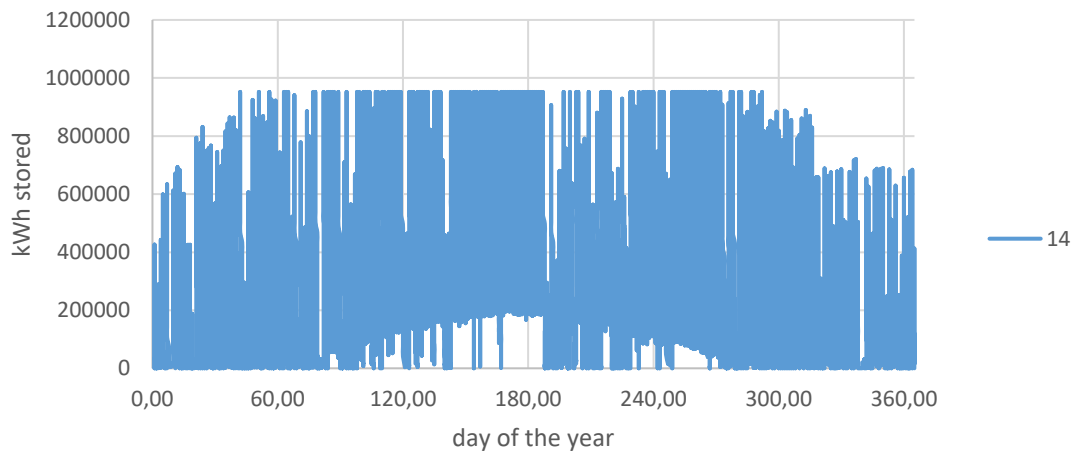
b
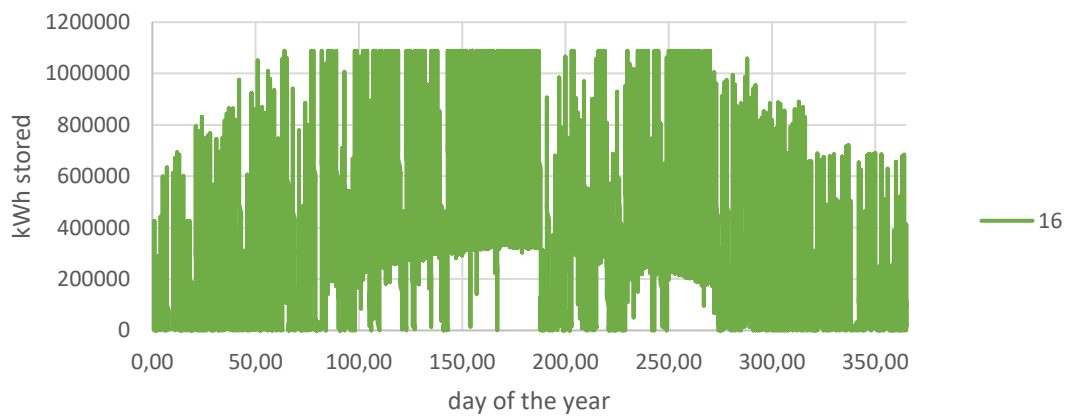
c

Figure 6.10 Energy stored in the storage tank through the whole year changing storage size, a) 12 h of storage b) 14 h and c) 16 h

In order to achieve a 5% of defocused power a storage size of about 20 heq would be needed. Although, a brief analysis on the existing technology [67] showed that maximum storage sizes

range between 15 equivalent hours (Shouhang Dunhuang 10 MW Phase I, China; Gemasolar Thermosolar Plant, Spain; DEWA CSP Tower Project, United Arab Emirates) and 17.5 equivalent hours (Atacama-1, Chile). Since this analysis is not taking into account the cost of the storage, which should instead be taken into account, it was decided not to exceed storage sizes usual in literature, therefore a storage size of 17 heq was chosen, corresponding to 1'700'165 MWth of power.

6.4 Auxiliary consumption

6.4.1 Heat rejection units (HRUs)

The analysis of the power block off-design efficiency goes beyond the scope of this work and it is not useful at this stage of analysis, indeed the thermodynamic cycle always works at 100% load with the exception of when some particular conditions, already explained in paragraph 6.3 occur. Moreover, a precise analysis of the off-design behaviour of the cycle would require off-design considerations for each component.

Only ambient temperature effect on the PB auxiliary consumption was thus taken into account. The design ambient temperature for this plant was considered to be 35°C, although for many days of the year ambient temperature is lower than this value. The control strategy for the PB in this case is to decrease or increase air mass flow rate in the heat rejection units in order to maintain constant minimum cycle temperature (52°C). In this way, turbomachinery, and all the HX with the exception of HRUs always work in nominal conditions.

The consumption of HRUs was evaluated changing the ambient temperature (Figure 6.11), considering the UA of the HX and the ΔTml constant, since HRUs were designed at the maximum ambient temperature, precooler and intercooler are able to exchange nominal rejection power in every ambient condition.
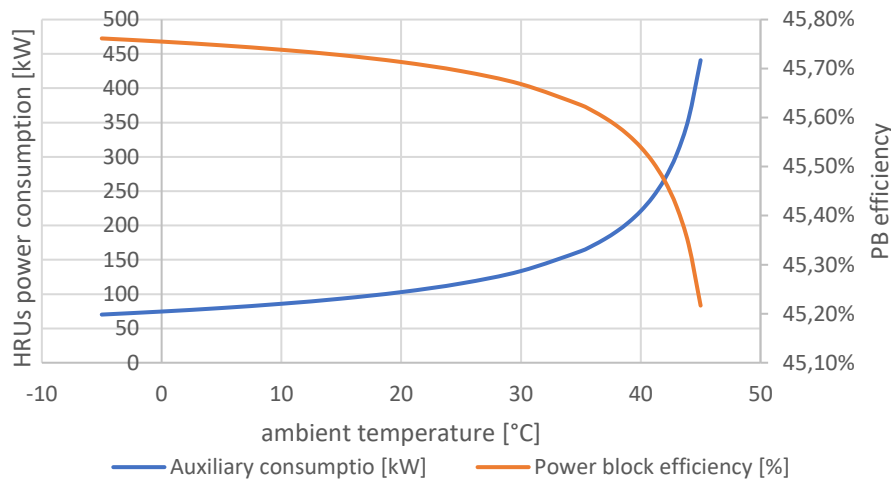
Figure 6.11 Power consumed from HRUs and net PB efficiency varying ambient temperature.

As it can be seen from Figure 6.11 power consumed by the heat rejection auxiliary systems increases more than exponentially for high temperatures, HRUs consumptions were accounted in the power block efficiency since this consumption affects the net power cycle efficiency (Figure 6.11).

6.4.2 Sodium circulation system

As explained in section 0, sodium is circulated in two independent loops, each of them equipped with a circulating pump.

The pump on the PHX loop works only when the power block is operating, since the PB almost always works at full load, the PHX pump work with a constant HTF mass flow rate and its consumption is two orders of magnitude lower than the pump on the receiver loop [12]. For this reason the power loss due to this pump consumption hasn't been taken into account in this analysis.

The pump on the receiver loop, instead, has an influent power consumption (in the order of MW) and has a changing mass flow rate which depends from the receiver loading. In order to evaluate the annual pump consumption a parametric analysis considering partial loads was performed. Pressure losses were evaluated for each case considering the pipe-list in Table 5.11. It is possible to see from the results, shown in Figure 6.12, that power consumption increase parabolically as the receiver load approaches 100%.
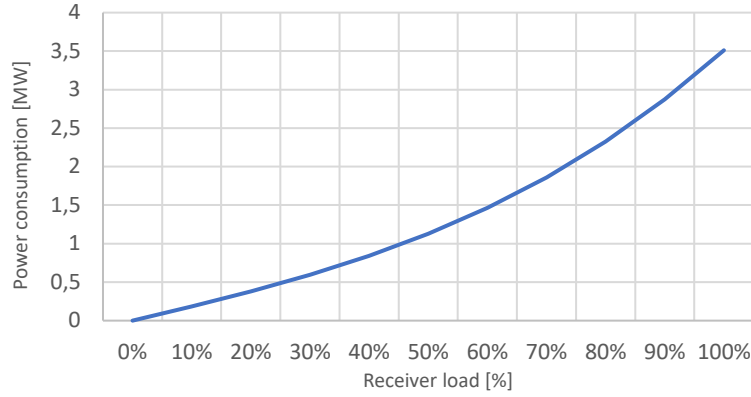
Figure 6.12 Power consumption of the HTF receive circulation pump varying receiver load

6.5 Annual simulation results

The annual simulation starts from the incident DNI on a discretized instant of time, i, to calculate the incident irradiation on the solar field during that time, since DNI data are given every 30 minutes, it is possible to evaluate production in terms of energy.

$$E_{SF_{incident}} = DNIA_{heliostat}n_{heliostats}\,0.5\,hours \quad [MWh_{th}]$$

Eq. 6.1

Then the efficiency of the solar field during that period of time is evaluated basing on the zenith and azimuth angle, interpolating the efficiency table produced with SolarPILOT. The energy hitting the receiver can be calculated as in Eq. 6.2.

$$E_{Receiver_{incident}} = E_{SF\,incident} * \eta_{opt} \quad [MWh_{th}]$$

Eq. 6.2

The receiver efficiency is, as well, determined interpolating the efficiency matrix, dependent of Receiver incident power and air velocity. Energy which could potentially enter the HTF is calculate as in Eq. 6.3, this energy is only theoretically the one entering the HTF because part of this energy could be defocused (basing on the thermal storage control strategy section 6.3, Figure 6.8) and never actually be transformed into thermal energy in the HTF.

$$E_{HTF_{theoretical}} = E_{Receiver_{incident}} * \eta_{thermal} \quad [MWh_{th}]$$

Eq. 6.3

The effect of minimum receiver working load is accounted in the thermal efficiency term since part of the energy incident on the receiver will never be transformed into HTF heat.

Through the storage system control strategy it is possible to determine how much of this energy is defocused ($E_{defocus}$), sent to the power block (E_{PB}), or stored in the hot tank, as well as

138

determining how much of the stored energy is used, controlling the amount of energy stored in every time-step (E_{tank}).

The energy going to the cycle is multiplied to the net PB efficiency, which depends from ambient temperature since HRUs auxiliary consumption is account din the PB efficiency.

$$E_{el\ produced} = E_{PB} * \eta_{PB} \quad [MWh_{th}]$$

<div align="right">Eq. 6.4</div>

The energy delivered is the energy produced minus the one necessary to the SF auxiliary systems (mainly the receiver sodium circulation pump).

$$E_{el\ delivered} = E_{produced} - E_{SFaux} \quad [MWh_{th}]$$

<div align="right">Eq. 6.5</div>

In order to get annual performances, the energies calculated on the 30 minutes time step are summed up for 8760 hours (17520 half an hours) and efficiencies are calculated in as reported in the following equations.

$$\eta_{opt_{annual}} = \frac{\sum E_{Receiver_{incident}}}{\sum E_{SF_{incident}}}$$

<div align="right">Eq. 6.6</div>

$$\eta_{thermal_{annual}} = \frac{\sum E_{HTF_{theoretical}}}{\sum E_{Receiver_{incident}}}$$

<div align="right">Eq. 6.7</div>

$$\eta_{defocus_{annual}} = \frac{\sum E_{PB}}{\sum E_{HTF_{theoretical}}}$$

<div align="right">Eq. 6.8</div>

$$\eta_{PB_{annual}} = \frac{\sum E_{el_{produced}}}{\sum E_{PB}}$$

<div align="right">Eq. 6.9</div>

$$\eta_{SF\ aux_{annual}} = \frac{\sum E_{el_{delivered}}}{\sum E_{el_{produced}}}$$

<div align="right">Eq. 6.10</div>

$$\eta_{sol\ to\ el} = \frac{\sum E_{el_{delivered}}}{\sum E_{SF_{incident}}}$$

<div align="right">Eq. 6.11</div>

Annual results are reported in Table 6.1.

$E_{SF_{incident}}$ Field incident thermal power [MWh]	1'082'447	$\eta_{opt_{annual}}$ Annual optical efficiency	55.46% (64.71%)
$E_{Receiver_{incident}}$ Solar power to receiver [MWhth]	600'290	$\eta_{thermal_{annual}}$ Annual thermal efficiency	84.42% (87.02%)
$E_{HTF_{theoretical}}$ Solar power to HTF [MWhth]	506'753	$\eta_{defocus_{annual}}$ Annual defocusing efficiency	94.47%
E_{PB} Thermal energy entering the WF [MWhth]	478'738	$\eta_{PB_{annual}}$ Annual PB efficiency	45.69% (45.63%)
$E_{el_{produced}}$ Gross electricity production [MWhe]	218'752	$\eta_{SF\ aux_{annual}}$ Annual SF auxiliary efficiency	99.99%
$E_{el_{delivered}}$ Net electricity production [MWhe]	218'736	$\eta_{sol\ to\ el}$ Annual solar to electric efficiency	20.21% (22.79%)
h_{eq} of operation	7040 h	h_{eq} of defocusing	412 h
CF	0.804h	Percentage power defocused	5.53%

Table 6.1 Annual simulation results, in the parentheses design conditions results for comparison

As expected the optical and thermal efficiencies are negatively affected from working in off design conditions for most of the hours of the year, while the PB is always operated at full load and instead it benefits from the lower average ambient temperature, which for the site chosen is around 19°C, therefore the average auxiliary consumption of the HRUs is below the design one in design conditions.

Solar to electric efficiency results slightly higher that the efficiency range of conventional SPT (7%-20%), found in the 2012 report from IRENA on CSP [106]. Moreover the Capacity Factor (CF) is consistent with the report [106] which assesses that capacity factors of 0.8 can be achieved with storage capacities of 15 h.

7 Conclusions and future developments

As it is emerging from climate change data, the problem of global warming has to be addressed as soon as possible. For this reason, many countries are investing in renewable energy sources in order to limit their energy sector carbon intensity. The increase of power installed from unpredictable and intermittent renewable sources such as wind and PV has increased majorly in the last decade and has brought new grid control challenges and an increased need of new methods of energy storage.

CSP can be a very interesting technology due to its ability to produce dispatchable renewable power. Its LCOE is, although, still too high to make this technology competitive with other renewable technologies such as PV and wind, therefore efficiency improvement and cost reduction is necessary.

The purpose of this study was to assess limitations and issues which must be addressed in order to build an optimized SPT plant with sodium as HTF and sCO_2 as working fluid in the PB.

Initially a literature review was carried out in order to choose the most promising HTF, sodium was chosen for outstanding heat transfer characteristics of liquid metals with respect to molten salts and for the maturity level of the technology with respect to other liquid metals such as lead-bismuth eutectic, indeed liquid sodium has been studied, tested and commercialized as a primary and secondary HTF for fast breed nuclear reactors.

In order to exploit the higher maximum temperature of liquid sodium with respect to solar salts a sCO_2 was employed as working fluid, CO_2 has also other advantages as smaller turbomachinery and potentially higher cycle efficiency. The choice of the cycle configuration was based on previous studies which asses its high efficiency, in particular the study of Polimeni et al. [4] highlights superior performances of the RMCI over SC, RC and PC.

The receiver geometry and aspect ratio, the solar field aiming strategy cut off factor and the turbine inlet temperature were optimized through parametric analyses. Power block turbine expansion ratio and RPR were optimized in every parametric case. Moreover receiver dimensions were changed in each case in order to comply with tubes material temperature limitation.

From this analysis it emerged that a good receiver configuration, compliant with technical limits, has tube diameter 33.4 mm, corresponding to the standard 1 inch dimension, flow is distributed on three passes in series, each pass is divided in two parallel panels in order to ease panel transport. This geometrical design gives good results in terms of heat transfer without increasing the fluid velocity over the critical value of 6 m/s, receiver dimensions were instead changed each time in order to maintain temperatures below their limits.

From the parametric analysis on the aspect ratio, defined as H/D, emerged that aspect ratios closer to 1 result in higher optical efficiency and lower thermal efficiency of the receiver due to a more peaked flux map, indeed, in order to maintain maximum tube temperature fixed with

higher peak fluxes, the receiver area must be increased. The overall solar to thermal efficiency decreases, ranging from 57.01% to 53.92%, when the aspect ratio is varied from 0.98 to 2.1.

The solar field positioning cut off factor was also optimized, this parameter determines the aiming strategy of heliostats to the receiver, it influences the shape of the flux map and the optical efficiency, particularly the image intercept efficiency. Increasing the positioning cut off factor enhances the optical efficiency, but it increases peak flux consequently influencing negatively thermal efficiency. From the results it emerged that overall efficiency is highest when the cut off factor is 2.5, although, between a value of 2 and a value of 2.5 the efficiency increases of less than 0.3% (57.07% and 57.32% with cut off factor equal to 2 and 2.5 respectively) while receiver surface area must be increased by 1/5 of the total surface to comply with temperature limitations. For this reason, the cut off factor was set to 2.

Lastly the analysis on maximum turbine inlet temperature highlighted that increasing temperature in the range investigated (723.6°C-785°C) is always beneficial for the overall plant efficiency (ranging from 23.7% to 25.7%), with PB efficiency increasing and receiver thermal efficiency decreasing as expected. Another interesting result is that increasing TIT and keeping constant maximum tube temperature, optical efficiency increases, this is due to the larger receiver area, hence there are less heliostats (due to the higher efficiency and fixed power output), which aim at a larger target.

During the investigation of technical limits, it emerged that the most critical aspects are the very elevated temperatures and heat fluxes. In particular, at very high CR the mechanical design of the receiver is very challenging since this component is exposed to high uneven irradiation, which result in unbalanced peaks in material temperature. The limit analysis showed that a maximum temperature of 871°C can be sustained by the tubes material coupled with a tube diameter of 33.4 mm and 1.65 mm, increasing tube diameter or decreasing thickness would result in unacceptable high stresses.

Other critical components are the HXs, indeed PCHE are limited in temperature and pressure, high pressure PCHE cannot sustain temperatures above 650°C. Moreover, PCHE layout, with its very small channels, is not suitable for sodium since plugging due to solidified particles of sodium could be an issue. For these reasons, at this temperature and pressure the only viable option for the PHX is a shell and tube, its feasibility has been verified with Alpha Laval but the projected cost is high. PCHE are, instead, feasible and particularly interesting for the regenerators, this layout, indeed, allows a more efficient heat exchange with a smaller HX volume, thus reducing its cost.

The feasibility study of the turbine, performed in collaboration with Franco Tosi Meccanica, showed that sCO2 turbine which does not comprise blade refrigeration is possible with TIT below 750°C, at this temperature, though, rotor must be cooled. The effectiveness of the cooling process in this type of turbine was verified through a study of the Nusselt numbers varying cooling mass flow rates, although refrigeration is not always convenient in terms of efficiency and turbine complexity.

Considering the use of alloy N07263, rotor must be cooled down to 725°C, maximum allowable temperature for the cited material considering creep. Decreasing TIT to 725°C instead of refrigerating the turbine rotor of a 750°C (TIT) turbine has the same detrimental effect on efficiency as a cooling mass flow rate of 2.66% of the working fluid mass flow rate.

The turbine analysis reports also two possible designs of the turbine. The first one is the maximum efficiency design, reaching 93.19% of overall blading efficiency, in this design all stages are 0.5 degree of reaction. The second design, instead, was conceived in order to decrease as much as possible the number of stages and the temperature in the first stages of the turbine, in order to decrease the need of high temperature resistance materials earlier in the stages. This layout is designed with a lower degree of reaction in the first stages, although this design penalizes efficiency which can only reach 92.26%.

Together with FTM, a few considerations on the compressors were discussed. Compressors are all radial, due to their reduced sizes and they have been assumed directly coupled to the turbine through a gear box. A simple compressor sizing has been performed through the Balje diagram keeping efficiency around its optimal value of 85%.

A new optimized plant design was made, considering TIT equal to 725°C and the new turbine efficiency resulting from the turbine feasibility study. Moreover additional pressure losses on the pipeline from PHX to the turbine and on the turbine inlet control valve were considered. Limitations accounted in the preliminary design for the receiver were, instead, confirmed from the mechanical analysis. The performance assessment of the ultimate design results are reported in Table 7.1.

PB efficiency	45.63%
Receiver thermal efficiency	87.02%
SF optical efficiency	64.71%
SF aux consumption	3.51 MW
Net solar to electric efficiency	22.79 %

Table 7.1 Ultimate design performances in design conditions

Subsequently the off-design conditions of the optimized plant were analysed in order to perform the annual simulation and a storage control strategy was developed. Results of the annual analysis show reduced optical and thermal efficiencies, respectively 55.46% and 84.42%, due to the effect of off-design operation, while power block efficiency, 45.69%, is slightly increased since average site temperature is about 19°C while design ambient temperature is 35°C, therefore the reduction in HRUs consumption affects positively the PB efficiency. The solar to electric efficiency, 20.21%, is slightly higher than the solar to electric efficiency range for conventional SPT plants reported by IRENA [106]. The high capacity factor, 0.804, is explained by the large SM and storage and is compliant with IRENA [106].

From this thesis work it emerged that components limitations are often not technical but economical, indeed more performing materials and more complex solutions can often be employed in order to increase performances despite a very high increase of cost. In example

turbine rotor and blades could be refrigerated in order to increase the turbine intel temperature, although the increase in efficiency wouldn't probably justify the higher complexity and cost; the shell and tube PHX can be designed to resist to very high temperature and pressures increasing material resistance and tube thicknesses, increasing the material needed for the construction. Some solutions which present very high performances are not considered in the industry sector due to prohibitive costs.

Choices taken in this study favoured efficiency over reduced cost, for example high temperature and pressure in the sCO_2 cycle make unfeasible the employment of hybrid heat exchangers for the PHX which must be designed as a very expensive shell and tube HX. Other examples are the solar multiple and storage size which should be optimized through a technoeconomic study, while in this study were pushed to very high values to increase the capacity factor.

For these reasons the author advices a future economic study, coupled to this one, in order to assess equipment cost and compare plant LCOE with the SOA of CSP plants. In the cited study plant layout and parameters chosen should be optimized considering LCOE instead of efficiency.

Another essential development according to the author opinion is the increase of plant nominal power, indeed, SPT plant which are being built in the latest years are larger in size with respect to the one analysed in this study, their nominal power ranges around the hundred of Megawatts to exploit the scale effect decreasing LCOE. If sodium receiver coupled with sCO_2 cycle needs to be commercially competitive with other CSP layouts, nominal power should increase up to at least 100 MW. Future studies should focus on technical challenges arising from an increased design power.

Lastly, once the competitivity of this kind of plant has been assessed, a study focused on the partial load performances of the sCO_2 power block should be performed, in order to assess if this kind of plant configuration can be competitive also in a future scenario, when electricity produced by CSP plants will be used to cover negative production peaks of the intermittent renewable sources.

Bibliography

[1]   IEA, "https://www.iea.org/data-and-statistics?country=WORLD&fuel=Renewables%20and%20waste&indicator=Solar%20PV%20electricity%20generation." .

[2]   IRENA International Renewable Energy Agency, *Renewable Power Generation Costs in 2017*. 2018.

[3]   N. Boerema, G. Morrison, R. Taylor, and G. Rosengarten, "Liquid sodium versus Hitec as a heat transfer fluid in solar thermal central receiver systems," 2012.

[4]   S. Polimeni, M. Binotti, L. Moretti, and G. Manzolini, "Comparison of sodium and KCl-MgCl2 as heat transfer fluids in CSP solar tower with sCO2 power cycles," *Sol. Energy*, vol. 162, no. January, pp. 510–524, 2018.

[5]   O. J. Fous, "Sodium-NaK Engineering Handbook," vol. I, p. 339, 1972.

[6]   T. W. Neises and C. S. Turchi, "A Comparison of Supercritical Carbon Dioxide Power Cycle Configurations with an Emphasis on CSP Applications," *Energy Procedia*, vol. 49, pp. 1187–1196, Jan. 2014.

[7]   C. S. Turchi, Z. Ma, and J. Dyreby, "Supercritical carbon dioxide power cycle configurations for use in concentrating solar power systems," *Proc. ASME Turbo Expo*, vol. 5, no. March, pp. 967–973, 2012.

[8]   S. M. Besarati and D. Y. Goswami, "Supercritical CO2 and other advanced power cycles for concentrating solar thermal (CST) systems," in *Advances in Concentrating Solar Thermal Research and Technology*, Woodhead Publishing, 2016, pp. 157–178.

[9]   D. Thanganadar, F. Asfand, and K. Patchigolla, "Performance Analysis of Supercritical CO 2 Cycles for CSP," *SOLARPACES 2019 Int. Conf. Conc. Sol. Power Chem. Energy Syst.*, pp. 7–8, 2019.

[10]   V. T. Cheang, R. A. Hedderwick, and C. McGregor, "Benchmarking supercritical carbon dioxide cycles against steam Rankine cycles for Concentrated Solar Power," *Sol. Energy*, vol. 113, pp. 199–211, 2015.

[11]   M. Binotti, M. Astolfi, S. Campanari, G. Manzolini, and P. Silva, "Preliminary assessment of sCO2 cycles for power generation in CSP solar tower plants," *Appl. Energy*, vol. 204, pp. 1007–1017, 2017.

[12]   S. Polimeni, "Techno-economic assessement of innovative high temperature solar receiver coupled with sCO2 cycles," 2015.

[13]   H. Benoit, L. Spreafico, D. Gauthier, and G. Flamant, "Review of heat transfer fluids in tube-receivers used in concentrating solar thermal systems: Properties and heat transfer coefficients," *Renewable and Sustainable Energy Reviews*. 2016.

[14]   D. L. Siebers and J. S. Kraabel, "Estimating Convective Energy Losses From Solar Central Receivers," 1984.

[15]   E. Achenbach, "The effect of surface roughness on the heat transfer from a circular cylinder to the cross flow of air," *Int. J. Heat Mass Transf.*, vol. 20, no. 4, pp. 359–369, 1977.

[16]   Tempil, "Product Data : Pyromark° 2500 Flat Black," *Http://Www.Tempil.Com/Specialty-Coatings/Pyromark-High-Temperature-Paint/*, no. 847, p. 60007, 2013.

[17]   NREL, "Solar Pilot." .

[18]   P. Features, "HAYNES ® 230 ® alloy," 2019.

[19]   R. E. Division, "Thermodyn a Mic and Transport Properties of Sodium Liquid and Vapor."

[20]   B. and Wilcox, "Molten salt thermal energy storage subsystem research experiment. Volume 2. Final Technical Report."

[21]   ASME, "ASME BPV Code SEC II Part D (Metric) 2010," 2010.

[22]   R. Le Pierres, D. Southall, and S. Osborne, "Impact of Mechanical Design Issues on Printed Circuit Heat Exchangers," *Proc. SCO2 Power Cycle Symp. 2011*, 2011.

[23]   S. p. a. Franco Tosi Meccanica, "Considerazioni sul progetto di turbina a CO2." .

[24]   "Climate Change: Atmospheric Carbon Dioxide | NOAA Climate.gov." [Online]. Available: https://www.climate.gov/news-features/understanding-climate/climate-change-atmospheric-carbon-dioxide. [Accessed: 20-Mar-2020].

[25]   "Effects | Facts – Climate Change: Vital Signs of the Planet." [Online]. Available: https://climate.nasa.gov/effects/. [Accessed: 20-Mar-2020].

[26]   "Renewables in Electricity Production | Statistics Map by Region | Enerdata." [Online]. Available: https://yearbook.enerdata.net/renewables/renewable-in-electricity-production-share.html. [Accessed: 20-Mar-2020].

[27]   V. Dostal, D. MJ, and H. P.A, "A supercritical carbon dioxide cycle for next generation nuclear reactors, MIT-ANP-TR-100, advanced nuclear power technology program report. Cambridge (MA): Massachusetts Institute of Technology." 2004.

[28]   G. Angelino, "Real Gas Effects in Carbon Dioxide Cycles." p. V001T01A071, 1969.

[29]   G. Angelino, "Carbon Dioxide Condensation Cycles For Power Production," *Journal of Engineering for Gas Turbines and Power*, vol. 90, no. 3. p. 287, 1968.

[30]   T. W. Neises and C. S. Turchi, "Supercritical carbon dioxide power cycle design and configuration optimization to minimize levelized cost of energy of molten salt power towers operating at 650 °C," *Sol. Energy*, vol. 181, pp. 27–36, Mar. 2019.

[31]   J. Dyreby, S. Klein, G. Nellis, and D. Reindl, "Design Considerations for Supercritical Carbon Dioxide Brayton Cycles With Recompression," *J. Eng. Gas Turbines Power*, vol. 136, no. 10, p. 101701, 2014.

[32]   F. Crespi, G. Gavagnin, D. Sánchez, and G. S. Martínez, "Analysis of the Thermodynamic Potential of Supercritical Carbon Dioxide Cycles: A Systematic Approach," *J. Eng. Gas Turbines Power*, vol. 140, no. 5, May 2018.

[33]   M. D. Carlson, "GUIDELINES FOR THE DESIGN AND OPERATION OF SUPERCRITICAL CARBON DIOXIDE R & D SYSTEMS," *SOLARPACES 2019 Int. Conf. Conc. Sol. Power Chem. Energy Syst.*, no. 505, pp. 2–3, 2019.

[34]   M. Mecheri and Y. Le Moullec, "Supercritical CO2 Brayton cycles for coal-fired power plants," *Energy*, vol. 103, pp. 758–771, 2016.

[35]   Y. Ma, M. Liu, J. Yan, and J. Liu, "Thermodynamic study of main compression intercooling effects on supercritical CO2 recompression Brayton cycle," *Energy*, vol. 140, pp. 746–756, Dec. 2017.

[36]   F. A. Al-Sulaiman and M. Atif, "Performance comparison of different supercritical carbon dioxide Brayton cycles integrated with a solar power tower," *Energy*, vol. 82, pp. 61–71, Mar. 2015.

[37]   J. Pacio, A. Fritsch, C. Singer, and R. Uhlig, "Liquid metals as efficient coolants for high-intensity point-focus receivers: Implications to the design and performance of next-generation CSP systems," in *Energy Procedia*, 2013.

[38]   J. Pacio and T. Wetzel, "Assessment of liquid metal technology status and research paths for their use as efficient heat transfer fluids in solar central receiver systems," *Sol. Energy*, vol. 93, pp. 11–22, 2013.

[39]   D. Stahl, F. K. Boese, and S. Kostrzewa, "System and components design of a sodium heat transfer circuit for solar power plants," *Electr. Power Syst. Res.*, vol. 3, no. 3–4, pp. 151–161, 1980.

[40]   N. Lorenzin and A. Abánades, "A review on the application of liquid metals as heat transfer fluid in Concentrated Solar Power technologies," *Int. J. Hydrogen Energy*, vol. 41, no. 17, pp. 6990–6995, 2016.

[41]   F. Muller-Steinhagen, Hans; Trieb, Freng; Trieb, "Concentrating solar power."

[42]   M. Liu *et al.*, "Review on concentrating solar power plants and new developments in high temperature thermal energy storage technologies," *Renewable and Sustainable Energy Reviews*. 2016.

[43]   H. L. Zhang, J. Baeyens, J. Degrève, and G. Cacères, "Concentrated solar power plants: Review and design methodology," *Renewable and Sustainable Energy Reviews*. 2013.

[44]   B. Hoffschmidt, "Receivers for Solar Tower Systems," *Sfera2*, p. 33, 2014.

[45]   D. Castelli, "POLITECNICO DI MILANO Sviluppo del modello termico di un ricevitore solare a torre con fluido termovettore monofase," pp. 1–11, 2012.

[46]   and G. C. Lee A. Weinstein, James Loomis, Bikram Bhatia, David M. Bierman, Evelyn N. Wang, "Concentrating Solar Power," pp. 0–3, 2010.

[47]   A. Soni, A. Patel, M. Pandey, and A. Gour, "Overview Of Different Solar Receiver on Basis of its Configuration and Heat Transfer Fluid," vol. 5, no. 3, pp. 522–528, 2017.

[48]   A. A. Shah, C. Ungaro, and M. C. Gupta, "High temperature spectral selective coatings for solar thermal systems by laser sintering," *Sol. Energy Mater. Sol. Cells*, vol. 134, pp. 209–214,

2015.

[49]   K. Vignarooban, X. Xu, A. Arvay, K. Hsu, and A. M. Kannan, "Heat transfer fluids for concentrating solar power systems - A review," *Appl. Energy*, vol. 146, pp. 383–396, 2015.

[50]   J. Birnbaum *et al.*, "Steam temperature stability in a direct steam generation solar power plant," *Sol. Energy*, vol. 85, no. 4, pp. 660–668, 2011.

[51]   L. Heller, "Literature review on heat transfer fluids and thermal energy storage systems in CSP plants," *Lit. Rev. heat Transf. fluids Therm. energy storage Syst. CSP plants*, 2013.

[52]   W. Ding, A. Bonk, and T. Bauer, "Molten chloride salts for next generation CSP plants: Selection of promising chloride salts & study on corrosion of alloys in molten chloride salts," *SOLARPACES 2018 Int. Conf. Conc. Sol. Power Chem. Energy Syst.*, vol. 2126, p. 200014, 2019.

[53]   N. Bartos and J. Fisher, "Experiences From Using Molten Sodium Metal As A Heat Transfer Fluid In Concentrating Solar Thermal Power Systems."

[54]   J. Coventry, C. Andraka, J. Pye, M. Blanco, and J. Fisher, "A review of sodium receiver technologies for central receiver solar power plants," *Sol. Energy*, vol. 122, pp. 749–762, Dec. 2015.

[55]   C. Corgnale, B. Hardy, T. Motyka, R. Zidan, J. Teprovich, and B. Peters, "Screening analysis of metal hydride based thermal energy storage systems for concentrating solar power plants," *Renewable and Sustainable Energy Reviews*. 2014.

[56]   K. Niedermeier, J. Flesch, L. Marocco, and T. Wetzel, "Assessment of thermal energy storage options in a sodium-based CSP plant," *Appl. Therm. Eng.*, vol. 107, pp. 386–397, Aug. 2016.

[57]   E. G. Feher, "The supercritical thermodynamic power cycle," *Energy Convers.*, vol. 8, no. 2, pp. 85–90, 1968.

[58]   R. Vijaykumar, M. L. Bauer, M. Lausten, and A. M. Shultz, "Optimizing the supercritical CO2 Brayton cycle for concentrating solar power application," *6th Int. Symp. - Supercrit. CO2 Power Cycles*, 2018.

[59]   M. A. Reyes-Belmonte, A. Sebastián, M. Romero, and J. González-Aguilar, "Optimization of a recompression supercritical carbon dioxide cycle for an innovative central receiver solar power plant," *Energy*, 2016.

[60]   A. B. Zavoico, "SAND2001-2100 Unlimited Release Solar Power Tower Design Basis Document," no. July, 2001.

[61]   V. Sobolev, "Database of thermophysical properties of liquid metal coolants for GEN-IV," *SCK• CEN Tech. Report, SCKCEN-BLG-1069*, vol. 16, no. 12, pp. 3496–3502, 2010.

[62]   E. Achenbach, "The effect of surface roughness on the heat transfer from a circular cylinder to the cross flow of air," *Int. J. Heat Mass Transf.*, vol. 20, no. 4, pp. 359–369, Apr. 1977.

[63]   W. C. Swinbank, "Long-wave radiation from clear skies," *Q. J. R. Meteorol. Soc.*, vol. 89, no. 381, pp. 339–348, Jul. 1963.

[64] X. Berger, D. Buriot, and F. Garnier, "About the equivalent radiative temperature for clear skies," *Sol. Energy*, vol. 32, no. 6, pp. 725–733, Jan. 1984.

[65] M. R. Rodríguez-Sánchez, "On the design of solar external receivers," pp. 1–256, 2015.

[66] R. D. Kale, B. K. Sreedhar, and K. V. Sreedharan, "The history of liquid metal pump development in India," *Curr. Sci.*, vol. 114, no. 2, pp. 292–307, 2018.

[67] NREL, "https://solarpaces.nrel.gov/by-technology/power-tower." .

[68] M. J. Wagner, "SolarPILOT User ' s Manual," pp. 1–67, 2015.

[69] C. S. Turchi, Z. Ma, T. W. Neises, and M. J. Wagner, "Thermodynamic Study of Advanced Supercritical Carbon Dioxide Power Cycles for Concentrating Solar Power Systems," *J. Sol. Energy Eng.*, vol. 135, no. 4, Nov. 2013.

[70] A. Ambrosini, A. Boubault, C. K. Ho, L. Banh, and J. R. Lewis, "Influence of application parameters on stability of Pyromark® 2500 receiver coatings," *AIP Conf. Proc.*, vol. 2126, no. July, 2019.

[71] J. Coventry and P. Burge, "Optical properties of Pyromark 2500 coatings of variable thicknesses on a range of materials for concentrating solar thermal applications," *AIP Conf. Proc.*, vol. 1850, 2017.

[72] John Fowler, "Annex X - ASME Design calculations." .

[73] D. R. Eno, G. A. Young, and T. L. Sham, "A unified view of engineering creep parameters," *Am. Soc. Mech. Eng. Press. Vessel. Pip. Div. PVP*, vol. 6, no. PARTS A AND B, pp. 777–792, 2008.

[74] J. Veverkova, A. Strang, G. R. Marchant, G. M. McColvin, and H. V. Atkinson, "High temperature microstructural degradation of Haynes Alloy 230," *Proc. Int. Symp. Superalloys*, pp. 479–488, 2008.

[75] W. Logie, C. Asselineau, J. Pye, and J. Coventry, "Thermal Stress in Sodium Receiver Tubes," vol. 135, no. November, pp. 6–7, 2016.

[76] R. W. Bradshaw *et al.*, "Final Test and Evaluation Results from the Solar Two Project," *Contract*, no. January, p. 294, 2002.

[77] C. A. Asselineau, W. Logie, J. Pye, and J. Coventry, "Limits of the cylindrical absorber design for a sodium receiver," *AIP Conf. Proc.*, vol. 2033, no. November, 2018.

[78] G. Lozza, "Turbine a gas e cicli combinati."

[79] M. H. Sabour and R. B. Bhat, "Lifetime prediction in creep-fatigue environment," *Mater. Sci. Pol.*, vol. 26, no. 3, pp. 563–584, 2008.

[80] X. Zhang *et al.*, "Recent developments in high temperature heat exchangers: A review," *Front. Heat Mass Transf.*, vol. 11, no. July, 2018.

[81] B. Sunden, "High Temperature Heat Exchangers (HTHE)," *Heat Transf. Proc. Int. Heat Transf. Conf.*, vol. 1, no. September, pp. 259–268, 1986.

[82]   D. Fleming and A. Kruizenga, "Identified Corrosion and Erosion Mechanisms in SCO2 Brayton Cycles," no. June, 2014.

[83]   D. Southall, R. Le Pierres, and S. J. Dewson, "Design considerations for compact heat exchangers," *Int. Conf. Adv. Nucl. Power Plants, ICAPP 2008*, vol. 3, pp. 1953–1968, 2008.

[84]   G. GTI, SwRI, "10 MWe Supercritical Carbon Dioxide (sCO 2) Pilot Power Plant," pp. 1–8, 2019.

[85]   T. Sasaki, M. Itoh, H. Maeda, J. Tominaga, D. Saito, and Y. Niizeki, "Development of turbine and combustor for a semi-closed recuperated brayton cycle of supercritical carbon dioxide," *Am. Soc. Mech. Eng. Power Div. POWER*, vol. 1, pp. 1–6, 2017.

[86]   R. Allam *et al.*, "Demonstration of the Allam Cycle: An Update on the Development Status of a High Efficiency Supercritical Carbon Dioxide Power Process Employing Full Carbon Capture," *Energy Procedia*, vol. 114, no. January 2018, pp. 5948–5966, 2017.

[87]   D. Arrell, "Next generation engineered materials for ultra supercritical steam turbines," *Siemens Power Gener. Rep.*, no. May, p. 87, 2006.

[88]   D. Gandy and J. Shingledecker, Eds., *Advances in Materials Technology for Fossil Power Plants: Proceedings from the Seventh International Comference*. ASM International, 2013.

[89]   T. Zhang, "Considerations when Designing Turbomachinery with sCO2 as a Working Fluid," vol. 2, 2019.

[90]   M. F. Aksit, "Brush Seals and Common Issues In Brush Seal Applications," pp. 1–14, 2012.

[91]   M. J. Neale, "The tribology handbook," *Tribol. Handb.*, vol. 3, p. B22.1-B22.6, 1996.

[92]   S. & C. TMI, "SCO2 turbomachinery systems," vol. 2, 2018.

[93]   J. Lee, S. Baik, S. K. Cho, J. E. Cha, and J. I. Lee, "Issues in performance measurement of CO2 compressor near the critical point," *Appl. Therm. Eng.*, vol. 94, pp. 111–121, 2016.

[94]   D. Ranjan, "Fundamental study of key issues related to advanced sCO 2 Brayton cycle: prototypic hx development and cavitation."

[95]   E. Pesatori *et al.*, "Optimized cycle and turbomachinery configuration for an intercooled, recompressed sCO2 cycle," *6th Int. Symp. - Supercrit. CO2 Power Cycles*, no. March 2018, 2018.

[96]   D. Stahl, F. K. Boese, and S. Kostrzewa, "System and components design of a sodium heat transfer circuit for solar power plants," *Electr. Power Syst. Res.*, vol. 3, no. 3–4, pp. 151–161, Sep. 1980.

[97]   B. K. Sreedhar *et al.*, "Development of active magnetic bearings and ferrofluid seals toward oil free sodium pumps," *Nucl. Eng. Des.*, vol. 265, pp. 1166–1174, 2013.

[98]   P. Chellapandi, R. Suresh Kumar, S. Jalaldeen, P. Selvaraj, and S. C. Chetal, "Evaluation of speed lowering of primary sodium pump into sodium pool for 500 MWe PFBR based on creep damage," *Procedia Eng.*, vol. 55, pp. 451–456, 2013.

[99]   K. A. Polzin, M. Space, and M. Space, "Liquid-Metal Pump Technologies for Nuclear Surface Power," no. March 2007, 2020.

[100]   H. Ota *et al.*, "Development of 160 m3/min Large Capacity Sodium-Immersed Self-Cooled Electromagnetic Pump," *J. Nucl. Sci. Technol.*, vol. 41, no. 4, pp. 511–523, 2004.

[101]   E. Khodarev, "Liquid Metal Fast Breeder Reactors 1962-1971," *IAEA Bull.*, vol. 20, no. 6, 1971.

[102]   B. A. Brese, R. G. Pint, and J. R. Keiser, "Supercritical CO2 Compatibility of Structural Alloys at 400°-750°C."

[103]   M. Walker and E. Withey, "Influence of CO2 Purity on the Corrosion of Structural Alloys for Supercritical CO2 Power Cycles," *6th Int. Supercrit. CO 2 Power Cycles Symp. March 27 - 29, 2018, Pittsburgh, Pennsylvania*, pp. 1–20, 2018.

[104]   B. A. Pint and J. R. Keiser, "The Effect of Impurities on Oxidation in Supercritical CO2 at 750°C," *6th Int. Symp. - Supercrit. CO2 Power Cycles*, vol. 2, pp. 1–12, 2018.

[105]   G. Manzolini, "Concentrated solar power : CSP plant design."

[106]   B. Hoffschmidt *et al.*, "CONCENTRATING SOLAR POWER _ Renewable energy technologies: cost analyses series," *IRENA Work. Pap.*, vol. 3, no. 2, pp. 595–636, 2012.

8 Appendix A - Heat exchangers model

The heat exchangers have been modelled in Matlab initially to verify the consistency of pressure loss assumption made by Polimeni in [4] with the pressure drop model found in his thesis [12]. This model comes originally from the thesis of Dostal [27] and it is composed by two linked parts, the heat transfer model, which calculates the heat transfer area starting from temperature and pressure at the cold end of the heat exchanger and the total heat transferred, and the pressure drop model, which computes the total pressure drop starting from the calculated exchange area. The overall procedure is iterative because the two models depend from each other.

Both models start from the definition of the geometry of the heat exchanger. For this initial study a Printed Circuit Heat Exchanger (PCHE) type has been chosen for both the Primary heat exchanger and the regenerators.

This type heat exchanger is less sensitive to high pressures and high-pressure differentials since it consists of many plates, into which the channels are chemically etched, which are then fused together by diffusion bonding to form a monolithic block. The channels can be straight of wavy. In this model a straight configuration has been chosen for sake of simplicity. PCHEs offer the heat transfer capability of a plate heat exchanger combined with the pressure and temperature capabilities of a shell and tube heat exchanger.

The flows enters in a counter-current arrangement, flowing in the straight channels with have a semi-circular cross-section, as in Figure 8.1.
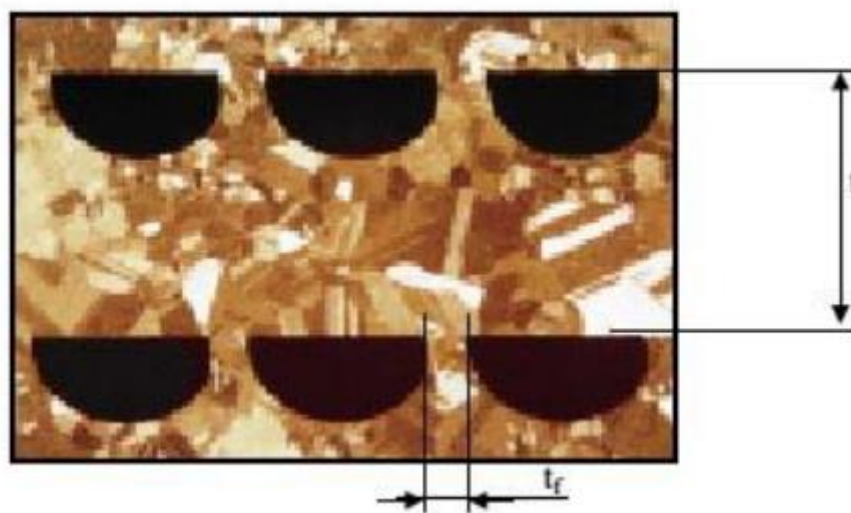
Figure 8.1 Cross section area of a PCHE [12]

Heatric PCHE's main geometrical parameters taken from [12] are:

- $d_c = 2mm$, semi-circular channel diameter;
- $t = 1.5\ mm$, plate thickness;
- $t_n = 3\ mm$, node thickness (hot plus cold side);
- $p_c = 2.4\ mm$, channel pitch.

The following simplifying assumptions were considered:

- The geometry of the channels on the hot and the cold sides are the same;
- The total mass flow rate of each side is equally distributed on the channels;
- The heat conduction area is approximated as the heat transfer area of each channel, while the heat conduction length is equal to the plate thickness;
- The temperature distribution is periodic, with a span of two plates, and the temperature variation along the channel cross-sectional perimeter is neglected.

These assumptions allow to evaluate the performances of the heat exchangers just evaluating the heat transfer between one hot and one cold channel and to extend the results to the whole geometry by simply multiplying by the number of channels. In addition, the heat conduction among the plates can be modelled as a one-dimensional problem through a planar wall.

The inputs required are the temperature of the fluids at the inlet and outlet and a preliminary guess of their pressures. In this case assumption made by Polimeni et al. [4] where used to calculate preliminary guesses for pressure at the inlet and outlet of the heat exchanger. Temperatures across the heat exchanger come from the power block model developed in Excel.

Heat exchange is calculated from the temperature difference on the cold side of the HX through the use of the REFPROP functions implemented in Matlab, used to compute the thermodynamic properties of the fluid at a specific temperature and pressure. The velocity at the hot side inlet is chosen in order to match pressure drops on the low pressure side (hot side) with the pressure drops assumptions the work started from (Polimeni et al. [4]), a special attention has to be made on the calculated Reynolds number in each discretization of both hot and cold vessels which need to be high enough so that flow in the HX is always in a turbulent regime, which is favourable in terms of pressure drops and heat transfer.

Models coming from Dostal [27] have been used to define the geometry and calculate the heat transfer area and pressure drop on the heat exchangers, they are described in the following paragraphs.

The model starts from the definition of the equivalent hydraulic diameter from the geometrical parameters previously reported. This parameter will then be used for the calculation of the Reynolds number

$$d_{eq} = \frac{4\pi d_c^2}{8\left(\pi \frac{d_c}{2} + d_c\right)}$$

The flow area of the channel is instead calculated with the geometrical diameter:

$$A_{channel} = \pi \frac{d_c^2}{8}$$

The absolute roughness is assumed to be 10 μm and its value it's used to compute the relative roughness as $\Delta = R/d_c$.

The density of the hot flow outlet is evaluated with REFPROP, thus the overall channel area needed can be computed:

$$A_{tot-side} = \frac{\dot{m}_{side}}{\rho_{hot_{in}} v_{hot_{in}}}$$

Dividing the overall flow area by the one of a single channel we can find the number of channels, n_{chan}.

Once the geometry has been defined the heat exchanger has been divided in several axial nodes (see Figure 8.2) under the hypotheses that each node exchanges the same thermal power, in this way it is possible to take into account the variation of the thermodynamic properties with the temperature along the channel length.
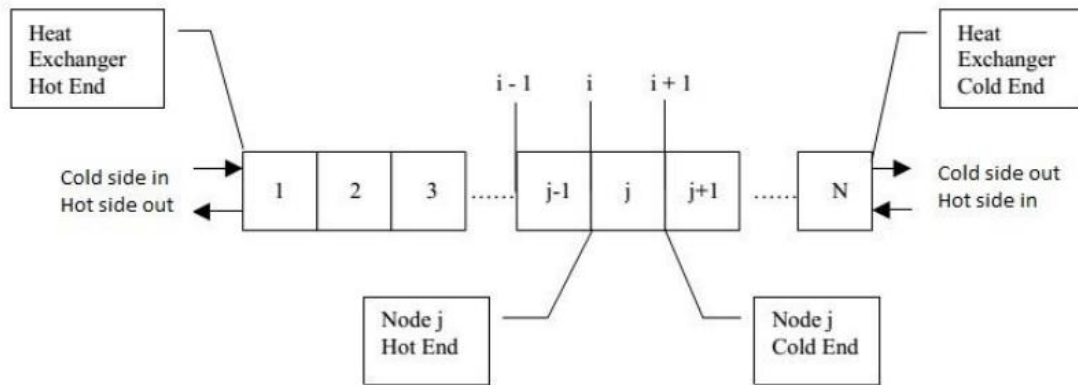
Figure 8.2 Node division of the heat exchanger channels

Since it was assumed that every channel exchanges heat just with the adjacent one and that each node exchanges the same heat, the total heat transferred can be divided by the number of channels and the number of nodes (j) to find the heat exchanged by the single section of channel:

$$\dot{q}_{node} = \frac{\dot{Q}_{HX}}{j\, n_{chan}} \qquad\qquad \textit{Eq. 8.4}$$

The cold end enthalpy on both sides is evaluated with REFPROP or, when applying the model to the primary heat exchanger, with a manually added function which calculates the properties of sodium as a function of temperature (function described in section 3.2).

Once the initial enthalpy value has been defined, enthalpy at the end of the node can be computed adding (or subtracting in case of cold side) the heat exchanged in that node divided by the mass flow rate of the fluid in the channel, this procedure goes on for all the sections:

$$\dot{H}_{i+1_{side}} = \dot{H}_{i_{side}} + \frac{\dot{q}_{node}}{\dot{m}_{chan}} \qquad\qquad \textit{Eq. 8.5}$$

In Eq. 8.5, i represent the index of nodes' interfaces.

To calculate the length on the channels and pressure drops an iterative procedure must be adopted, since the pressure drop are dependent from the channel length and vice-versa.

This procedure is applied to each node and it converges when the error, calculated as the difference between the length of the node calculated at iteration k and the length calculated at iteration $k+1$, is below 1e-8 m; then the calculation starts for the subsequent node.

1) Initially, once the enthalpy H_i and H_{i+1} has been calculated, temperature at both node's interfaces are calculated with the REFPROP solftware.

$$Ti = f(Hi, pi); \; T_{i+1} = f(H_{i+1}, p_{i+1}) \qquad\qquad \textit{Eq. 8.6}$$

$$T_{j-mean} = \frac{T_i + T_{i+1}}{2}; \; p_{j-mean} = \frac{p_i + p_{i+1}}{2} \qquad\qquad \textit{Eq. 8.7}$$

Pressure p_{i+1} is evaluated in the first iteration as $pi \pm \frac{\Delta p_{assumed}}{n_{sections}}$ (+ for the cold fluid, - for the hot one, which exits from the cold end side), at the second iteration the value of pressure is recalculated as $pi \pm \frac{\Delta p_{j,calculated}}{n_{sections}}$ starting from the pressure drop calculated at that iteration.

2) Fluid properties, such as density and viscosity, are evaluated at node average conditions:

$$\rho_j = f(T_{j-mean}, p_{j-mean}); \; \mu_j = f(T_{j-mean}, p_{j-mean}) \qquad\qquad \textit{Eq. 8.8}$$

3) The velocity of the fluid in each section and the Reynolds number associated are computed to determine the flow regime and subsequently to calculate pressure drops and heat transfer length.

$$v_j = \frac{\dot{m}_{channel}}{\rho_j \, A_{channel}} \; ; Re_j = \frac{\rho_i \, v_j \, d_{eq}}{\mu_j}$$

<div align="right">Eq. 8.9</div>

4) The friction factor f is evaluated with the model taken by Dostal [27], described in Appendix B, the pressure loss can be estimated as:

$$\Delta p_j = \frac{1}{2} f \frac{l_{node}}{d_{eq}} \rho_j v_j^2 + \frac{1}{2} C \rho_j v_j^2$$

<div align="right">Eq. 8.10</div>

Where C is the concentrated loss coefficient, whose values has been evaluated in just three simplified cases by Polimeni as:

$$C = \begin{cases} 0.5; & if \; entrance \; loss \\ 1; & if \; exit \; loss \\ 0; & otherwise \end{cases}$$

<div align="right">Eq. 8.11</div>

5) The heat transfer coefficient is function of the Nusselt number , which is computed starting from the Reynolds number (Re_j), with different correlations depending on the flow regime, these are reported in the model provided by Dostal [27] described in Appendix C. From the definition of Nusselt number we can calculate the convective heat transfer coefficient:

$$h_j = \frac{Nu_j k_j}{d_{eq}}$$

<div align="right">Eq. 8.12</div>

Where k_j is the conductivity of the fluid. The same procedure is applied for both sides, and both the convective heat transfer coefficients are computed.

6) The conduction across the channels is modelled as conduction through a flat plate and therefore the overall heat transfer coefficient can be computed as:

$$U_{eq_j} = \left(\frac{1}{h_{j-hot}} + \frac{t}{k_{metal}} + \frac{1}{h_{j-cold}} \right)^{-1}$$

<div align="right">Eq. 8.13</div>

7) Node length can be lastly evaluated as:

$$L_j = \frac{\dot{q}_{node}}{U_{eq_j} \left(\pi * \frac{d_c}{2} + d_c \right) \Delta T_{lm_j}}$$

<div align="right">Eq. 8.14</div>

8) The pressure at the exit of the node is adjusted with the new pressure drop value.

9) The error based on the difference between the new length calculated and the previous one is computed, and the whole procedure goes one until its value is lower than the tolerance. When the convergence in one node is reached, the calculations continue for the next one, starting from the pressure value obtained for the previous node.

9 Appendix B

Pressure drop model for Heat Exchangers

The friction losses that occur in the channels are caused by the shear stress acting near the pipes' surface, because of fluid's viscosity, leading to a reduction of pressure along the channel length:

$$\Delta p_{distr} = f \frac{\rho L v^2}{2D} \qquad \text{Eq. 9.1}$$

The friction factor f is a parameter that considers the viscosity effect, and its value is strongly dependent on the flow regime and relative roughness of the tubes.

First, the borders of different flow regimes must be identified, in term of Reynolds number boundaries. The limits values of Re depend from the relative roughness R_{rel} calculated as:

$$R_{rel} = \frac{R_{abs}}{d_{eq}} \qquad \text{Eq. 9.2}$$

- **Laminar flow**:
  $if\ Re < Re_0$, with Re_0 calculated as:

$$Re_0 = \begin{cases} 754 \exp\left(\dfrac{0.0065}{R_{rel}}\right), & if\ R_{rel} > 0.007 \\ 2000, & otherwise \end{cases} \qquad \text{Eq. 9.3}$$

$$f = \frac{64}{Re} \qquad \text{Eq. 9.4}$$

  $if\ Re_0 < Re < Re_1$, with Re_1 calculated as:

$$Re_1 = \begin{cases} \dfrac{1160}{R_{rel}}, & if\ R_{rel} > 0.007 \\ 2000, & otherwise \end{cases} \qquad \text{Eq. 9.5}$$

$$f = 4.4 Re^{-0.595} \exp\left(\frac{0.00275}{R_{rel}}\right) \qquad \text{Eq. 9.6}$$

- **Transitional flow:** $if\ Re_1 < Re < Re_2$

$$Re_2 = 2090 \left(\frac{1}{R_{rel}}\right)^{0.0635} \qquad \text{Eq. 9.7}$$

$$f = (f_2 - f^*) \exp\left(-0.0017(Re_2 - Re)\right)^2 + f^* \qquad \text{Eq. 9.8}$$

Where f_2 is obtained through the Colebrook equation:

$$f_2 = \left(2 \log_{10} \left(\frac{2.51}{Re_2 \sqrt{f_2}} + \frac{R_{rel}}{3.7} \right) \right)^{-2}$$

Eq. 9.9

While f^* is evaluated as:

$$f^* = \begin{cases} 0.032, & if\ R_{rel} \leq 0.007 \\ 0.0733 - \dfrac{0.0109}{R_{rel}^{0.286}}, & otherwise \end{cases}$$

Eq. 9.10

- **Turbulent flow**: $if\ Re_2 < Re < Re_3$ the regime is turbulent but the friction factor still depends from the Reynolds number:

$$Re_3 = 441.19\ R_{rel}^{-1.1772}$$

Eq. 9.11

$$f = \left(2 \log_{10} \left(\frac{2.51}{Re \sqrt{f}} + \frac{R_{rel}}{3.7} \right) \right)^{-2}$$

Eq. 9.12

- **Fully developed turbulent flow**: $if\ Re > Re_3$ the turbulent regime is fully developed and the friction factor is independent from the Reynolds number:

Eq. 9.13

$$f = \left(2 \log_{10} \left(\frac{2.51}{Re_3 \sqrt{f}} + \frac{R_{rel}}{3.7} \right) \right)^{-2}$$

The previous correlations are the mathematical transcription of the Moody's diagram. To get the correct results, the friction factor is evaluated considering a fictitious hydraulic diameter d_{eq}, as the cross-section of the channels under investigation is semi-circular.

10 Appendix C

Heat transfer model for heat exchangers

The aim of the thermal model is to assess the heat transfer properties of the fluids involved, giving the relations that link the flow regime with the Nusselt number, representative of the forced convection phenomena. The first distinction among the fluids is based on Prandtl number.

If $0.5 < Pr < 2000$, condition which applies for CO_2, the following method applies:

- **Laminar flow:** $Re < 2300$

$$Nu = 4.089 \qquad \text{Eq. 10.1}$$

- **Turbulent flow:** $Re > 5000$
  The heat transfer characteristics are linked to the friction factor, computed as:

$$fc = \left(\frac{1}{1.8 \ln(Re) - 1.5}\right)^2 \qquad \text{Eq. 10.2}$$

  For straight semi-circular channels, the Gnielinski correlation can then be used to calculate the Nusselt number:

$$Nu = \frac{fc/8 \, (Re - 1000)Pr}{1 + 1.27(Pr^{\frac{2}{3}} - 1)\sqrt{\frac{fc}{8}}} \qquad \text{Eq. 10.3}$$

- **Transitional flow:** $2300 < Re < 5000$
  The Gnielinski correlation is useful for turbulent flows, but for low Reynolds number it is less and less accurate. The resulting Nusselt number for $Re = 2300$ is not the one suggested for laminar flow, introducing a discontinuity in the model. To guarantee continuity for every Reynolds range, the transitional Nusselt number is obtained as linear interpolation between the two flow conditions:

$$Nu = 4.089 + \frac{Nu|_{Re=5000} - 4.089}{5000 - 2300}(Re - 2300) \qquad \text{Eq. 10.4}$$

For low Prandtl number fluids ($Pr \ll 1$), that is the case of liquid sodium the Nusselt number dependence on channel roughness is negligible, and, approximating each node conditions as a constant heat flux problem, it can be obtained with the Sleicher – Rouse correlation:

$$Nu = 6.3 + 0.0167Re^{0.85}Pr^{0.93} \qquad \text{Eq. 10.5}$$

11 Appendix D

Property	unit	correlation	source
Density	kg/m^3	$219 + 275.32\left(1 - \dfrac{T(K)}{2503.7}\right) + 511.58\left(1 - \dfrac{T(K)}{2503.7}\right)^{0.5}$	[13], [61]
Specific heat	J/kgK	$1658.2 - 0.8479 * T(K) + 4.4541x10^{-4} * T^2(K) - 2.9926x10^6 * T^{-2}(K)$	[12], [43]
Conductivity	W/mK	$124.67 - 0.11381 * T(K) + 5.5226x10^{-5} * T^2(K) - 1.1842x10^{-8} * T^3(K)$	[13]
Viscosity	$Pa * s$	$Exp\left(-6.4406 - 0.3958\,ln\big(T(K)\big) + \dfrac{556.835}{T(K)}\right)$	[13]
Enthalpy*	kJ/kg	$\displaystyle\int_{Tref}^{T} Cp(T)dT$	

Table 11.1 Property correlations valid for liquid sodium [97.8°C; 873°C] [3]

*Calculated as the integral of the specific heat over the temperature range neglecting the influence of pressure, the reference temperature chosen is the melting temperature of sodium, $T_{melt} = 371\,K \cong 97.8\,°C$. [61]

12 Appendix E

```
TURBINA A GRADO DI REAZIONE 0.5
DATI GENERALI
Portata    Pmonte    HMonte     TMonte   PFin    TFin     HStatfin   HTotfin    RPM         Ang.ing   vel.ing.  AngBase  AngCima  NStadi   rug.pal.
[kg/s]     [bar]     [kJ/kg]    [°C]     [bar]   [°C]     [kJ/kg]    [kJ/kg]    [Giri/min]  [°]       [m/s]     [°]      [°]      --       [mm]
 286.17    241.33    1253.785   725      84.85   577.065  1076.994   1077.84    4600        90        38.6445   0        0        10       0.002
DATI PER STADIO
```

		Stadio 1	Stadio 2	Stadio 3	Stadio 4	Stadio 5	Stadio 6	Stadio 7	Stadio 8	Stadio 9	Stadio10
Stat.Profilo	[-]	7015S04	7015S03	7015S04	7015S03	7015S03	7015S03	7015S04	7015S04	7015S05	7015S04
Rot. Profilo	[-]	7015S03	7015S03	7015S03	7015S03	7015S03	7015S04	7015S04	7015S05	7015S05	7015S04
Stat.Dbase	[mm]	500	500	500	500	500	500	500	500	500	500
Rot. Dbase	[mm]	500	500	500	500	500	500	500	500	500	500
Stat.DMedio	[mm]	536.27	538.51	540.94	543.65	547.5	549.8	554.63	560.07	561.6	569.38
Rot. DMedio	[mm]	538.39	540.01	543.42	545.41	549.55	552.06	557.21	561.29	565.47	573.63
Stat.HPala	[mm]	36.268	38.514	40.936	43.65	47.498	49.796	54.628	60.071	61.604	69.376
Rot. HPala	[mm]	38.387	40.012	43.421	45.415	49.553	52.06	57.206	61.289	65.474	73.634
Stat.PosAss	[mm]	0	75.04	153.98	229.02	301.61	374.2	461.94	552.13	657.46	758.89
Rot. PosAss	[mm]	38.74	111.33	192.72	265.31	337.91	416.85	507.03	603.57	711.35	803.98
Stat. g/S-NPal	[-]	.282 50	.284 62	.285 50	.286 62	.280 64	.289 62	.281 52	.274 54	.293 42	.278 54
Rot. g/S-NPal	[-]	.273 65	.281 63	.275 65	.283 63	.277 65	.285 51	.278 53	.281 44	.283 44	.272 56
Stat.gRad	[mm]- N°	.150 3	.150 3	.150 3	.150 3	.150 3	.150 3	.150 3	.150 3	.150 3	.150 3
Rot. gRad	[mm]- N°	.150 3	.150 3	.150 3	.150 3	.150 3	.150 3	.150 3	.150 3	.150 3	.150 3
Stat.S/C	Base-Cima	.70 .80	.70 .81	.70 .81	.70 .82	.68 .81	.70 .84	.67 .82	.65 .80	.69 .87	.65 .83
Rot. S/C	Base-Cima	.67 .77	.69 .80	.67 .78	.69 .81	.67 .80	.68 .83	.66 .81	.66 .83	.66 .84	.62 .81
		--------	--------	--------	--------	--------	--------	--------	--------	--------	--------
Stat.U/C0	[-]	0.9697	0.9697	0.9697	0.9697	0.9697	0.9697	0.9697	0.9697	0.9697	0.9697
Rot. U/C0	[-]	0.9717	0.9717	0.9719	0.9721	0.9723	0.9737	0.973	0.9732	0.9735	0.9768
Stat.p1	[bar]	229.889	209.789	190.972	173.336	156.863	141.506	127.227	113.892	101.605	90.202
Rot. p1	[bar]	219.681	200.241	182.007	164.986	149.049	134.276	120.466	107.631	95.826	84.85
Stat.T1	[°C]	717.623	703.955	690.066	675.941	661.57	646.938	632.013	616.708	601.126	585.15
Rot. T1	[°C]	710.827	697.062	683.046	668.817	654.298	639.557	624.443	608.968	593.236	577.065
G.Reaz.	[]	0.5	0.5	0.5	0.5	0.5	0.5	0.5	0.5	0.5	0.5
Stat.h0Stat	[kJ/kg]	1253.038	1236.35	1219.538	1202.532	1185.377	1167.978	1150.416	1132.51	1114.277	1095.841
Rot. h0Stat	[kJ/kg]	1244.692	1227.942	1211.035	1193.952	1176.679	1159.197	1141.465	1123.384	1105.075	1086.404
H0Tot	[kJ/kg]	1253.79	1237.1	1220.33	1203.31	1186.2	1168.79	1151.27	1133.34	1115.14	1096.74
Stat.h1Misc	[kJ/kg]	1244.692	1227.942	1211.035	1193.952	1176.679	1159.197	1141.465	1123.384	1105.075	1086.404
Rot. h1Misc	[kJ/kg]	1236.35	1219.538	1202.532	1185.377	1167.978	1150.416	1132.51	1114.277	1095.841	1076.994
Stat.h1	[kJ/kg]	1244.643	1227.896	1210.992	1193.912	1176.641	1159.161	1141.431	1123.352	1105.045	1086.376
Rot. h1	[kJ/kg]	1236.293	1219.484	1202.481	1185.329	1167.933	1150.373	1132.468	1114.238	1095.805	1076.959
Stat.Titolo	[-]	1	1	1	1	1	1	1	1	1	1
Rot. Titolo	[-]	1	1	1	1	1	1	1	1	1	1
Stat.MachIs	[-]	0.275	0.28	0.286	0.29	0.297	0.301	0.308	0.314	0.32	0.328
Rot. MachIs	[-]	0.279	0.284	0.289	0.294	0.3	0.305	0.311	0.316	0.326	0.332

Stat.Mach	[-]	0.268	0.273	0.278	0.283	0.289	0.293	0.301	0.307	0.312	0.32
Rot. Mach	[-]	0.272	0.276	0.282	0.286	0.292	0.297	0.304	0.309	0.318	0.324
Stat.CEffBase	[-]	0.9753	0.9747	0.97562	0.97496	0.97475	0.97508	0.97576	0.97547	0.97669	0.97563
Rot. CEffBase	[-]	0.97416	0.97459	0.97436	0.97481	0.97454	0.97586	0.97545	0.97627	0.97642	0.97489
Stat.Rapp.g/s	[-]	1.04487	1.04441	1.04422	1.04371	1.04557	1.04292	1.04529	1.04756	1.04189	1.0462
Rot. Rapp.g/s	[-]	1.04823	1.04541	1.04744	1.04465	1.04651	1.04418	1.04644	1.04523	1.04467	1.04863
Stat.eta	[-]	0.950462	0.949259	0.951061	0.949718	0.949267	0.949906	0.951216	0.950603	0.953004	0.950846
Rot. eta	[-]	0.948192	0.949023	0.948529	0.949413	0.94885	0.951431	0.95058	0.952173	0.952429	0.949333
Stat.U	[m/s]	129.163	129.704	130.287	130.941	131.868	132.421	133.585	134.896	135.265	137.137
Rot. U	[m/s]	129.673	130.065	130.886	131.366	132.363	132.967	134.206	135.189	136.197	138.163
Stat.QFuga	[kg/s]	1.677	1.568	1.462	1.361	1.265	1.17	1.083	1	0.914	0.841
Rot. QFuga	[kg/s]	1.927	1.807	1.705	1.593	1.5	1.395	1.312	1.222	1.135	1.065
Stat.V1	[m/s]	134.854	135.346	136.377	136.807	138.025	138.485	140.074	141.138	141.875	143.795
Rot. V1	[m/s]	38.896	40.047	39.588	40.807	40.295	41.561	40.942	41.598	42.537	41.206
Stat.V1m	[m/s]	39.799	40.139	40.528	40.883	40.443	41.766	41.158	40.581	43.341	41.873
Rot. V1m	[m/s]	38.89	40.045	39.58	40.805	40.292	41.558	40.937	41.598	42.522	41.203
Stat.V1t	[m/s]	128.848	129.257	130.216	130.555	131.967	132.037	133.89	135.178	135.092	137.564
Rot. V1t	[m/s]	-0.716	-0.382	-0.802	-0.412	-0.438	-0.492	-0.616	-0.04	-1.148	-0.5
Stat.W1	[m/s]	39.801	40.141	40.528	40.885	40.443	41.768	41.159	40.582	43.342	41.875
Rot. W1	[m/s]	136.065	136.455	137.507	137.951	138.779	139.779	140.9	141.483	143.777	144.655
Stat.W1t	[m/s]	-0.315	-0.447	-0.072	-0.386	0.099	-0.385	0.305	0.282	-0.173	0.426
Rot. W1t	[m/s]	130.389	130.447	131.688	131.778	132.801	133.459	134.822	135.23	137.345	138.663
Stat.AngUsc	[-]	90.4541	90.6376	90.1013	90.5403	89.8592	90.5278	89.5755	89.6022	90.229	89.4167
Rot. AngUsc	[-]	91.0547	90.5467	91.1604	90.5788	90.6235	90.6784	90.8624	90.0555	91.5459	90.6953
RotD.Spinta	[kN]	200.3	188.1	176.2	164.9	154.4	143.4	134	125	114.6	106.9
RotP.Spinta	[kN]	274.2	259.3	249.1	235.2	226.2	212.8	205.7	195.5	185.3	180.5
StatP.Spinta	[kN]	71	70.6	70.3	70.1	71.4	69.6	71.5	73.6	69.2	73.3
Stat.ECinU	[kJ/kg]	9.0929	9.1593	9.2994	9.3581	9.5255	9.5891	9.8103	9.9599	10.0642	10.3385
Rot. ECinU	[kJ/kg]	0.7565	0.8019	0.7836	0.8326	0.8118	0.8636	0.8381	0.8652	0.9047	0.849
Stat.PAttrRot	[kW]	25.3885	19.4637	23.0063	17.6043	16.7936	15.854	18.7863	17.9112	19.9595	16.0029
Rot. PAttrRot	[kW]	22.7245	21.6493	20.8698	19.8515	19.1486	22.6063	21.8487	24.9471	23.7838	19.4525
Stat.S0	[kJ/(kg*K)]	2.9447	2.9458	2.9469	2.948	2.9492	2.9504	2.9515	2.9528	2.954	2.9552
Rot. S0	[kJ/(kg*K)]	2.9452	2.9463	2.9474	2.9486	2.9498	2.951	2.9521	2.9534	2.9546	2.9559
Pot.	[kW]	4712.94	4744.45	4816.21	4846.81	4938.57	4963.27	5081.94	5158.76	5213.42	5367.02

Potenza di gruppo (kW): 49843.39; Potenza di gruppo (kW): 49843.39; Potenza dissipata X attrito (kW): 407.652
Rendimento isoentropico di gruppo: .9319; Efficienza volumetrica di gruppo: 99.5317%
Spinta totale di gruppo (kN): sul rotore 3731.5; sullo statore: 710.5
Lunghezza canale da inizio 1°Stat a fine ultima rot: 836.53 mm

Table 12.1 Calculation results obtained with the FTM proprietary code "Fila per fila", homogeneous degree of reaction (0.5) case

```
TURBINA A GRADO DI REAZIONE VARIABILE
DATI GENERALI
Portata  Pmonte  HMonte    TMonte  PFin   TFin     HStatfin   HTotfin   RPM         Ang.ing  vel.ing.  AngBase  AngCima  NStadi  rug.pal.
[kg/s]   [bar]   [kJ/kg]   [°C]    [bar]  [°C]     [kJ/kg]    [kJ/kg]   [Giri/min]  [°]      [m/s]     [°]      [°]      --      [mm]
286.17   241.33  1253.785  725     84.85  577.949  1078.068   1079.413  5200        90       52.7414   0        0        7       0.002
DATI PER STADIO
```

		Stadio 1	Stadio 2	Stadio 3	Stadio 4	Stadio 5	Stadio 6	Stadio 7
Stat.Profilo	[-]	7015S04	7015S04	7015S04	7015S03	7015S03	7015S04	7015S04
Rot. Profilo	[-]	7015S03	7015S03	7015S03	7015S04	7015S04	7015S05	7015S05
Stat.Dbase	[mm]	500	500	500	500	500	500	500
Rot. Dbase	[mm]	500	500	500	500	500	500	500
Stat.DMedio	[mm]	527.04	533.38	537.28	540.83	547.3	550.88	558.07
Rot. DMedio	[mm]	535.9	541.22	545.54	546.72	548.95	554.69	560.98
Stat.HPala	[mm]	27.04	33.376	37.283	40.835	47.297	50.875	58.07
Rot. HPala	[mm]	35.898	41.219	45.538	46.725	48.954	54.686	60.976
Stat.PosAss	[mm]	0	81.39	162.78	237.82	319.2	406.94	505.92
Rot. PosAss	[mm]	38.74	120.13	201.52	280.46	361.85	458.39	557.37
Stat.g/S-NPal	[-]	.278 50	.272 52	.274 52	.285 62	.273 66	.289 50	.283 52
Rot. g/S-NPal	[-]	.272 65	.281 63	.269 67	.282 51	.279 52	.284 43	.287 43
Stat.gRad	[mm]- N°	.150 3	.150 3	.150 3	.150 3	.150 3	.150 3	.150 3
Rot. gRad	[mm]- N°	.150 3	.150 3	.150 3	.150 3	.150 3	.150 3	.150 3
Stat.S/C	Base-Cima	.70 .77	.67 .76	.67 .77	.70 .81	.66 .78	.70 .84	.67 .83
Rot. S/C	Base-Cima	.67 .76	.69 .80	.65 .76	.68 .81	.67 .80	.68 .83	.68 .84

```
--------------------------------------------------------------------------------
```

		Stadio 1	Stadio 2	Stadio 3	Stadio 4	Stadio 5	Stadio 6	Stadio 7
Stat.U/C0	[-]	0.7435	0.8228	0.8427	0.8724	0.8922	0.9121	0.9121
Rot. U/C0	[-]	1.0309	1.0967	1.0479	0.9971	0.893	0.9184	0.9168
Stat.p1	[bar]	218.002	190.818	167.763	146.845	127.506	108.724	92.34
Rot. p1	[bar]	207.018	181.902	158.839	137.982	117.644	100.364	84.85
Stat.T1	[°C]	709.638	690.275	671.777	652.907	633.158	611.202	589.146
Rot. T1	[°C]	702.327	683.465	664.073	644.2	622.073	600.383	577.949
G.Reaz.	[]	0.35	0.37	0.4	0.44	0.5	0.5	0.5
Stat.h0Stat	[kJ/kg]	1252.394	1225.972	1203.065	1179.718	1155.98	1129.759	1104.252
Rot. h0Stat	[kJ/kg]	1234.891	1211.305	1188.967	1166.356	1142.867	1116.948	1091.11
H0Tot	[kJ/kg]	1253.79	1226.93	1204	1180.61	1157.02	1131.07	1105.55
Stat.h1Misc	[kJ/kg]	1234.891	1211.305	1188.967	1166.356	1142.867	1116.948	1091.11
Rot. h1Misc	[kJ/kg]	1225.972	1203.065	1179.718	1155.98	1129.759	1104.252	1078.068
Stat.h1	[kJ/kg]	1234.746	1211.206	1188.882	1166.286	1142.806	1116.897	1091.064
Rot. h1	[kJ/kg]	1225.911	1203.016	1179.665	1155.924	1129.689	1104.192	1078.013
Stat.Titolo	[-]	1	1	1	1	1	1	1
Rot. Titolo	[-]	1	1	1	1	1	1	1
Stat.MachIs	[-]	0.4	0.37	0.371	0.366	0.371	0.375	0.386
Rot. MachIs	[-]	0.323	0.303	0.32	0.339	0.378	0.381	0.391
Stat.Mach	[-]	0.39	0.361	0.36	0.356	0.361	0.367	0.377
Rot. Mach	[-]	0.31	0.292	0.31	0.329	0.367	0.371	0.381

Stat.CEffBase	[-]	0.97613	0.97592	0.97271	0.97349	0.9746	0.97812	0.9777
Rot. CEffBase	[-]	0.95971	0.96617	0.96862	0.97232	0.97327	0.97492	0.97495
Stat.Rapp.g/s	[-]	1.04326	1.04727	1.04664	1.04315	1.04688	1.0415	1.04273
Rot. Rapp.g/s	[-]	1.04864	1.04524	1.04975	1.0449	1.04446	1.04262	1.04122
Stat.eta	[-]	0.95129	0.95111	0.944698	0.946292	0.948482	0.955516	0.954591
Rot. eta	[-]	0.919443	0.932292	0.93699	0.944177	0.945778	0.949049	0.949033
Stat.U	[m/s]	143.498	145.223	146.287	147.254	149.013	149.988	151.946
Rot. U	[m/s]	145.91	147.358	148.534	148.858	149.465	151.025	152.738
Stat.QFuga	[kg/s]	2.353	1.931	1.714	1.496	1.321	1.142	1.014
Rot. QFuga	[kg/s]	1.936	1.688	1.622	1.533	1.528	1.343	1.211
Stat.V1	[m/s]	194.393	176.751	173.394	168.847	168.254	168.038	169.921
Rot. V1	[m/s]	43.828	43.355	42.378	45.759	51.278	51.015	51.866
Stat.V1m	[m/s]	56.433	50.336	49.653	50.202	48.074	50.612	50.073
Rot. V1m	[m/s]	43.802	41.909	41.975	45.754	49.517	49.985	50.907
Stat.V1t	[m/s]	186.022	169.432	166.133	161.211	161.24	160.234	162.376
Rot. V1t	[m/s]	-1.507	11.102	5.834	0.669	-13.324	-10.199	-9.928
Stat.W1	[m/s]	70.661	55.855	53.472	52.106	49.604	51.639	51.148
Rot. W1	[m/s]	153.786	142.556	148.745	155.091	170.153	168.795	170.446
Stat.W1t	[m/s]	42.524	24.209	19.846	13.957	12.226	10.247	10.429
Rot. W1t	[m/s]	147.416	136.257	142.7	148.188	162.788	161.224	162.666
Stat.AngUsc	[-]	53.001	64.3146	68.2138	74.4631	75.7308	78.5549	78.2344
Rot. AngUsc	[-]	91.9702	75.1634	82.0869	89.1622	105.0604	101.5326	101.0359
RotD.Spinta	[kN]	411.5	308	268.8	228	199.2	169.6	152.5
RotP.Spinta	[kN]	290	244.1	251.5	251.8	284.4	250.2	233.4
StatP.Spinta	[kN]	110.4	100.7	97.8	90.7	91.7	84.1	86.7
Stat.ECinU	[kJ/kg]	18.8944	15.6205	15.0327	14.2546	14.1547	14.1183	14.4366
Rot. ECinU	[kJ/kg]	0.9604	0.9398	0.898	1.0469	1.3147	1.3013	1.3451
Stat.PAttrRot	[kW]	32.9183	31.1527	29.1722	21.8697	20.5526	23.3398	21.6544
Rot. PAttrRot	[kW]	30.1866	28.8906	27.2907	31.1251	28.4285	31.8709	29.8076
Stat.S0	[kJ/(kg*K)]	2.9447	2.9469	2.9487	2.9506	2.9523	2.9543	2.956
Rot. S0	[kJ/(kg*K)]	2.9458	2.9479	2.9497	2.9515	2.9533	2.9551	2.9569
Pot.	[kW]	7575.42	6468.8	6610.18	6676.49	7362.32	7233.94	7416.47

Potenza di gruppo (kW): 49343.62; Potenza dissipata X attrito (kW): 388.260
Rendimento isoentropico di gruppo: .9226; Efficienza volumetrica di gruppo: 99.4503%
Spinta totale di gruppo (kN): sul rotore   3543.2; sullo statore: 662.1
Lunghezza canale da inizio 1°Stat a fine ultima rot: 589.92 mm

Table 12.2 Calculation results obtained with the FTM proprietary code "Fila per fila", variable degree of reaction case